Aix*Marseille université
Socialement engagée

NNT/NL : 2020AIXM0001/001ED000

THÈSE DE DOCTORAT

Soutenue à Aix-Marseille Université
le 30 novembre 2022 par

Alain COIMBRA

Modelling flame spread over cylindrical samples in microgravity

Discipline
Sciences pour l'ingénieur

Spécialité
Énergétique

École doctorale
École Doctorale no. 353

Laboratoire/Partenaires de recherche
Aix-Marseille Université - IUSTI UMR 7343
Sorbonne Université - UMR CNRS 7190
Université de Lille - UMR 8207

Composition du jury

Stanislav STOLIAROV University of Maryland	Rapporteur
Thomas ROGAUME Université de Poitiers	Rapporteur
Olivier VAUQUELIN Université d'Aix-Marseille	Examinateur, Président du jury
Serge BOURBIGOT Université de Lille	Examinateur
Luis Fernando FIGUEIRA DA SILVA CNRS	Examinateur
Fatiha NMIRA EDF R&D	Examinatrice
Guillaume LEGROS Université d'Orléans	Co-directeur de thèse
Jean-Louis CONSALVI Université d'Aix-Marseille	Directeur de thèse

IUSTI LABORATOIRE AIX MARSEILLE UNIVERSITÉ CNRS

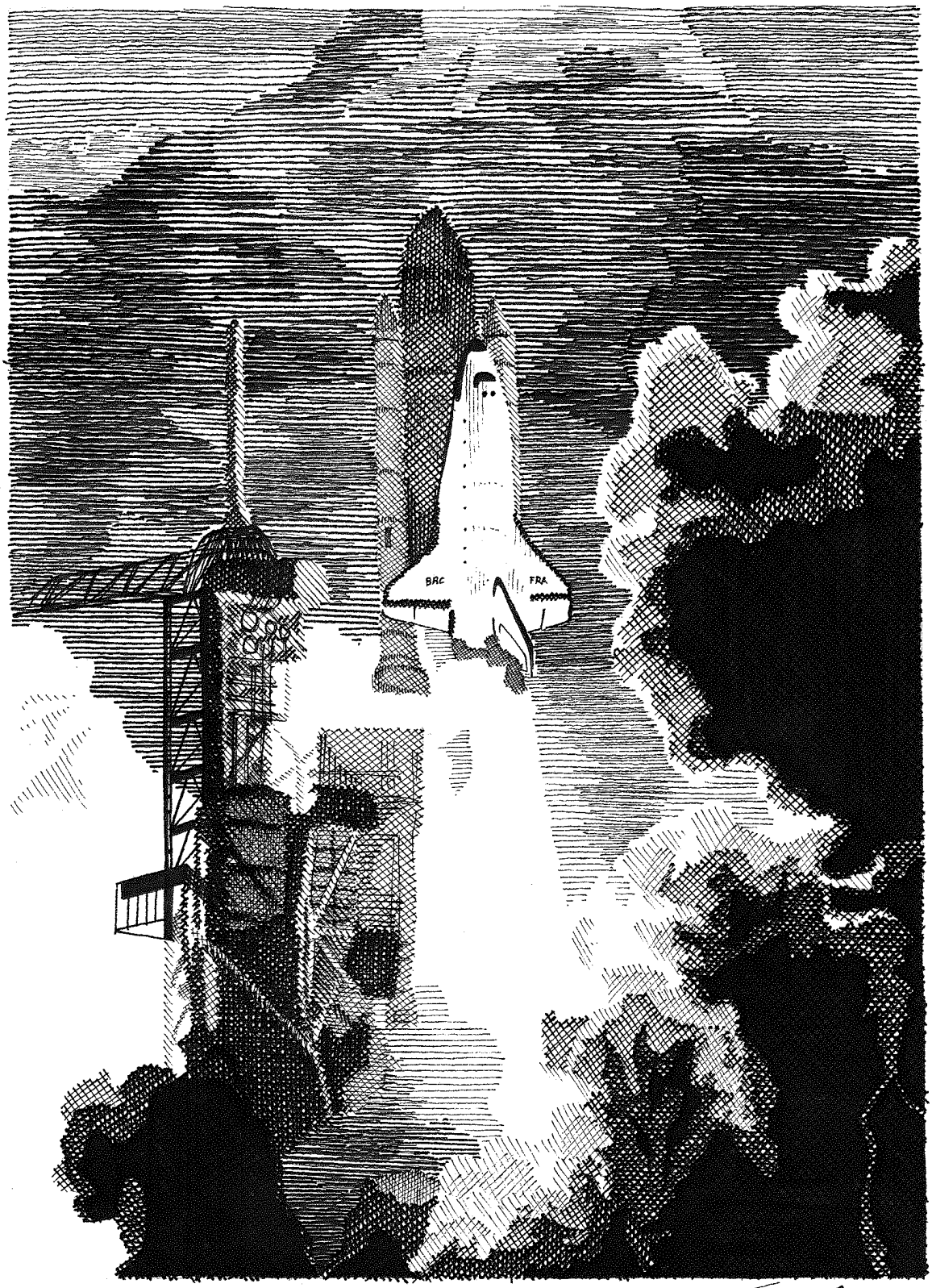

2022

I, undersigned, Alain Coimbra, hereby declare that the work presented in this manuscript is my own work, carried out under the scientific direction of Jean-Louis Consalvi, in accordance with the principles of honesty, integrity and responsibility inherent to the research mission. The research work and the writing of this manuscript have been carried out in compliance with both the french national charter for Research Integrity and the Aix-Marseille University charter on the fight against plagiarism.

This work has not been submitted previously either in this country or in another country in the same or in a similar version to any other examination body.

Marseille, 30 November 2022

Résumé

L'objectif principal de cette étude est de fournir des outils de modélisation pour étudier l'inflammabilité des polymères avec et sans retardateurs de feu dans un environnement de microgravité. Un accent particulier est mis sur le polyéthylène basse densité qui est utilisé comme revêtement pour simuler des fils électriques dans une configuration cible étudiée à l'échelle internationale pour évaluer et caractériser l'inflammabilité des fils électriques. Dans la première partie du manuscrit, un modèle d'ingénierie qui prédit la propagation de la flamme à contre-courant sur des fils cylindriques en microgravité est développé. Le modèle est appliqué pour interpréter les données expérimentales obtenues lors de vols paraboliques pour des fils composés d'un coeur métallique en nickel-chrome (NiCr) revêtue de polyéthylène de faible densité (LDPE) de différentes épaisseurs. Les hypothèses, étayées par des simulations numériques détaillées, réduisent le problème à la résolution des équations de transfert de chaleur pour le NiCr et le LDPE dans la région de pyrolyse et dans la région en amont du front de flamme. La vitesse de propagation de la flamme s'avère être contrôlé par deux paramètres mesurables du modèle: le flux de chaleur convectif de la flamme transféré au solide et la longueur de la diffusion de la chaleur près du front de flamme. Une procédure est proposée pour calibrer ces deux paramètres et le modèle ainsi calibré est validé par rapport aux données expérimentales pour différentes géométries de fils et conditions ambiantes. De plus, les mécanismes de transfert de chaleur en amont du front de pyrolyse sont ensuite étudiés, montrant leur nature complexe. La deuxième partie du manuscrit est consacrée au développement d'une stratégie de modélisation expérimentale et inverse pour construire des modèles de pyrolyse pour les matériaux condensés. Un modèle semi-empirique qui reproduit simultanément la décomposition thermique du matériau dans des expériences d'analyse thermogravimétrique (TGA), de calorimétrie différentielle à balayage (DSC) et de gazéification est développé. La stratégie de calibration consiste en la simulation inverse de ces expériences à l'échelle du laboratoire pour déterminer les propriétés apparentes: les paramètres cinétiques et thermodynamiques à partir des expériences TGA et DSC et les paramètres de transport à partir des expériences de gazéification d'échantillons thermiquement épais. L'approche est validée par la caractérisation de polymères précédemment étudiés dans la littérature avant d'être appliquée au LDPE pure et traité par retardateur de flamme intumescent actif en phase condensée composé de polyphosphate d'ammonium (APP) mélangé avec du pentaérythritol (PER) avec un rapport 3:1 (wt/wt). Un mécanisme de réaction semi-global pour la dégradation du LDPE/APP/PER est construit. Il se compose de deux réactions consécutives de premier ordre pour la fusion et la gazéification (pyrolyse) du LDPE et d'un mécanisme de réaction en 5 étapes pour l'APP/PER, qui a été conçu à partir des mécanismes

du processus d'intumescence. Le flux de chaleur de la flamme dans les expériences de cône calorimêtre est également évalué par simulation inverse de l'une des expériences. Les paramètres optimisés ainsi que le flux de chaleur radiatif rétrocédé par la flamme sont en accord avec la littérature et la robustesse du modèle est évaluée par une comparaison avec les données expérimentales pour une large gamme de taux de chauffage dans les expériences TGA et de flux de chaleur dans les expériences de cône calorimètre. Les temps d'inflammtion ainsiq ue l'évolution de la puissance de flamme présentent un accord satisfaisant avec les données expérimentales quelque soit les conditions de flux du cône.

Mots clés : inflammabilité des matériaux, polymères, retardateur de flamme intumescent actif, microgravité, modélisation

Abstract

The main objective of this study is to provide modeling tools to investigate flammability of polymers with and without fire retardants in microgravity environment. A special emphasis is put on low-density Polyethylene that is used as coating to simulate electrical wires in an international configuration for assessing and characterizing the flammability of electrical wires. In the first part of the manuscript, an engineering model that predicts the creeping flame spread over cylindrical wires in microgravity is developed. The model is applied to interpret experimental data obtained in parabolic flights for wires composed by a nickel-chromium (NiCr) metallic core coated by low-density polyethylene (LDPE) of different thicknesses. The assumptions, supported by detailed numerical simulations, reduces the problem to solving the heat transfer equations for both NiCr and LDPE in the pyrolysis region and in the region ahead of the flame front. The flame spread rate is found to be controlled by two model parameters, which are measurable from intrinsic material and ambient gas properties: the convective flame heat flux transferred to the solid ahead from the flame front and the gaseous thermal heat length near the flame front. A procedure is proposed to calibrate these two parameters and the calibrated model is validated against experimental data for different wire geometries and ambient conditions. In addition, the heat transfer mechanisms ahead of the pyrolysis front are then investigated, showing their complex nature. The second part of the manuscript is devoted to the development of an experimental and inverse modelling strategy to construct pyrolysis models for the condensed materials. A semi-empirical model that simultaneously reproduces the thermal decomposition of the material in thermogravimetric analysis (TGA), differential scanning calorimetry (DSC) and cone calorimeter experiments is developed. The calibration strategy consists in the inverse simulation of these specific lab-scale of experiments to determine apparent properties: the kinetic and thermodynamics parameters from TGA and DSC experiments and the transport parameters from gaseification experiments of thermally-thick samples. The approach is validated by characterizing polymers previously studied in the literature before being applied to neat LDPE and LDPE with a condensed-phase-active intumescent flame retardant consisting of ammonium polyphosphate (APP) mixed with pentaerythritol (PER) with ratio 3:1 (wt/wt). A semi-global reaction mechanism for the degradation of LDPE/APP/PER is built, which consists of two consecutive first-order reactions for the melting and gasification (pyrolysis) of LDPE and a 5-step reaction mechanism for APP/PER, which was designed driven by the mechanisms of the intumescence process. The flame heat flux in the cone calorimeter experiments is also evaluated by targeting the heat release rate (HRR) data in the optimization process of one of the cone calorimeter experiments. The optimized parameters and cone radiative heat flux

are in line with the literature and the robustness of the model is assessed by a comparison with the experimental data for a wide range of heating rates in TGA experiments and cone heat fluxes in the cone calorimeter experiments. Ignition times and peak and total HHRs are within the engineering accuracy whatever the flux conditions.

Keywords: creeping flame spread, electrical wire, microgravity, material flammability, thermal analysis, low-density polyethylene, intumescence, APP/PER

List of publications and participation in conferences

1. List of publications produced as part of the thesis project:
    - Coimbra A., Sarazin J., Bourbigot S., Legros G., and Consalvi J-L.. "A semi-global reaction mechanism for the thermal decomposition of low-density polyethylene blended with ammonium polyphosphate and pentaerythritol." Fire Safety Journal (2022): 103649.
    - Coimbra A., Sarazin J., Bourbigot S., Legros G., and Consalvi J-L.. "Thermal decomposition of low-density polyethylene: model development and parameterization over gasification experiments." Mediterranean Combustion Symposium (2022)
    - (manuscript submitted) Coimbra A., Li Y., Guibaud A., Citerne J-M., Legros G., Consalvi J-L.. "An engineering model for creeping flame spread over idealized electrical wires in microgravity." Comptes Rendus - Académie des Sciences - Mécanique (2022)
    - Consalvi, J-L., Guibaud A., Coimbra A., Citerne J-M., Legros G.. "Effects of oxygen depletion on soot production, emission and radiative heat transfer in opposed-flow flame spreading over insulated wire in microgravity." Combustion and Flame 230 (2021): 111447
    - Li Y., Guibaud A., Citerne J-M., Consalvi J-L., Coimbra A., Sarazin J., Bourbigot S., Torero J-L., Legros G.. "Effects of flame retardants on extinction limits, spread rate, and smoke release in opposed-flow flame spread over thin cylindrical polyethylene samples in microgravity." Proceedings of the Combustion Institute (2022)
2. Participation in conferences and summer schools during the thesis period
    - GDR CNRS MFA 2799 "Microgravité Fondamentale et Appliquée", 20 October 2020
    - GDR CNRS MFA 2799 "Microgravité Fondamentale et Appliquée", 02 to 04 November 2021
    - 3ème École des Sciences des Incendies et Applications École thématique du CNRS, May 30 to June 3, 2022
    - (after the PhD) 12th Mediterranean Combustion Symposium, January 2023

Nomenclature

A	Arrhenius pre-exponential factor, $1/s$
a	Cross section area, m^2
B	Mass transfer number
c	Heat capacity, $J/kg/K$
C	Corrective heat transfer factor for a cylindrical geometry
D	Thermal diffusivity, m^2/s
E	Arrhenius activation energy
E_{cc}	Heat transferred in the metallic core, W
$E_{gs,pr}$	Heat transferred from the flame to the polymer, W
$E_{gs,pr,flat}$	Heat transferred from the flame to the polymer in a flat slab, W
H	Heat of reaction, J/kg
h	Enthalpy, J/kg
$\bar{h}$	Heat transfer coefficient, $W/m^2/K$
I_{ex}	Radiative heat flux, W
I_{ex}^0	External radiation incident into the boundary, W
I_{rr}	Heat flux radiated by a material boundary, W
k	Thermal conductivity, $W/m/K$
k_r	Arrhenius rate of reaction, kg/s
L	Sample length, m
L_{vap}	Latent heat of vaporization, J/kg
L_m	Latent heat of melting (chapter 2), J/kg

L_g Preheat length, m

m Mass, kg

N_r Number of reactions

N_s Number of species

P Pressure, Pa

$\dot{q}''_{cone}$ Radiant heat flux from the heating system, W/m^2

$\dot{q}''_{flame}$ Flame heat feedback, $W/m^2/s$

$\dot{q}''_{fl,c}$ Convective heat flux transferred from the flame to the solid, $W/m^2/s$

q_x Heat conduction inside the condensed phase

r Radial direction

r_f Mass-to-fuel ratio

R Radius, m

R_{ex} Material surface reflectivity

$\bar{R}$ Molar gas constant, $J/kg/mol$

t Time, s

T Temperature, K

u Velocity, mm/s

$X_{O2,\infty}$ Oxygen mass fraction

x Axial coordinate, m

$Y_{O2,\infty}$ Oxygen volume fraction

Greek symbols

α absorption coefficient, $1/m$

Δ Volume, m^3

δ Insulation thickness, mm

ϵ Emissivity

μ Kinematic viscosity, $Pa.s$

ν Volume fraction

θ stoichiometric coefficient

ρ Density, kg/m^3

σ Stefan–Boltzmann constant, $W/m^2/K^4$

Subscripts

bottom Bottom surface of the sample

c Metallic core

g Gas phase

init Initial value

m Melting

max Maximum value

p Pyrolysis

res Residue

s Solid-phase

top Top surface of the sample

∞ Ambient conditions

0 Initial conditions

Superscripts

’ Per meter

” Per meter squared

n Time step

Acronyms

APP Ammonium polyphosphate

AP Ammonium polyphosphate/Pentaerythritol

CCE Competitive complex evolution

Cu Copper

DSC Differential scanning calorimetry

EG Expandable graphite

ETFE Ethylene-tetrafluoroethylene

FSR Flame spread rate

HDPE High-density polyethylene

HHR Heat release rate

HIPS High-impact polystyrene

IFR Intumescent flame retardant

LDPE Low-density polyethylene

LOC Limiting oxygen concentration

MLR Mass loss rate

NiCr Nickel-Chrome

PER Pentaerythritol

PLA Polylactic acid

PMMA Polymethyl methacrylate

POM Polyoxymethylene

RMSRE Root mean squared relative error

SCE Shuffled complex evolution algorithm

STA Simultaneous thermal analyser

TGA Thermogravimetric analysis

THEIC Tris(hydroxyethyl) isocyanurate

1g Normal gravity

μg Microgravity

Contents

List of Figures

List of Tables

1 Introduction

Sommaire

1.1 Context and objectives of the study

Even though space was explored as early as in the 4th century BC by ancient astronomers, it was only in the twentieth century that mankind was finally able to send probes and man himself to space. Space exploration, then, could be classified into three categories: astronomy, unmanned probes, and manned probes, where man is the explorer and common denominator. It is a combination of man's dream, technology, and understanding of science that has formed the basis of all forms of space exploration since its beginning.

The perspectives of crewed space exploration in the 21st century have never been more ambitious. Because of advances in science and technology, researchers are working on ever-more complex questions relating to data, discovery, and colonization. Due to changes in the global economy and in industry funding, private commercial enterprises are initiating projects that the government once led. As a consequence, the manned space exploration to the Moon, Mars and in deep space are bound to happen in the forthcoming decades [1, 2]. The adaptation to this changing reality will require significant effort from government and private organizations to develop the technology and capabilities to make long space voyages feasible. The scientific and engineering accomplishments required to attain these goals will give profound understanding of people, plants, materials and engineering systems, which will also benefit life on Earth [3].

In 2011, the American National Aeronautics and Space Administration (NASA) issued a report listing the fundamental topics in which developments in science and technology will be paramount for achieving further progress into the solar system exploration. A main topic widely discussed is that of fire safety [3]:

"Advances stemming from research on fire retardants, fire suppression, fire sensors, and combustion in microgravity that provide the basis for a comprehensive fire-safety system, greatly reducing the likelihood of a catastrophic event."

Even though they are rare events, fire hazards have occurred in a space vehicle and will occur again. The event of a fire in a confined environment with difficult external support such as a spacecraft can have devastating consequences, including loss of life, equipment and mission failure. Moreover, the absence of buoyant forces in microgravity alters the ignition and flame spread dynamics, making hypotheses deemed valid on Earth questionable. An accurate evaluation of materials' flammability in microgravity remains, therefore, a challenge.

At the present, materials considered for use in spacecraft are evaluated in flammability tests by NASA's fire safety standard STD-6001B [4]. They consist of a pass/fail test, considering worst-case scenarios of fire initiation and growth in normal gravity (1 g). Two main examples of such tests are illustrated in Fig. 1.1. The main material flammability test is Test 1, illustrated in Fig. 1.1(a). In this test, a vertical strip of material 5 cm wide and 33 cm long is set in a holder and ignited at the bottom-end, generating a condition of upward flame propagation. Similarly, test 4 consists of flammability evaluation of the coating of an electrical wire, as depicted in Fig. 1.1(b). A wire of approximately 120 mm long is typically used as test sample, inclined 15° to the vertical line, and similarly ignited from the bottom. Both tests consider that a material fails if the flame spread exceeds 6 cm or if a flaming debris drips into a piece of paper placed beneath the sample and causes its ignition [5].

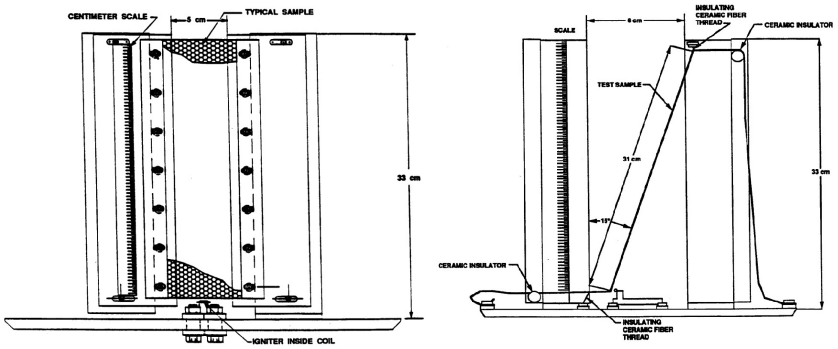

Figure 1.1: Typical material flammability experiments for spacecraft of NASA-STD-6001B (a) upward flame propagation (Test 1) (b) electric wire flammability (Test 4). Adapted from the literature [5].

A drawback of both depicted tests is that their results may be applicable only to the same conditions as those in the test, and no information on flammability characteristics of the material under spacecraft environment is provided [6]. For example, the limiting oxygen concentration (LOC) of a thin PMMA sheet has been shown to decrease from 17.0 in 1 g to 14.9 in a microgravity environment [7]. These limitations

suggest the need to develop new fire tests in such conditions, that seem to describe the actual worst case scenario of a fire risk.

In order to circumvent these limitations, our team has designed a novel experimental rig, custom-made for parabolic flights that simulate a microgravity environment. The Detection of Ignition and Mitigation Onboard for Non-Damaged Spacecrafts (DIAMONDS) is an international configuration for assessing and characterizing the flammability of electrical wires and cylindrical samples, in both normal and microgravity [8]. This sample configuration has been chosen since flame spread through electrical wires was identified as the main source of fire initiation and growth. A picture of the rig on board the airplane is shown in Fig. 1.2. A complete description of the DIAMONDS rig development and the microgravity conditions enabled by the parabolic flights may be found in a previous work [8].

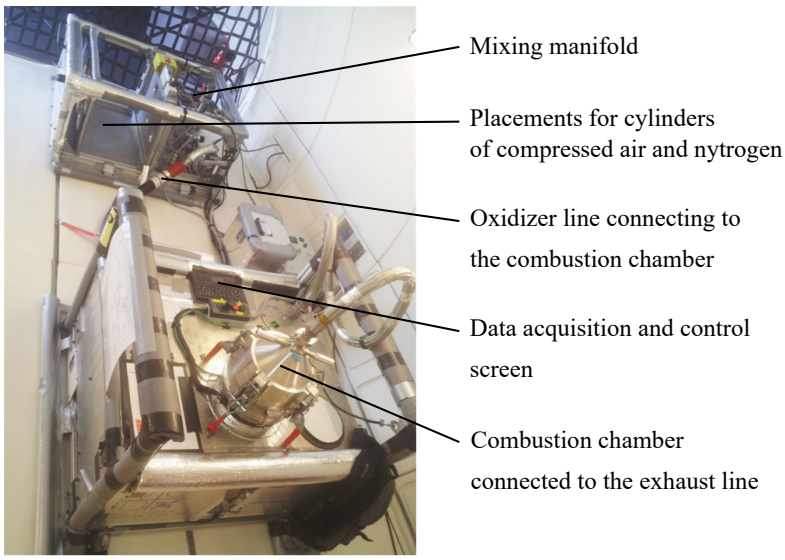

Figure 1.2: Picture of the DIAMONDS rig on board the Novespace airplane. Adapted from the PhD thesis of Augustin Guibaud [9].

The DIAMONDS rig has been used for assessing flammability of a wide variety of laboratory wire coatings and metallic cores. The material flammability can be characterized in terms of ignition, extinction, flame spread rate, among other factors, via visual observation techniques on a digital camera. An infrared camera has been also added, measuring the infrared energy emitted from the surface of samples. Concerning smoke production of a spreading flame, the broadband Modulated Absorption Emission (B-MAE) technique has been implemented to probe soot temperature and volume fraction [10]. All techniques combined have allowed a more comprehensive analysis of a material's flammability in conditions that simulate with more accuracy the environment of a spacecraft.

Fire retardants are an appealing solution for mitigating the fire risks posed by flammable materials. Such as discussed in NASA's report, the performance of flame

retardants commonly used on Earth are still poorly understood in microgravity. Using the DIAMONDS rig, our team recently investigated the flammability improvements of flame retardants in microgravity conditions. Two additives were considered: ammonium polyphosphate/pentaerythritol (AP) and expandable graphite (EG), both of which fit into the category of intumescent flame retardants (IFR). Upon heating in the presence of a flame, an expanded char layer is formed, inhibiting fire spread by slowing down heat and mass transfer between the gas and condensed phases and thus protecting the substrate material [11, 12, 13]. Images of flame spreading over a polymer wire with both flame retardants are show in Fig. 1.3, in both normal and microgravity conditions. It is clear from observation of Fig. 1.3 how the absence of buoyant forces changes the flame spread mechanics, alter the smoke production, and modifies performance of flame retardants.

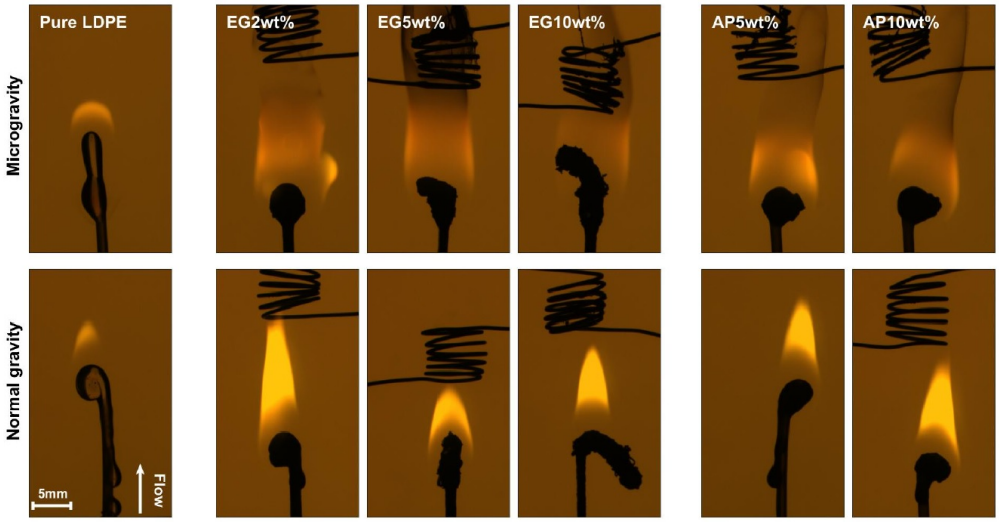

Figure 1.3: Backlighted frames imaging flame spread over cylindrical low-density polyethylene (LDPE) samples in an opposed-flow configuration, to investigate the impact of gravity and flame retardants with varying weight content.

The DIAMONDS experimental rig addresses therefore several issues that have been previously neglected in fire testings for use in a spacecraft. Large-scale fire tests in reduced gravity environments remain nevertheless impractical, and computer-based fire models are of high importance for studying the evolution of a fire in such conditions. This PhD thesis is then dedicated to building a computational environment that aids in the analysis and interpretation of flammability tests of solid fuels in microgravity conditions.

A literature review is first presented in the manuscript. Most notably, a historical review and state-of-the-art of flame spread in microgravity research is first presented. The methods for characterizing material flammability are then described, following by a review of polymeric flame retardant systems. Flame spread over solid fuels is a multi-physics problem, involving fluid dynamics, combustion, soot production,

radiative heat transfer, solid phase decomposition, etc. Models suitable for industrial applications must be resolved in large volumes and coarser resolution grids. These codes therefore cannot be emphasized on these detailed processes and their complex coupled nature and, instead, engineering solutions for flame spread and fire growth models remain appealing. In Chapter 2, an engineering approach to the problem of flame spread over an electric wire in microgravity is presented, and model validation and calibration are made from data obtained in the DIAMONDS rig. It is shown how the complex heat transfer mechanics, solid thermal decomposition and combustion chemistry can be translated into a simplified heat balance model that, once calibrated, accurately predicts the flame spread rate in polymer-coated metallic wires. On the other hand, the formulation of a more comprehensive flame spread model would require first a detailed condensed-phase thermal decomposition model. The framework to develop such semi-empirical pyrolysis models, as well as the procedure to obtain the model parameters and and its validation are presented in Chapter 3. This pyrolysis model is intended to be coupled with a gas-phase flame model, previously developed by our team, to predict the fuel mass flow rate into the flame and make the flame spread model fully predictive. In Chapter 4, the flammability of low-density polyethylene (LDPE) used in DIAMONDS is modeled, based on a series of gasification experiments. The thermal decomposition of the flame retardant AP, shown in Fig. 1.3, is similarly studied in Chapter 5. A reaction mechanism is developed for this complex materials and blends, as well as its changes in properties during the intumescent process as it slows down the burning. A complete pyrolysis model for the decomposition of the intumescent system LDPE/AP is developed, accurately reproducing a series of gasification experiments within engineering accuracy.

1.2 Literature review

1.2.1 Expressions for the opposing-flow flame spread over a solid fuel

A brief historical review of analytical studies related to the opposing-flow flame spread problem is presented in this section. The main purpose of this section is to present the previous efforts to characterize flame spread over solid fuels and determine the steady state flame spread rate (FSR).

The research over the opposed-flow flame spread problem has been thoroughly reviewed and technically discussed by Wichman 1992 [14]. The goal was to historically assess the main studies of the laboratory-scale opposing flow flame spread, also denoted as creeping flame spread. The first three decades of this study were presented, starting from the first theoretical works in the 1960s where the key physical features of the problem were first described. Areas where flame spread research were still unexplored have been pointed out, such as microgravity and solid-phase modeling. Since the focus had been mainly on the gas-phase processes, a detailed solid-phase modeling that relates material decomposition to the flame spread problem was still

lacking.

Two pioneering studies at the end of the 60s provided the fundamentals of of the opposed-flow flame spread problem. The first was proposed by McAlevy III et al. 1969 [15] where the second was proposed by De Ris 1969 [16] and is known as the DeRis theory in the literature. The latter is briefly described in this section, as it provides the basis of the semi-analytical methodology formulation used in Chapter 2. By proposing several simplifying assumptions and focusing on the fundamental heat transfer mechanisms, deRis correlates analytical expressions for the FSR, differentiating the characteristics of the thick and thin flame fuel bed. A simple model problem is proposed to analyze the flame quenching phenomena near the flame tip. Influences of the flame radiation (although only approximately theorized), the solid-fuel preheating prior to the flame arrival and boundary conditions along the vaporizing fuel surface were also discussed.

The burning process in the deRis model is illustrated in Fig. 1.4. The fuel solid slab is heated by the hot flame from ambient to the vaporization temperature, which characterizes the pyrolysis or flame front. The released fuel vapor mixes with the oxidizer from the opposed air stream and is ignited by the flame, producing heat that sustains the flame spread process.

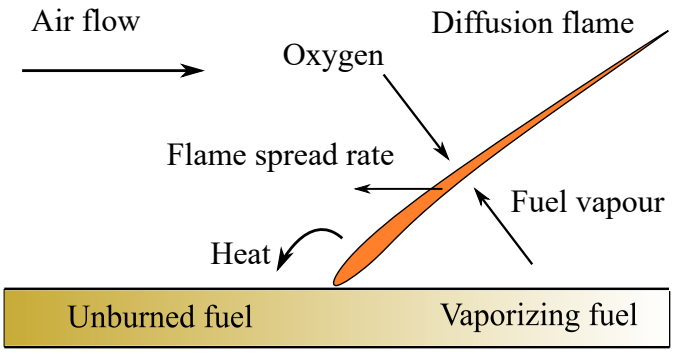

Figure 1.4: 2D physical description a flame spreading over a flat fuel bed - deRis model [16].

The model assumptions and simplifications of the deRis model as listed as follows:

1. The opposing oxidizer flow has a constant and uniform velocity (Oseen approximation).
2. The solid and gas phases have constant properties.
3. Lewis number is equal to 1, and mass diffusion of species is assumed to be driven only by specie concentration gradients.
4. The fuel bed vaporizes at constant temperature T_{vap}, which marks the flame front.

The correlation is obtained by analyzing heat and mass transfer in the region ahead of the pyrolysis front. The flame spread velocity is showed to be strongly influenced by the adiabatic stoichiometric flame temperature and the solid fuel thermal properties. For the thin flame sheet, the flame spread velocity u_p is expressed as:

$$\rho_s c_{p_s} \tau u_p (T_{vap} - T_\infty) = \sqrt{2} k_g (T_f - T_{vap}), \tag{1.1}$$

where τ, rho, c_p and k are the fuel thickness, density, heat capacity and thermal conductivity, respectively. The temperatures T_{vap}, T_∞ and T_f are the fuel vaporization temperature, ambient temperature and flame temperature, respectively. Subscripts s and g refer to solid and gas properties, respectively. The LHS of Eq. 1.1 is the heat transfer rate need to raise the fuel bed temperature to its vaporization temperature, whereas the RHS is the gas-phase conductive heat transfer rate from the flame forward to the unburned fuel bed. The deRis analysis was then extended considering the effects of fuel-bed conduction. For the thick flame sheet, the flame spread formulation is expressed as:

$$\frac{\rho_s c_{p_s} k_s}{\rho_g c_{p_g} k_g} \frac{u_p}{u_\infty} = \left(\frac{T_f - T_{vap}}{T_{vap} - T_\infty} + \frac{2R_1 F(2k_g/\rho_g c_{p_g} u_\infty l_1)}{\rho_g c_{p_g} u_\infty (T_{vap} - T_\infty)} + \frac{2R_2}{\pi \rho_g c_{p_g} u_\infty (T_{vap} - T_\infty)} \right)^2, \tag{1.2}$$

where R_1, R_2 and l_1 are constants associated to the radiative heat flux received by the fuel bed from the flame. The function F is solved using an eigenvalue relationship, described in Ref. [17].

Although further experimental verification was required, and analysis of the roles of reaction kinetics and opposed oxidizing flow velocity were lacking, the deRis model represented a first step towards practical, useful correlations that allow the discussion of key physical elements that control flame spread.

Further theoretical interpretations of flame spread over a combustible surface have been presented by Delichatsios and colleagues [18, 19, 20]. An energy balance analysis on the solid phase near the pyrolysis front over a flat fuel surface was developed, as shown in Fig. 1.5. An insight on two important quantities that dictate the flame spread behavior was made. The gaseous thermal diffusion length near the flame front, L_g, was estimated by using an Oseen approximation and is related to the opposing air-flow velocity. A uniform conductive heat flux over a flat slab in the pyrolysing region, $E_{gs,pr}$, was deduced from an exact solution of the heat problem assuming infinitely fast kinetics and Oseen approximation. The model parameters can be expressed as:

$$L_g = \frac{D_g}{u_\infty}; \tag{1.3}$$

$$E_{(gs,pr,flat)} = k_g \frac{[B - r_f]L_{vap}}{c_g}, \tag{1.4}$$

where D_g is the gas-phase thermal diffusivity. The symbols B, r_f and L_{vap} represent the mass transfer number, the stoichiometric fuel-to-air mass ratio, and the latent heat of vaporization.

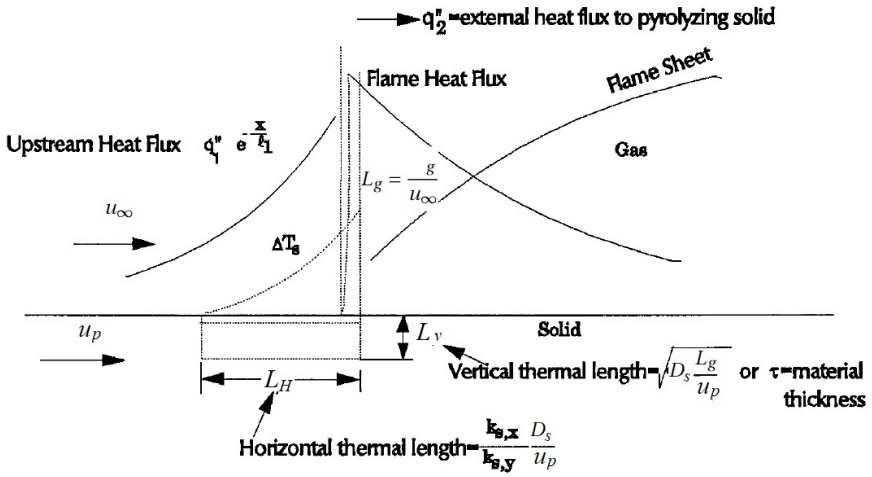

Figure 1.5: A diagram for opposed flow flame spread illustrating length scales, heat fluxes, and temperatures. Taken from Delichatsios 1996 [18].

In the Delichatsios model, the FSR could be deduced from the heat transfer rate per unit sample width from the flame leading edge to the solid phase from ambient temperature to vaporization temperature. For a thermally thick solid, the FSR could be expressed as:

$$\left(\frac{T_{vap} - T_\infty}{E_{gs,pr,flat}}\right)^2 (\rho_s c_{p_s} k_s) u_p L_g = 1, \tag{1.5}$$

and for a thermally thin solid, the resulting FSR was calculated as:

$$\left(\frac{T_{vap} - T_\infty}{E_{gs,pr,flat}}\right)^2 (\rho_s c_{p_s} k_s) u_p L_g = \frac{k_s (T_{vap} - T_\infty)}{E_{gs,pr,flat}} \frac{L_g}{\tau}. \tag{1.6}$$

The Delichatsios semi-analytical expressions for creeping flame spread were then extended to flame spread parallel over a fuel cylinder, such as along a wire or cable insulation [19]. The objective was to provide a relation between flame spread over a flat surface and over a cylindrical geometry, through a correction factor c in the form of $E_{gs,pr} = c \times E_{gs,pr,flat}$, where c is independent on material flammability characteristics.

The cylinder curvature was found to increase the flame heat transfer in comparison with the flat slab, and the rate of temperature rise within solid was faster because there was less material within the cylinder per unit length around the cylinder that needs to be heated than for the flat surface. The correction factor was expressed as:

$$c = \frac{\sqrt{\pi}\frac{L_g}{R_s}}{\ln(1+\sqrt{\pi}L_g/R_s)}, \tag{1.7}$$

where R_s is the outer cylinder fuel radius.

The Delichatsios works provided an engineering analytical solution for the flame spread problem, showing that the flame spread rate could be characterized by measurable material's intrinsic properties and ambient conditions. Methods for characterizing the modeled parameters were also presented. A limitation of this model is an over-prediction on the modelling of the flame heat flux $E_{gs,pr,flat}$, which is still a consequence of the deRis assumption of infinitely-fast combustion kinetics.

As well as their cylindrical geometry, a unique feature in wires is the presence of a metal conductor inside the flammable material. The metallic core, as discussed in the next section, is known to modify the heat transfer pattern within the solid and, therefore, influences the FSR. An expansion of the Delichatsios' model is then required to account for different heat transfers between the flammable solid and the metallic core.

Concerning the configuration of an electrical wire, an analytical model to the downward flame spread over a cylindrical polymer-coated, metallic wire was formulated by Konno and colleagues [21]. A description of the heat transfer processes in the condensed phase that play a role on the resulting FSR is given in Fig. 1.6. In their analysis, the burning wire was divided into three zones: a preheat zone, a pyrolysis zone and a burned zone (see Fig. 1.6). Some simplifications of the model are listed as follows:

1. Both the insulation and core wire are thin enough for thermally thin assumptions to be applicable.

2. The melting process and deformation of the insulation are ignored.

3. The radiation from the flame is ignored.

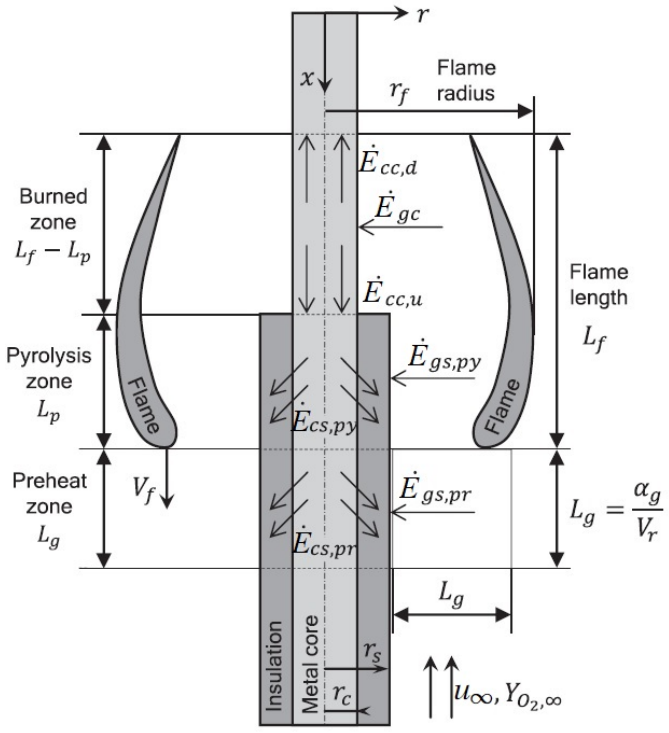

Figure 1.6: description of downward flame spread over an electrical wire. Taken from Konno et al. 2019 [21].

Such as the previously described models, the FSR can be analyzed in terms of the ratio of the enthalpy required to preheat the unburned fuel up to pyrolysis temperature to the thermal input to the unburned fuel. Two dominant heating mechanisms are present on the thermal input at the preheat zone, as illustrated in Fig. 1.6: the gas-phase heat transfer from the flame to the fuel surface, $E_{gs,pr}$, and the conduction from the metallic core, $E_{cs,pr}$. $E_{gs,pr}$ is calculated as follows [22]:

$$E_{gs,pr} = \frac{P_s L_g k_g (T_f - T_{vap})}{R_s \ln(1 + L_g/R_s)} \tag{1.8}$$

where P is the outer insulation perimeter and subcript s refers to the insulation. $E_{cs,pr}$ was calculated from two heat transfers in the form of $E_{cs,pr} = E_{cc,u} - E_{cs,py}$, where $E_{cc,u}$ is the heat conduction inside the metal core in the upstream axial direction and $E_{cs,py}$ is the heat loss from the metal core to the insulation in the pyrolysis zone. The FSR could then be expressed as:

$$u_p = \frac{E_{gs,pr} + E_{cc,u} - E_{cs,py}}{(A_s \rho_s c_{p_s} + A_c \rho_c c_{p_c})(T_{vap} - T_\infty)}, \tag{1.9}$$

where the subscripts s and c denote the polymer and metallic core, respectively. $E_{cc,u}$

and $E_{cs,py}$ were modelled as:

$$E_{cc,u} = a_c k_c \frac{(T^* - T_{vap})}{L_p}; \tag{1.10}$$

$$E_{cs,py} = \frac{P_c L_p k_s (T^* - T_{vap})}{2R_c \ln(R_s/R_c)}; \tag{1.11}$$

where the subscript c denotes the metallic core, and T^* is a characteristic core temperature.

1.2.2 Flame spread over electrical wires in microgravity

The literature concerning flame spread over wires is reviewed in this section. The main focus is brought to works that consider the microgravity condition (μ g), although some of the described works use the configuration of flame spread in normal gravity (1 g). In those cases, the typical configuration of study is downward flame spread in 1 g, which resembles the configuration of opposed-flow flame spread in μ g used in this work due to the generated opposed vertical, upwards buoyant flow.

The relevant parameters that control flame spread over wires in microgravity can be roughly grouped in two categories. First, the effect of ambient conditions and buoyancy forces on the flammability of wires is reviewed, such as ambient pressure, opposing air flow velocity and oxygen concentration. Then studies dedicated to understanding the role of the metallic core, as well as wire natures, on the heat mechanics, extinction and FSR are reviewed. In the third subsection, studies performed using the DIAMONDS rig are discussed. The main points of these studies are summarized in Table 1.1, and their main conclusions are presented in this section.

The effect of ambient conditions

The FSR of ethylene-tetrafluoroethylene (ETFE) wires was measured in microgravity and in downward spread in normal gravity by Fujita et al. 2000 [23]. The FSR was found to be significantly higher in almost all tested cases in μg. This was attributed to much thicker preheat zones, as well as decreased radiative heat losses in microgravity.

The similarity of a sub-atmospheric pressure with a weak imposed flow with a real microgravity environment was discussed by Nakamura et al. 2008 [24]. A polyethylene coated NiCr wire was used as a test combustible sample in ambient air in a pressure range of ($20 < P < 101$ kPa). As expected, the flame shape and behavior were largely influenced by the pressure, as a wider and less luminous flame was observed with the decreasing pressure. The FSR was found to slightly increase with the decreasing pressure, whereas the heat release rate seemed to decrease. The combined increase in dripping frequency and FSR made sub-atmospheric pressure more dangerous when compared to atmospheric pressure in terms of fire hazards. The flame shape and FSR with a weak opposing air flow correlated reasonably well with sub-atmospheric

pressure and microgravity environment.

The suggestion that a microgravity flame could be simulated by reducing buoyancy effects in a decreased pressure environment was further assessed by Thomsen et al. 2019 [25]. The effect of pressure and gravity on the burning of a thin composite fabric (Sibal) in upward/concurrent flame spread was studied. It was found that the FSR and flame luminosity decreased with the reduced pressure. At around $P = 30$ kPa, similar FSRs were obtained with microgravity conditions.

Further studies on the effect of reduced ambient pressures on the flame spread of LDPE-coated copper wires was further investigated by Gagnon et al. 2021 [26]. It was shown that both the FSR and the molten LDPE dripping frequency decreased with the decreased pressure and with an increased opposing air flow. It was nevertheless observed that other studies with different core materials or dimensions yielded different results.

A study on the effect of pressure on the flame spread mechanism has been performed by Zhao et al. 2017 [27], using polyethylene-insulated copper wires, in downward flame spread at 1g. In a range from sub-atmospheric pressure ($P = 60$ kPa) to elevated pressure ($P = 500$ kPa), the flame shape, the molten polyethylene dripping and the FSR were investigated. The dripping event decreased significantly with the increasing pressure, and ceased completely above $P = 200$ kPa. The flame width monotonically decreased with increasing pressure, whereas the flame height firstly increased and then decreased, reaching a maximum value at $P = 200$ kPa. Most importantly, the FSR was shown to increase with the ambient pressure. Two distinct heat transfers are analyzed in this configuration: the flame convective and radiative heat and the conductive heat along the copper wire. The heat transfer from the flame was observed to play a dominant role in the flame spread process whatever the pressure. Indeed, both convective and radiative heat transfer terms increase with the increasing pressure, whereas heat conduction from the metal to the insulation is shown to decrease.

Further studies regarding flame spread behavior over solid cylindrical fuels have been performed by Zhao et al. 2019 [28]. Considering polyethylene and polymethylmethacrylate (PMMA), the fuel burning rates show an increasing tendency with pressure as $P^{0.6}$ and $P^{0.79}$ for PMMA and polyethylene, respectively. The flame spread rate also shows this tendency with PMMA and polyethylene FSR increasing as $P^{0.5}$.

Comparisons of flammability limits between 1g and μg were made by Osorio et al. 2015 [29], using copper wires with an ETFE insulation. The limiting oxygen concentrations were experimentally measured at oxygen concentrations ranging from 20% to 32% and external radiant fluxes from 0 to 25 kW m^{-2}. Microgravity showed, again, reduced heat losses due to the absence of natural convection, allowing the flame to propagate in lower oxygen concentrations, and it presented a larger impact in ETFE than in polyethylene.

The metallic core

A unique feature in the flame spread over electric wires is the presence of an inert, high thermal conductivity metallic core inside the flammable polymer coating. The

metallic core alters the heat mechanism within the wire and has a direct impact on the FSR and flame extinction mechanics [30].

The role of the metallic core on the heat transfer mechanisms of flame spread in microgravity was investigated theoretically by Umemura et al. 2002 [31]. A mathematical model for steady state flame spread over wire insulation was proposed, in which the radiation effects are neglected in order to explore the effect of the wire as a heating or cooling medium on the burning wire coating (ETFE-coated copper wires). The proposed model consisted of a spherical flame burning around a single point of fuel source, located at the edge of the uncoated wire (see Fig. 1.7). The metallic wire with a large thermal conductivity was shown to act as both a heat sink and a heat source on the burning of wire coating. The uncoated copper wire inside of the flame acted as a heat sink, receiving heat from the surrounding hot gas and transferring part of it to the coating to enhance gasification. On the other hand, at the vicinity of the flame front, the flame extinguished locally due to heat losses to the copper wire which acted as a heat sink.

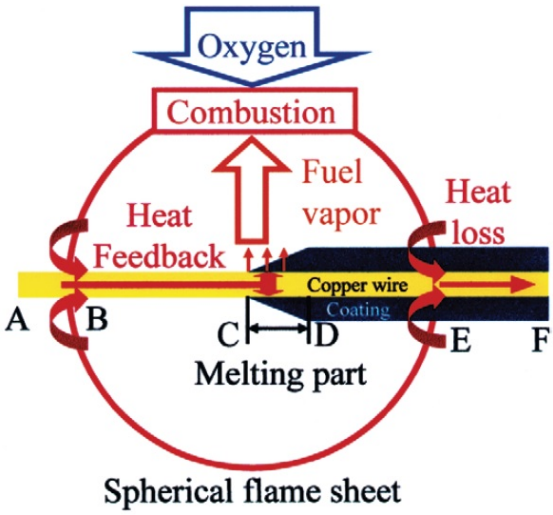

Figure 1.7: Proposed mechanism for the formation of spherical flame in electric wire insulation burning in microgravity. Taken from Umemura et al. 2002 [31].

Conditions of flame extinction limits in wires were experimentally measured by Takahashi et al. 2013 [32], using low-density polyethylene (LDPE) insulated Nickel-chrome (NiCr) and Copper (Cu) wire samples. The effect of oxygen levels and external opposed flow conditions from 60 to 200 mm/s in 1g and μg were considered. The limiting oxygen concentration (LOC) of the high thermal conductivity core (Cu) was found to be higher than that of a low conductivity core (NiCr), even though spread rates were considerably higher on the former configuration. This was attributed to the fact that heat losses that passed through the core wire were much larger for Cu core wire than for NiCr core wire. The μg results showed lower LOC levels in comparison with 1g mainly due to the absence of natural convection that drives away the flame

heat, resulting in an increased heating of the unburned insulation.

The observation of the volume change of the molten insulation provides insights over the flame spread mechanisms, such as the amount of fuel supplied to the flame and the amount of heat feedback from the flame to the insulation. The unsteady molten insulation volume change was investigated in drop towers, providing 4.5 s of microgravity (10^{-5} g) by Takahashi et al. 2013 [33], using samples of LDPE insulated NiCr wires. The insulation volume change rate was found to decrease when increasing the opposed air flow velocity. Moreover, the pyrolysis volume rate increased monotonically with the air velocity, which was attributed to an increase in the heat input to the molten insulation.

The effect of flow direction on the mechanism of extinction limit of flame spread over insulated wires was investigated by Nagachi et al. 2017 [34]. The LOC was measured on the flame spread of thick polyethylene insulated NiCr and Cu wires in a range of $-200 < V_g < -50$ mm/s (opposed air flow) to $50 < V_g < 200$ mm/s (concurrent air flow). The LOC was lower in concurrent flow conditions than in opposed flow, which was also observed previously for flame spread over flat plates Kumar et al. 2003 [35]. The measured LOC was similar for NiCr and Cu. This was attributed to the thick insulation, which may minimize the effect of the wire.

The flame spread behavior over wires in a concurrent flow in microgravity was studied by Nagachi et al. 2019 [36]. A steady state flame spread was shown to be achievable for the concurrent flow case, and an analytical model of heat balance was proposed to explain this condition. The FSR was shown to increase with the concurrent oxidizer flow velocity, and it was also shown to be greater for the higher thermal conductivity metallic core (Cu over NiCr).

The effect of pressure on flammability of LDPE coated NiCr wires was also investigated by Nagachi et al. 2020 [37]. The LOC increased with the decreasing pressure in the studied range. This was attributed to the radiation loss from the wire, which increased as the ambient pressure decreased.

Further investigations of the effect of the metallic core on the extinction phenomena in electric wires were done by Konno et al. 2020 [38]. The FSR was shown to increase with the ambient oxygen concentration for Cu, Fe and NiCr wires, with oxygen content ranging from 16 to 25%. The FSR was also increased when increasing the conductivity of the wire core. Temperature profiles along the wire were also measured, leading to previous experimental observations of the LOC in high-conductivity and low-conductivity wires [32]. It was shown that reducing the FSR made it harder to sustain the flame spread, as heat loss at the surface of the unburned insulation increased, leading to quenching extinction. Simultaneously, an increase in the core conductivity also led to increased heat losses near the flame front, due to the greater effect of the core as a cooling medium.

The effect of the metallic core diameter, microgravity and external radiant heat fluxes on the wire flammability was experimentally studied by Konno et al. 2020 [39]. The wire with the thicker core ($d_c = 2.5$ mm) was less flammable than that with the thinner one ($d_c = 0.7$ mm), which was assumed to be due to the increased heat sink effect of the core. Nevertheless, the effect of wire dimensions is a complex issue and

different parameters that have a simultaneous impact on wire flammability have been identified:

- The insulation thickness, which impacts heat gains and/or losses to the metal core.
- The core diameter, which controls the temperature distribution along the wire and contact surface between the core and insulation.
- The total outer diameter, which influences the curvature of the external surface and modifies external heat fluxes [19].

Regarding the gravity effect, both tested wires were less flammable under microgravity, which is a conclusion that diverged from previous observations.

DIAMONDS rig

The flame spread in multiple, parallel wires in concurrent and opposed flow was studied by Citerne et al. 2016 [8], using the DIAMONDS rig, presented in the previous section. It presented a first step towards the understanding of the mechanisms that lead to heat exchange between wires and their resulting influence on flame spread. In addition, lower FSR were observed when decreasing the oxidizer flow velocity.

Experimental measurements on the DIAMONDS rig and numerical studies were performed in a configuration of non-buoyant opposed-flow flame spread over LDPE-insulated NiCr wires by Guibaud et al. 2020 [40]. Considering a O2/N2 oxidizer composed of 19% of oxygen in volume in an opposed flow velocity of 200 mm/s, visual optics methods were used to measure the flame spread rate, pyrolysis rate, stand-off distance, soot volume fraction and soot temperature. The stand-off distance was defined as the radial distance between the wire surface and the flame sheet. Computationally, measured spread and pyrolysis rates were used as input and equations for mass, momentum, species, energy, and soot number density and mass fraction were solved in an axisymmetric flame-fixed coordinate system. Moreover, a simple polyethylene degradation model and a state-of-the-art radiation model were applied. The simplifying assumption of pure ethylene as a pyrolysis product was proved effective for LDPE. Furthermore, the acetylene-benzene based soot model could be, with minor modifications, applied to polyethylene. For this studied configuration, soot radiation was shown to prevail over the gas phase radiation. The flame radiation self-absorption contributed to less than 5% of calculated values for incident radiative flux along the molten ball, thus validating the optically-thin approximation. Concerning the radiative heat flux balance, measurements showed that the re-radiation along the LPDE pyrolyzing surface as well as virgin phase was higher than the flame incident radiative flux. This showed that the flame spread was ensured by the flame convective heat and conduction inside the condensed material and metallic wire. Furthermore, numerical results showed non-uniform radial temperature profiles throughout the LDPE coating, invalidating the widely used thermally-thin assumption.

The technique of Modulated Absorption/Emission (B-MAE) was developed to measure soot temperature and volume fraction within the spreading flames [10, 41]. Soot-related radiative heat transfer was quantified. A mapping of radiative losses was drawn along the burning wire surface profile, which was used as a novel experimental approach, where soot radiative heat feedback to the wire could be measured. These detailed quantitative measurements have assisted on giving insight on the dominant heat transfers and mechanisms that drive flame spread in microgravity. The soot-related heat that was radiated back to the wire represented up to 19% of the heat required to fully pyrolyze the solid LDPE coating in microgravity, which was four times the value computed for a similar configuration in normal gravity.

The role of the three basic ambient conditions in the flame spread of wires in microgravity was documented by Guibaud et al. 2020 [42], and will be the basis of the model validation in Chapter 2. Experiments with oxygen content ranging from 18 to 21%, oxidizer flow velocity ranging from 100 to 200 mm/s, and pressure ranging from 51 kPa to 142 kPa were conducted using the DIAMONDS rig, in parabolic flights. The oxygen level was shown to have a direct impact on the FSR. Assuming ethylene as the only pyrolysis product, a one-step chemical reaction in the form of $F + SO_x \rightarrow (1+S)P$, where the oxidizer/fuel mass ratio S was a decreasing function of the oxygen content $x_{(O_2,\infty)}$ was assumed. The impact of the oxygen content on the flame spread u_p was then shown in Fig. 1.8. Indeed, the spread rate increases with the oxygen content, by an average power-law exponent of $\beta_{u_p}^{(1+S)} = -1.06 \pm 0.73$.

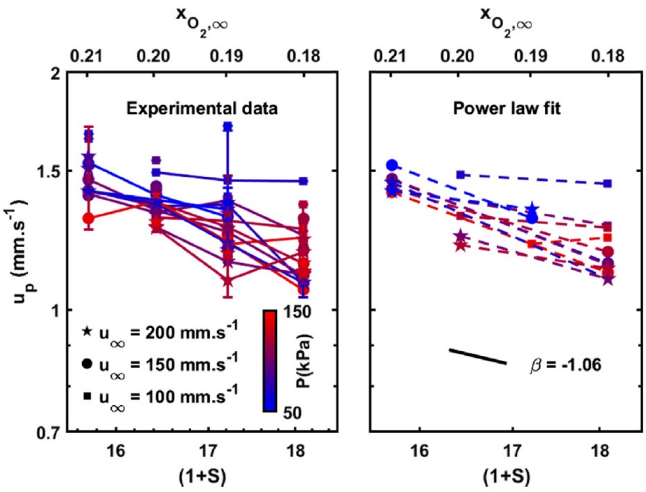

Figure 1.8: Experimental data of flame spread rate as a function of (1+S) (left). Symbols represent the flow velocity conditions, whereas colors represent pressure levels. Averaging over 13 sets of measurements, the fitted power law exponent is -1.06, as illustrated by the dark line (right), with standard deviation of 0.73. Adapted from Guibaud et al. 2020 [42].

The FSR behavior was further depicted as a function of the pressure and opposed flow velocity in Fig. 1.9. The flame spread velocity correlated with the pressure via

a power law of $\beta_{u_p}^{P} = -0.09 \pm 0.14$, whereas it correlated with the opposed oxidizer velocity by $\beta_{u_p}^{u_\infty} = -0.12 \pm 0.13$. This indicated that ambient pressure and opposed air velocities play little to no influence on the flame spread within these investigated ranges.

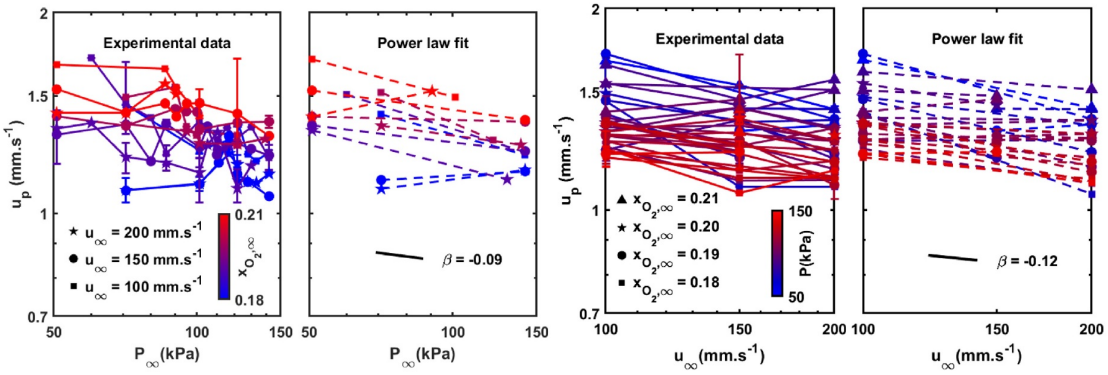

Figure 1.9: Flame spread rate as a function of the pressure (left) and flow velocity (right). Adapted from Guibaud et al. 2020 [42].

1.2.3 Methods for characterizing flammability of polymers

In the previous section, an extensive line of studies on the effects of air flow velocity, gas phase oxygen concentration, external thermal radiation, and gravity on the combustion of polymers was presented. However, the development of a comprehensive model that describes the degradation process of polymers would involve a complex coupling between the energy feedback from a flame to the solid surface and the generation of degradation products from its gasification. As a consequence of this complexity, the effects of polymer characteristics on combustion and flammability are not nearly as well understood as those in the gas phase. The equations that describe the condensed phase cannot be derived without understanding the governing chemical and physical processes that control the gasification of polymers. This section describes a literature survey on the development of pyrolysis models for fire applications.

Pyrolysis modeling

The work of Henderson et al. 1985 [43] represented some of the earliest efforts to model a polymer response undergoing thermal decomposition. The model was based on a one-dimensional conservation of energy and mass, and it was experimentally tested by measuring the temperature profiles during decomposition of a glass-filled phenol-formaldehyde polymer composite. The material apparent properties required as input for the model were thermal conductivity (k) of the virgin and char components, heat of decomposition (H), and the kinetic parameters (A and

E). These properties were experimentally measured: k was measured from the line-source technique, H was calculated from differential scanning calorimetry (DSC) and A and E were calculated from thermogravimetric data (TGA). The resulting thermal model was found to satisfactorily predict the thermal response of a polymer composite undergoing decomposition.

Following this early generation of polymer decomposition studies, the degradation of PMMA was modeled by Vovelle et al. 1987 [44]. The polymer sample was subjected to external radiant fluxes, which simulate the external heat feedback from a fire, and the mass loss rate and surface temperature profile were monitored. The material apparent properties were measured in a similar manner to the work of Henderson et al. 1985 [43]. The resulting model predicted accurately the polymer decomposition behavior.

The simple decomposition models previously described considered solids in an aggregate manner, with one (or few) decomposition reactions and physical processes. As a consequence, modeling polymers that present a more complex decomposition behaviour, or modeling multi-component blends were still impractical. With the advance in computational power in the last decades, a growing interest in CFD simulations of fire has also brought an interest to the development of sub-models that can provide information about the solid phase decomposition of more complex polymer systems. An example of two comprehensive pyrolysis models are Thermakin [45] and Gpyro [46].

Thermakin is a numerical tool developed by Stoliarov et al. 2014 [45] that computes the transient rate of gaseous fuel production from fundamental physical and chemical properties of pyrolysable solids in a two-dimensional configuration, suitable for simulation of flame spread and fire growth. It is capable of solving first- and second-order reactions, including those between two different reactants, making it an attractive solution for studying the decomposition of multi-blend systems. Gpyro has been developed by Lautenberger et al. 2009 [46] within the Fire Dynamics Simulator [47]. The model can be applied to non-charring and charring solids, composites, intumescent coatings, and smolder in porous media. It can be used as a standalone computer program or as a boundary condition in a larger-scale fire model, quantifying the rate at which solid combustible surfaces heat up and generate gaseous pyrolysate.

Within the Thermakin framework, a pyrolysis model that accurately reproduced the mass loss and temperature evolution of fire calorimetry data of simple polymers was developed by Stoliarov et al. 2009 [48]. The relevant material properties were experimentally measured and/or retrieved from literature.

Parameter determination for pyrolysis modeling

From the earlier studies to the most recent comprehensive pyrolysis codes, the presented works are within the category of semi-empirical models. They correlate the decomposition behavior of polymers to their intrinsic properties, often related to decomposition kinetics, heat and mass transfer. In cases of more complex systems, such as flame retardants, the amount of model input parameters may be too numerous, and their experimental determination becomes impractical due to the coupled nature

of physical and chemical processes. In order to overcome this difficulty, the processes of parameter estimation based on experimental databases have been reviewed by Kim et al. 2015 [49]. It is suggested that parameters estimation should follow four guidelines and approaches:

1. Parameter estimation is about being consistent, applying engineering commonsense
2. Parameter estimation is conducted by breaking down the problem into groups of unknowns of similar characters and considering them separately
3. Parameter estimation is conducted with consideration to an appropriate complexity in model set-up using certain approximations for simplifications
4. Parameter estimation is conducted with direct measurements of parameters with independent experiments, literature search and/or numerical optimization paired with certain pyrolysis models

An optimal determination of materials flammability properties for input in modern pyrolysis models involves a combination of experimental measurements, literature data and inverse numerical modelling. An example of this process is given in a flowchart for visualisation purposes in Fig. 1.10.

Successfully applying the proposed procedure for parameter estimation, Stoliarov and colleagues developed a systematic methodology for measuring the kinetics and thermodynamics of the thermal degradation that occur during the heating of thermoplastic materials [50]. Inverse numerical modelling was used to fit the heat flow and mass loss rates measured using TGA and DSC data from gasification of polymer samples exposed to radiant heat. The Arrhenius parameters that describe the kinetics of the material thermal decomposition were determined, as well as its heat capacities, heat of melting and heats of decomposition of the condensed-phase reactions. The gathered material properties of these studies were used in subsequent studies. A one-dimensional model was fitted into a nearly one-dimensional configuration of heating conditions of a cone calorimeter that supplies the polymeric samples with 20-70 kW m^{-2} of radiant heat flux [51]. The back surface temperature and mass loss rate of burning polymeric samples were measured as a function of time, and the thermal transport properties were determined by manually fitting the model with the experimental data. A thorough description of this strategy is presented in Chapter 3 and is subsequently applied to our purposes in Chapters 4 and 5.

The radiative absorption coefficient is an important material property for accurately computing the energy input to the burning material. The absorption coefficient and reflectance of common polymers for infrared radiation from a high temperature source was measured by Linteris et al. 2012 [52] using two distinct experimental methods. The first method used a radiant heater, together with a broadband thermal detector, and the second method used a spectral technique, both measuring the transmittance as a function of sample thickness. The resulting properties were obtained from deriving

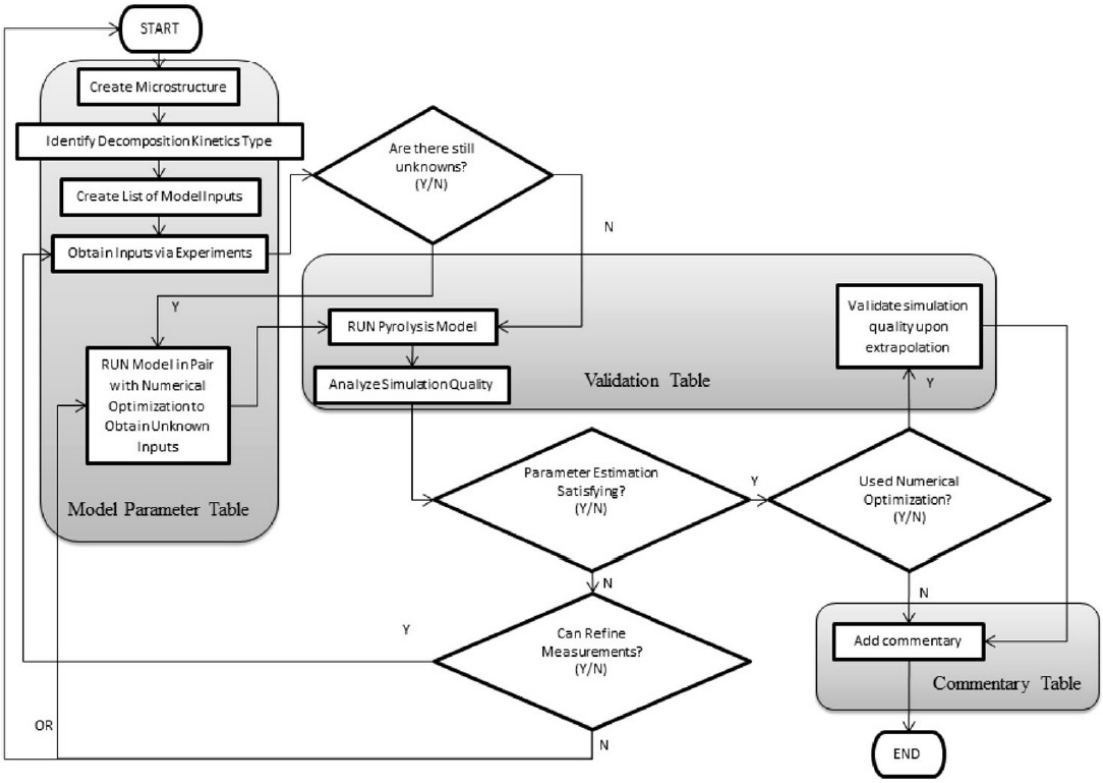

Figure 1.10: Flow chart of parameter estimation for comprehensive pyrolysis models. Taken from Kim et al. 2015 [49].

the Beer-Lambert's law for attenuation of radiation within a medium. This property was shown to significantly affect the material ignition time and burning rate, and it was also shown to be dependent on the material thickness.

In cases of numerous fitting parameters, inverse modeling of gasification tests are an attractive and, sometimes, a necessary solution. Optimization algorithms are often used to obtain the best possible agreement between simulations and experiments by adjusting the input parameters (material properties). An evaluation of the accuracy, efficiency and robustness of optimization algorithms for determining solid fuel properties for fire models in inverse-modeling of bench-scale pyrolysis tests was done by Chaos et al. 2011 [53]. It was shown that the Complex Shuffed Evolution algorithm (SCE) was highly flexible, efficient, and robust as well as superior to other evolutionary algorithms available in the literature for providing the desired parameters against virtual mass loss rate curves from calorimetry models. A step-by-step procedure of this algorithm will be explained in Section 3.1.4.

Flame heat feedback evaluation

The gaseous energy feedback from the flame to the surface is critical for modeling of the flammability of solid fuels. Due to the difficulties of direct heat flux measurement,

analytical and empirical modeling solutions for its determination have been proposed in the literature. The most common experiment used for evaluating the flame heat flux over a combustible solid is the cone calorimeter.

An early modeling of cone calorimetry was done by Rhodes et al. 1996 [54] for a thermally-thick, one-dimensional PMMA sheet. An approximated value of 37 kW m^{-2} was used for the flame heat flux. This value was computed from an analytical model of convective heat flux from PMMA pool fires [55] and a calculated radiant heat flux assuming a known temperature and emissivity of a PMMA flame [54]. This approach was subsequently applied to other common, commercial polymers such as nylon, polyethylene and polypropylene, with an estimated flame heat flux range of 14-30 kW m^{-2} [56].

An empirical solution for determining the flame heat feedback was proposed by Stoliarov et al. 2009 [48]. For each material, the flame heat flux was computed from inverse modeling, targeting the heat release rate (HRR) data from cone calorimetry and adjusting its value in small increments until the best agreement with experimental data was achieved. The interaction between the flame and the sample surface in the model was characterized by adding an estimated 12–24 kW m^{-2} pure radiative heat flux source term once ignition occurs. The derived flame heat fluxes were then used to predict the HRR at other test conditions. Overall, peak HRR and time to peak HRR were accurately predicted by the simulations, but average HRR was not predicted well for thin samples.

Modeling of the gas-phase flame using CFD simulations of a flame over a black PMMA surface was conducted by Linteris et al. 2005 [57]. Cone calorimeter experiments were made to validate the model. Topography measurements showed that the samples do not burn uniformly over the surface, especially for lower levels of cone irradiation, indicating the non-uniformity in flame heat feedback across the sample. This was also observed in other studies, indicating that heat flux at the center of the sample was primarily radiative and smaller in magnitude than on the sides of the sample, where it was dominantly convective [58, 59].

The dependence of flame heat flux on variables such as position across the sample, sample material, irradiation, burning rate, and the nature of the flame heat flux (radiative or convective) was studied by McCoy et al. 2019 [60]. In cone calorimeter experiments, the flame heat flux was measured in polymer samples cut in squares with 100 mm sides. A center zone and a side zone were defined, and heat fluxes were partitioned into radiative and convective components based on an analysis of the materials' radiative fractions. The sides were assumed wholly convective, with a flame temperature of 2150 K and convective heat coefficient of 20 W m^{-2} K^{-1}. The heat flux at the center was assumed primarily radiative, and a mean value of 9.5 kW m^{-2} was determined along a minor convective heat flux with a coefficient of 3.7 W m^{-2} K^{-1}. The final model was an area-weighted combination of the center and side zone simulations, and both average and peak HHR were well-predicted in the simulations.

1.2.4 Flame retardants

A common approach to enhance the fire safety performance of polymers is the use of flame-retardant additives. They can be added to inexpensive and widely used commercial plastics, such as polyethylene, polypropylene and polystyrene for passing flammability tests, while retaining their physical properties and processability [61]. Flame retardants (FR) can have one or more modes of action [62]:

- **Gas-phase action:** Reaction of removal by catalysis of the reactive OH* and H* radicals, which are released by burning materials and feed the fire.
- **Solid-phase action:** Generation of a char layer on the material surface, which insulates from the heat and prevents contact between oxygen and flammable gases.
- **Heat buffer:** Endothermic degradation reactions that absorb heat in the system.
- **Dispersion:** Release of non-combustible gases, such as water and nitrogen, diluting the combustible gases and oxygen in the system.
- **Pyrolysis:** Promotion of the release of poorly flammable molecules via catalysis.

Intumescent flame retardants (IFR)

In the category of solid-phase action, the intumescent flame retardants (IFR) are studied in this PhD thesis. When heated beyond a critical temperature, an intumescent material begins to swell and then to expand. The result of this process is a foamed, cellular charred surface layer protecting the underlying material from the action of the heat flux of the flame, as illustrated in Fig. 1.11.

Figure 1.11: Intumescent coating formed from intumescent-based polypropylene after ignition. Ammonium polyphosphate is used as an acid source and tris(hydroxyethyl) isocyanurate (THEIC) as char former. Taken from Bourbigot et al. 2019 [63].

The following steps were reported to occur during the intumescence process, with some degree of variability depending of the used components [62]:

1. An inorganic acid is formed between 425 and 490 K, depending on its source and original components.
2. After a slight increase in temperature, the acid esterifies the carbon rich components.
3. The mixture of materials melts prior to or during esterification.
4. The ester decomposes via dehydration, resulting in the formation of an inorganic, carbon based residue.
5. Gases released from degradation products cause the carbonizing material to foam.
6. At the end of the reaction process, solidification occurs in the form of a multicellular foam, as shown in Fig. 1.12.

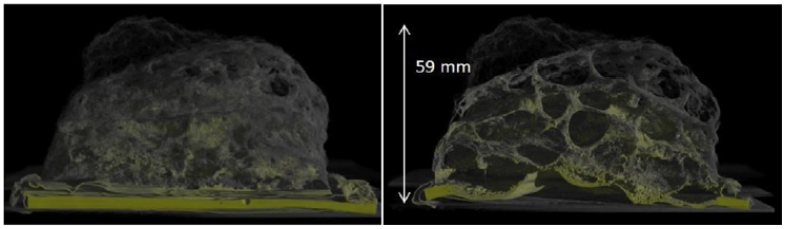

Figure 1.12: X-ray computed tomography pictures of an IFR system composed of 28%APP and 2% nano magnesium oxide in a polyurethane matrix. Left - full view; right - frontal cut through the sample. Taken from Muller et al. 2013 [64].

A comprehensive review of developments regarding intumescent systems for fire protection and flame retardancy was done by Alongi et al. 2015 [65]. It consisted on reviewing the research and development of IFR systems, ranging from the traditional methods employed in the 1970s to the latest developments in the reaction and resistance to fire based on the intumescence concept. First, the traditional studies and patents from the 1970s were reviewed. The pioneering works of Camino and colleagues [66, 67, 68] first identified the principal ingredients of intumescence and their basic chemistry. The parameters that control the fire protection resulting from formation of the expanded carbonaceous char were pointed out, such as heat conductivity (heat transfer), viscosity (expansion), kinetic parameters (dynamic of the degradation), size and cell distribution (structure and morphology) and chemical composition. Finally, novel strategies for development of IFR were implemented. Particularly, the incorporation of acid sources, carbon sources and blowing agents that act in a synergistic manner, following a precise sequence of reactions at the right time and temperature. Newly synthesized molecules were applied for that purpose, as well as polymers with intrinsic charring properties. A comprehensive list of studies of IFR polymeric systems was also presented.

Ammonium polyphosphate/Pentaerythritol (APP/PER)

One of the most widely studied flame retardant systems is ammonium polyphosphate (APP), in which it acts as both an acid source and a blowing agent (see Fig. 1.11). A commonly used charring agent is the polyhydric alcohol pentaerythritol (PER). The combination APP/PER was first chemically and structuraly studied in the works of Camino and colleagues [66, 67, 68] and, since, its effects were further investigated in several aspects such as synergistic effects, different polymer blends and modeling of decomposition. Most APP/PER studies considered polyurethane as a matrix, whereas studies of this IFR in polyethylene, as performed in this thesis remains scarce [65]. A few recent studies involving the development of this IFR system are presented.

Using TGA, the APP/PER system is structurally and chemically characterized by its thermal behavior by Bourbigot et al. 1996 [69]. Moreover, the effect of the addition of zeolite (A4) in the formulation was investigated. It was found that a pure APP/PER mixture presents an enhanced thermal stability over the APP/PER/A4 up to T=500 K, but at higher temperatures, the zeolite leads to the formation of a more stable carbonaceous residue.

The kinetics of the thermal degradation of a microencapsulation of APP/PER at a mass ratio of 3:1 in a melamine-formaldehyde was compared with the conventional APP/PER formulation by Sun et al. 2012 [70]. The microencapsulated form of the IFR system led to an improvement of the flame retardant properties. The improved thermal instability was attributed to the nonflammable gases produced by ignition of the melamine resin, helping the formation of a honeycomb char structure.

The effect of two flame retardant additives, APP and the combination of a nickel carbonate with pentaerythritol phosphate nickel salt (PPNS), on the burning behavior of a polyethylene matrix was investigated by Li et al. 2015 [71]. Compared to the effect of each individual flame retardant additive on flammability tests, a synergistic effect was observed in the form of a stable char layer in the later stages of combustion.

An IFR system of high-density polyethylene, APP and tris (2-hydroxiyethyl) isocyanurate (THEIC) is studied by Khanal et al. 2018 [72]. Flame retardance was measured by limiting oxygen concentration, thermogravimetric analysis, differential scanning calorimetry and cone calorimetry tests. An IFR system with a mass ratio of APP/THEIC of 3:1 was found to greatly reduce flammability of the material.

The fire performance of two IFR was studied by Bourbigot et al. 2019 [63] in a polypropylene (PP) matrix: APP and expendable graphite (EG). APP created a protective coating that worked as a heat barrier from the heat source, whereas EG created an expansion that increased heat dissipation [73]. By modeling kinetic degradation, both IFR systems were shown to increase thermal stability of the PP. Combination of both flame retardant additives was also investigated. It was shown that graphite worms formed by the EG aligned normal to the coating formed by the APP, thus increasing heat conductivity and decreasing fire performance. This effect was also observed and investigated by Bensabath et al. 2021 [74].

Few studies are available on the quantification of the intumescent material properties due to its difficulties in direct measurements. The conductive and radiative heat transfer in the porous medium of a polymeric intumescent char coating was studied

by Kang et al. 2019 [75]. The modeling purpose was to mathematically determine an apparent thermal conductivity of the coating, thus evaluating a material fire resistance performance. An increase in the porosity, pore size and a decrease in the solid conductivity led to enhancements on the thermal insulation of the polymeric porous media. The morphology of carbonized materials resulting from an intumescence process was studied using X-ray computed tomography by Muller et al. 2013 [64]. The IFR system was 30%APP and 28%APP and 2% nano magnesium oxide (MgO) in a polyurethane matrix. The heat conductivity of the systems was measured as a function of temperature in order to correlate structure and properties of the intumescent residues, as shown in Fig. 1.13. Upon heating, the materials softens and produces gases that expand it, and the conductivity decreases. In this stage, the performance of the intumescent coating in terms of thermal insulation was shown to be optimal. After 675 K, the heat conductivity of both formulation increased with the temperature as char expansion was maximum.

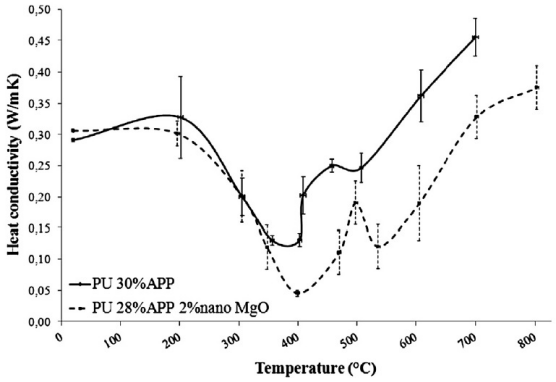

Figure 1.13: Evolution of heat conductivity as a function of temperature for 30%APP and 28%APP and 2% nano magnesium oxide in a polyurethane matrix. Taken from Muller et al. 2013 [64].

Solid-phase modeling of IFR systems

A mathematical model that predicted the temperature distribution along a decomposing polymer-based intumescent coating was proposed by Griffin 2010 [76]. The effect of the material thermal parameters, as well as its endothermic and/or exothermic decomposition and phase-change reactions were investigated, related to the capacity of a material to resist to fire when exposed to a radiant source. Good agreement with experimental results with two types of intumescent coating formulations reinforced previous findings that the expansion of the coating had a major influence on the thermal resistance of these materials. The limitations of a 1D model were also discussed.

The burning behavior of several charring polymers was numerically investigated by Li et al. 2015 [77]. In the case of highly intumescent polymers (such as Kydex and polyetherimide), limitations of the model burning predictions were observed.

The substantial sample swelling led to large uncertainties on heating intensity and atmosphere composition. It was also suggested that a multi-dimensional model might be necessary to better understand the mechanism of swelling and heat transfer in these cases.

A model that predicts the kinetics and thermodynamics of thermal decomposition of an IFR system was proposed by Ding et al. 2016 [78]. The material system analyzed in this study was polylactic acid (PLA), melamine and APP. This methodology was an extension of the previously described strategy for the parameterization of thermal composition parameters of neat materials [50, 79]. The key aspects of pyrolytic behavior in the condensed phase were quantitatively described, including possible interactions between components of the polymer decomposition and the flame retardant additives, using second-order reactions. Microscale combustion calorimetry (MCC) allowed for characterization of the enthalpy of combustion of the released virtual species released by the reaction model. Subsequently, the flame retardancy of this system was modeled from cone calorimetry by Sun et al. 2020 [80]. Through inverse analysis of back surface temperature and sample thickness in an inert 1D gasification experiment, mass and heat transport properties could be parameterized. An adjustment in the gas transfer coefficients of certain condensed phase components were necessary in order to predict mass loss rate profiles of the intumescent system. A two-dimensional study of the solid residue profile was also conducted. With the aforementioned gasification model, the impact of both fire retardants could be quantified and intelligently optimized. It was shown that the blend consisting of 25% APP and 5% MEL led to the greatest flame retardancy with a reduction of average peak heat release rate down to 69%.

The same procedure was applied by Ding et al. 2019 [81] to characterize a different system composed of polyamide 66 reinforced with chopped glass fiber, and red phosphorous as a flame retardant. The model parameters were obtained by inverse modeling of TGA and DSC experiments at a heating rate of 10 K min^{-1}, and the model was validated by showing robustness at predicting thermal decomposition dynamics at other heating rates (5 and 20 K min^{-1}) with the same blends. The model was also shown to predict thermal decomposition using different blends, as an overall validation. Cone calorimeter results were then reproduced in this IFR system [82]. An inert 1D pyrolysis code allowed for determination of heat and mass transport properties via inverse modeling, using the previously obtained kinetic and thermodynamic data. The influence of the 'wick effect', in which the molten polymer blends with glass fiber and is transported to regions of lower concentrations, was also studied and modeled. Using heats of combustion obtained in a MCC, an idealized gasification model was developed, enabling intelligent design of multi-flame retardant systems in polymeric matrices.

1.2.5 Summary of the literature

Author	Summary points
Wichman 1992 [14]	Literature review on the opposing-flow flame spread over a solid surface
De Ris 1969 [16]	Analytical expressions for the flame spread rate over a solid fuel
McAlevy III et al. 1969 [15]	Analytical expressions for the flame spread rate over a solid fuel
Delichatsios 1996 [18]; Delichatsios 2003 [20]	Engineering analytical solution for the flame spread problem, from the creation of two parameters that control the flame spread rate, that can be expressed as a function of the solid and gas properties
Konno et al. 2019 [21]	Description of the heat transfer process in a thermally-thin idealized electrical wire consisting of a metallic core and a polymer coating
Huang et al. 2020 [30]	Literature review on combustion over electric wires
Fujita et al. 2000 [23]	Pioneer study of flame spread over wires in μg. The FSR was systematically larger in μg that in 1g
Nakamura et al. 2008 [24]	Study of the similarity between flame spread over wires in μg and sub-atmospheric pressures in 1g
Thomsen et al. 2019 [25]	Study of the similarity between FSR and flame intensity in μg and sub-atmospheric pressures in 1g
Gagnon et al. 2021 [26]	Study on the effect of pressure on the flame spread mechanism and dripping
Zhao et al. 2017 [27]	Study on the effect of pressure on the flame spread mechanism, flame shape and dripping
Umemura et al. 2002 [31]	Development of a mathematical model to describe the role of the metallic core on flame spread over electric wires
Takahashi et al. 2013 [33]	Study of the unsteady molten insulation volume change
Osorio et al. 2015 [29]	Comparisons for flammability limits of wires between normal 1g and μg
Nagachi et al. 2019 [36]	Study of the effect of flow direction on the mechanism of extinction limit of flame spread over wires
Konno et al. 2020 [39]	Investigations of the effect of the metallic core on the extinction phenomena in electric wires. Measurements of temperature profiles along the wire
Konno et al. 2020 [38]	The effect of the metallic core diameter, μg and external radiant heat fluxes on the wire flammability
Citerne et al. 2016 [8]	Interactions between multiple, parallel wires in concurrent and opposed oxidizer flow

Guibaud et al. 2020 [40]; Guibaud et al. 2020 [41]	Experimental and numerical studies of soot production and radiative heat transfer in burning wires
Guibaud et al. 2020 [42]	Effect of oxygen concentration, pressure and opposing air flow velocity on the flame spread rate

Table 1.1: Summary of the literature review on flame spread over wires in microgravity

Author	Summary points
Henderson et al. 1985 [43]	Development of a simple decomposition model of polymers based on their apparent properties, experimentally determined
Vovelle et al. 1987 [44]	Modelling of the degradation of PMMA when subjected to external radiant fluxes
Stoliarov et al. 2009 [48]	Development of a pyrolysis model that reproduces results from cone calorimetry. Empirical determination of the flame heat feedback energy from inverse modeling
Kim et al. 2015 [49]	Review and evaluation of methods for determining input parameters for pyrolysis modeling
Li et al. 2013 [50]; Li et al. 2014 [51]; Stoliarov et al. 2015 [79]	Development of a strategy to parameter determination from a systematic inverse modeling of a series of gasification experiments, isolating individual pyrolysis processes
Linteris et al. 2012 [52]	Determination of radiative absorption coefficients of engineering polymers for input in pyrolysis modeling
Chaos et al. 2011 [53]	Evaluation of optimization algorithms commonly used for parameter determination
Rhodes et al. 1996 [54]; Iqbal et al. 1994 [55]; Hopkins Jr et al. 1996 [56]	Estimation of the flame heat feedback from a burning surface, with convective and radiative contributions
Linteris et al. 2005 [57]; Kacem et al. 2016 [58]; Boyer 2017 [59]	Gas-phase flame tomography study over a burning polymer surface and evaluation of the flame heat flux in cone calorimetry across the sample
McCoy et al. 2019 [60]	Measurement of the flame heat feedback in square polymer samples in a cone calorimeter. The flame heat was partitioned in a side zone, mainly convective and a center zone, mainly radiative

Table 1.2: Summary of the literature review on characterization of polymers flammability

Author	Summary points
Bourbigot et al. 2007 [62]	Description of the overall intumescence process
Alongi et al. 2015 [65]	Comprehensive review of traditional and recent intumescent flame retardant systems
Camino et al. 1984 [66]; Camino et al. 1984 [67]; Camino et al. 1985 [68]	Description of the mechanistic of decomposition and intumescence of APP/PER
Bourbigot et al. 1996 [69]	Description of the overall intumescence process
Bourbigot et al. 2007 [62]	Structural and chemical characterization of APP/PER decomposition using TGA. Study of the effect of zeolite addition in the mixture
Sun et al. 2012 [70]	Kinetics of degradation of APP/PER in melamine-formaldehyde and in micro-encapsulated form
Li et al. 2015 [71]	Study of the effect of APP and the combination of a nickel carbonate with pentaerythritol phosphate nickel salt (PPNS), on the burning behavior of a polyethylene matrix
Khanal et al. 2018 [72]	Study of an IFR system of high-density polyethylene, APP and THEIC in TGA, DSC and cone calorimetry
Bourbigot et al. 2019 [63]; Bensabath et al. 2021 [73]; Bensabath et al. 2021 [74]	Fire performance evaluation of APP and expandable graphite and their combination on polypropylene
Kang et al. 2019 [75]	Mathematical modeling of the conductive and radiative heat transfer in the porous medium of a polymeric intumescent char coating
Muller et al. 2013 [64]	X-ray computed tomography and thermal conductivity measurements of the carbonized intumescent coating
Griffin 2010 [76]	Mathematical model of the temperature distribution along a decomposing polymer-based intumescent coating
Li et al. 2015 [77]	Pyrolysis modeling of charring polymers using Thermakin
Ding et al. 2016 [78]	Development of a semi-global reaction mechanism of an IFR consisting of polylactic acid, melamine and APP, and determination of its kinetics and thermodynamic parameters
Sun et al. 2020 [80]	Cone calorimetry in a near-one dimensional modeling of the materials studied by Ding et al. 2016 [78]

Ding et al. 2019 [81]	Semi-global mechanism of an IFR consisting of polyamide 66 reinforced with chopped glass fiber, and red phosphorous, and determination of its kinetics and thermodynamic parameters
Ding et al. 2019 [82]	Cone calorimetry modeling of the materials studied by Ding et al. 2019 [81], and modeling of mass transport inside the sample

Table 1.3: Summary of the literature review on flame retardants

2 An Engineering model for creeping flame spread over idealized wires in microgravity

Sommaire

Fire hazards in a confined environment such as a spacecraft are a threat to equipment integrity and even the safety of the astronauts. The main potential source of a fire in this situation is attributed to electrical malfunction. The insulation and jacket layers of wire and cable are made of plastic materials, which may release pyrolysis gases when heated by external sources or short-circuiting. This flammable gas can mix with ambient oxidizer to be ignited, resulting in subsequent sustained combustion process and flame spread over the wire. This common scenario of flame spread over polymer-coated electrical wires has motivated extensive researches in both normal gravity [24, 83, 84, 30] and microgravity [23, 31, 33, 8, 42, 37].

Simplifying the in-flight configuration to an academic problem, the analysis of steady state opposed flow flame spread over a vertical wire is key to understanding the flammability of solid fuels [14]. Flame spread over solid surfaces results from the heating process of the material ahead of the pyrolysis front. Heat transfers of multiple natures raise the unburnt solid from the ambient temperature up to the pyrolysis temperature at which the material starts to release gaseous fuel that is ignited by the flame, ensuring the spreading process [15]. The flame spread process can be viewed then as a series of piloted ignitions where the flame acts as both heating source and pilot [85].

Flame spread models and correlations have been proposed for the case of opposed

steady state flame spread, denoted also as creeping flame spread [85]. Most notably, a correlation based on the heat balance ahead of the pyrolysis front in both thermally-thin and thick configurations is the deRis flame-spread model, presented in the literature review of this manuscript in section 1.2.1 [16]. In this approach, the heat transfer from the flame to the solid was obtained by solving the laminar boundary layer equation along with the infinite fast gas-phase chemistry and Oseen approximations. The flame spread rate (FSR) could be then assessed and characterized based on measurable material and gas properties. It was nevertheless observed that this model largely overestimates the flame heat transfer and the corresponding FSR, owing to the assumption of infinitely fast kinetics, which is not satisfied at the flame leading edge. This assumption implies that the flame is 'attached' to the solid surface, as previously shown in Fig. 1.4. In reality, the relatively cold solid surface acts in this region as a heat sink that produces local flame extinction, resulting in a complex flame attachment process [14].

In order to circumvent these difficulties and to provide an engineering analytical flame spread model, Delichatsios and co-workers reduced the flame heat transfer process to two properties, measurable from material and ambient gas properties, that characterize the creeping flame spread process: the convective heat flux per unit length, $\dot{E}'_{gs,pr}$, from the flame to material near the pyrolysis front and the gaseous thermal length, L_g, generated by the opposed oxidizer flow [18]. In addition, they provide experimental methodology and methods for their determination. A heat balance equation and its corresponding methodology was first proposed for a flat burning surface [18], before being extended to cylindrical samples [19]. As compared to flat geometry, the cylindrical curvature was found to modify the heat balance by enhancing gas-to-surface heat transfer and by reducing the heated layer depth in the solid. This heat balance was also developed for a flat material undergoing a melting process [20].

The presence of the metallic core inside the flammable polymer coating is known to modify the heat transfer pattern, from the ignition, spread, extinction to the phase-change processes of the polymer insulation and emission of combustion products [32, 30]. It was shown that increasing the thermal conductivity of the core results in an increased FSR, but simultaneously increases the local extinction behavior due to increased heat losses in the the unburned zone [38]. This process is impacted however by several parameters, as the role of the metallic core as a heat sink or heat source is shown to be controlled by the wire material properties, geometry and ambient conditions, most of which aren't well understood [30].

A detailed description of the heat transfer process in the case of a thermally-thin idealized electrical wire consisting of a metallic core and a LDPE coating has been provided by Konno and colleagues [21]. Figure 2.1 summarizes this heat transfer process. The heat transfer to the virgin polymer upstream to the pyrolysis front is driven by both the flame heat flux and the heat transfer from the metallic core to the virgin polymer. As observed in the experiments of Guibaud and co-workers [40], the polymer is entirely consumed by the degradation process, leading to a diffusion flame that falls down to the bare wire at the trailing edge. This induces a substantial heat flux

from the flame to the bare wire, which is in turn conducted through the metallic core towards the pyrolysis zone, contributing in addition to the flame heat flux to pyrolyse the solid. A part of this flux is then transferred though the metallic core ahead of the pyrolysis zone.

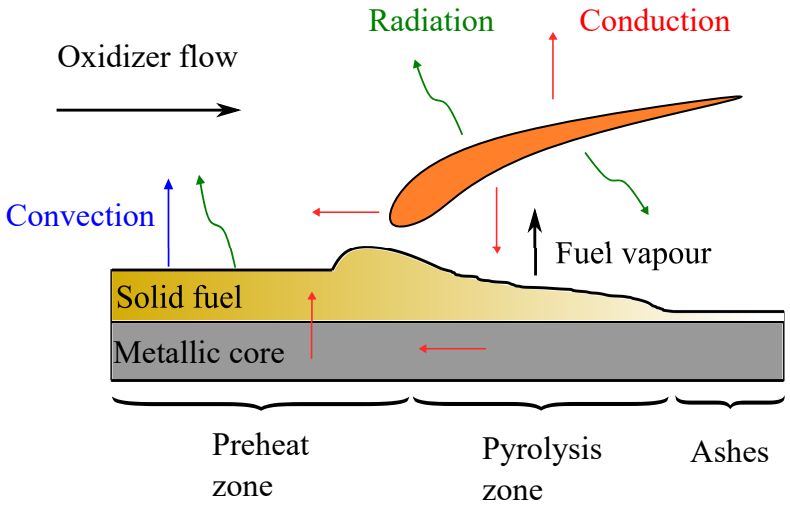

Figure 2.1: 2D scheme of opposed flow flame spread over polymer-insulated electric wire.

The objective of this chapter is to predict creeping flame spread over idealized polymer coated metallic wires in microgravity. It will be shown how this complex heat transfer behaviour can be simplified if the pyrolysis can be treated as phase-change as assumed in the aforementioned heat balance flame spread models [16, 18, 21]. An engineering heat balance flame spread model and an experimental procedure to determine the material properties characterizing the creeping flame spread over thin electrical wires are developed. The experiments made by Guibaud and co-workers on Nicr/LDPE electrical wires will be considered to determine these parameters and validate the model [40]. These experiments and assumptions for characterizing steady flame spread are described in Section 2.1. The flame spread model, governing equations and considered material and gas-phase properties will be presented in Section 2.2. The results will be discussed in Section 2.3. The calibration of the model parameters is presented and validated against experimental data. Then, a study of the heat mechanisms in the wire is discussed. Finally, the last section will be devoted to the conclusions and perspectives of this first step towards a fully predictive flame spread model.

2.1 Experimental methodology

The experimental procedure used to obtain the flame spread rate is briefly described in this section. Experiments in microgravity are conducted on the Detection of Igni-

tion And Mitigation Onboard for Non-Damaged Spacecrafts (DIAMONDS) rig, which is presented in the introduction of this thesis and extensively described in a previous work [8]. DIAMONDS were installed aboard the Novespace A310 ZeroG airplane, a facility that specifically operates parabolic flights. Every parabola provides a 22 s long sequence of microgravity with an accuracy level of $5{\cdot}10^{-2}$ g_0 ($g_0 = 9.81$ m/s^2). The experimental setup consists of a cylindrical combustion chamber with an inner diameter of 190 mm, where a laminar O_2/N_2 oxidizer flow can be established with a direction from the bottom to the top of the chamber. The flow conditions can be controlled with the oxygen content in volume fraction ranging from 0 to 21%, the pressure from 50.7 to 121.6 kPa and the flow velocity from 0 to 300mm/s. Cylindrical wires of length 150 mm, composed of a NiCr core coated by LDPE insulation, were placed along the central axis of the chamber and parallel to the flow direction. LDPE has been used as coating of laboratory wires as an international target configuration to investigate flammability properties of electrical cables in both normal and microgravity conditions [23, 86, 30]. In these experiments, three core-to-wire radius ratios, R_c/R_s were tested: (i) 0.25/0.4 (Type#1), (ii) 0.25/0.55 (Type#2) and (iii) 0.25/0.65 (Type#3), as summarized in Table 2.1. The core radius was kept unchanged and the LDPE thickness, δ_s, was varied. The cross sections area ratio, a_c/a_s, of Type#1 is about 2 and 2.63 times larger than those of Type#2 and Type#3, respectively. The samples were ignited using a hot Kanthal wire located at its upper end to initiate an opposed-flow flame spread.

Type	R_c (mm)	R_s (mm)	δ_s (mm)	a_c/a_s
I	0.25	0.40	0.15	0.391
II	0.25	0.55	0.30	0.206
III	0.25	0.65	0.40	0.148

Table 2.1: Configurations of NiCr core and LDPE insulations

All experiments were captured using a JAI AT-140CL digital tri-CCD camera, equipped with a telecentric lens to restrict the light collection to beams parallel to the optical axis. A controlled uniform LED backlight located sample is set on and off alternatively during the images acquisition in order to track the morphology of flame and LDPE droplet. Images are captured with a frame rate of 39.06fps over a 512x1396 pixels^2 CCD array in the red, green and blue spectral bans with a resolution of 72.6 μm ,which can provide an entire view during the flame spread. FSR is determined by tracking the flame front using image without backlighting processing once a steady flame spread is reached and a detailed description can be found in Ref. [87]. According to the images with backlighting, the spreading over LDPE is characterized by the formation of a molten droplet whose, for the conditions investigated in the present study, the volume increases first before reaching a steady value. The flame is assumed to spread at a steady rate once the dimensions of the molten insulation droplet, the visible flame length, and the rate of the flame front displacement reach a steady state value. These three steady spread criteria are illustrated in Fig. 2.3.

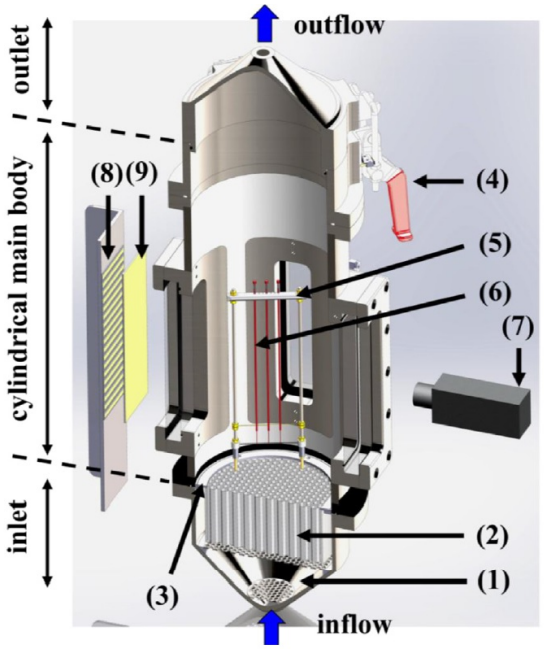

Figure 2.2: Schematic of the combustion chamber designed for the parabolic flights. (1) Conical part filled with glass beads; (2) stainless steel honeycomb; (3) stainless steel ring; (4) latch clamp for top end locking; (5) sample holer; (6) polyethylene coated wires; (7) camera; (8) set of LEDs; (9) diffusive screen. Reproduced from Citerne et al. 2016 [8].

The captured images are shown in Fig. 2.4. These experiments are conducted in four parabolic flight experiments, with oxygen content ranging from 18 to 21 %. The snapshots are taken 15-20 s after ignition and at the beginning of the microgravity sequence, with a backlight illumination. Fluctuations of visual flame length, luminosity and smoke emission are observed when varying the oxygen concentration. A 1 mm scale is shown in the upper left corner. The measured flame spread rate is also observed to have a significant impact with the oxygen concentration, which will be discussed in the results section.

2.2 Flame spread model

2.2.1 Model assumptions

The model considers a flame spreading at a steady rate over a thin electrical wire composed by a metal core of radius R_c and a polymer coating of radius R_s, as shown in Fig. 2.6. During steady-spread rate, the wire can be decomposed into four regions as illustrated in Fig. 2.6. The region directly ahead of the pyrolysis front is referred to as the preheat zone and involves the heat transfer between the flame and the LDPE. This region is proceeded by the unburnt zone where the heating process is manly driven

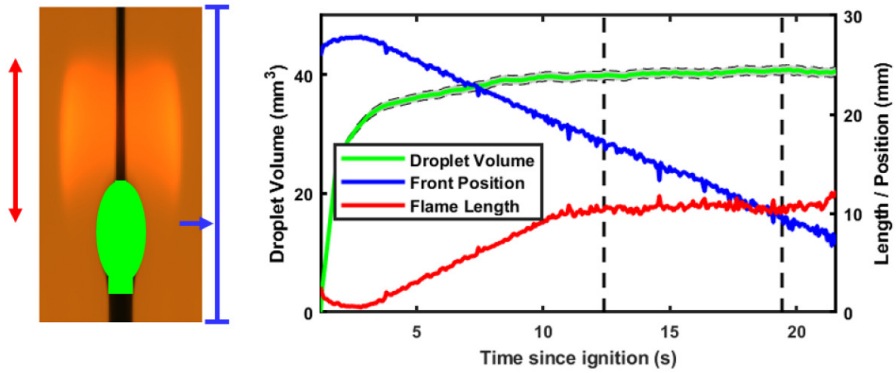

Figure 2.3: Steady state is assessed in parabolic flight by tracking the evolution of the flame front position (blue), flame length (red), and molten droplet volume (green). Reproduced from Guibaud et al. 2020 [41].

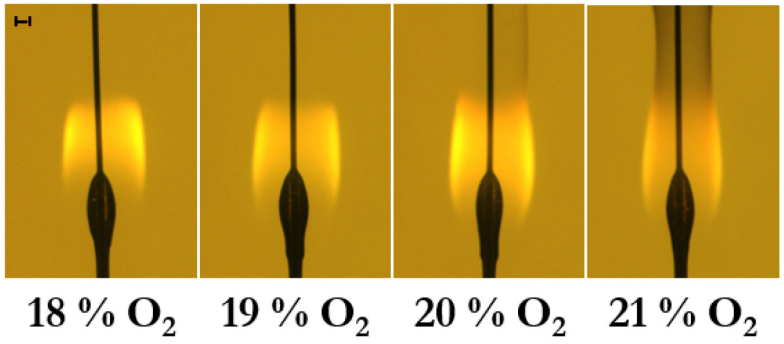

Figure 2.4: Opposed-flow spread of a flame in microgravity over a polyethyene-coated NiCr wire. Flow velocity and ambient pressure pressure are fixed at 150 mm/s and 101 kPa, respectively. Reproduced from the PhD thesis of Augustin Guibaud [88].

by conduction through the metallic core. The pyrolysis zone is located downstream the pyrolysis front followed by a bare metallic core as the polymer is completely burnt. The following assumptions are introduced:

i The polymer melting and the pyrolysis processes behave as phase changes occurring at temperatures $T_s = T_m$ and $T_s = T_p$, respectively.

ii The polymer can expand or contract in the direction r.

iii The flame front corresponds to the location, z_p, where the surface temperature of the polymer reaches T_p.

iv In the pyrolyzing region, the temperature of the polymer layer is maintained constant to $T = T_p$. .

v In the pyrolyzing region, the metal core and the polymer layer become rapidly in thermal equilibrium. This assumption implies that the heat flux, $E_{(cc,u)}$, conducted from the bare metal core toward the pyrolyzing region is completely transferred to the pyrolyzing polymer. Therefore, it does not affect the heat balance in the preheat region, and, in turn, the flame spread. The validity of this assumption has been assessed by using the CFD model, described in detail by [40]. During the simulation, it is assumed that the pyrolyzing LDPE is at T_p, consistent with the assumption iv. The results reported in Fig. 2.5 show the evolution along the wire axis of the temperatures inside the metal core and LPDE for a simulation considering a LPDE/NiCr of Type #2 (see Table 2.1), an oxidizer composed of 21% of O_2 and 79% of N_2 flowing at a velocity of 150 mm/s and a pressure of 101 kPa. The same behavior is observed for the other wire geometries and ambient conditions. Figure 2.5 shows that the NiCr temperature reaches a peak at the location where the flame falls to the bare metal core. This temperature decreases downstream and upstream the peak. In the pyrolyzing region, it reaches rapidly the pyrolysis temperature, suggesting that the present assumption is satisfied provided that assumption iv holds.

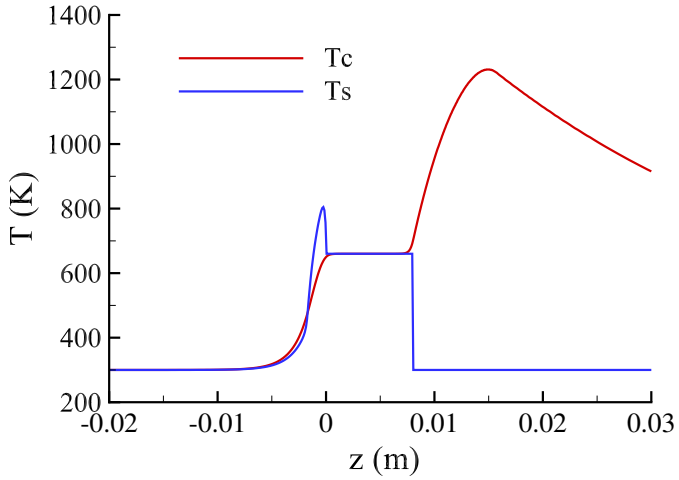

Figure 2.5: Evolution of LDPE and NiCr temperatures along the wire axis.

vi In the preheat zone, the radiative flux from the flame is balanced by the heat flux re-radiated by the solid surface. This assumption is sustained by numerical simulations [40].

vii The opposed flow is modelled as an Oseen flow with a vertically uniform velocity, u_∞, parallel to the wire axis.

viii The combustion kinetics is assumed to be infinitely fast with $\mathrm{F}(kg) + s\ \mathrm{O}_2 \rightarrow (1+s)\mathrm{Pr}$.

ix The cylindrical curvature enhances the convective heat transfer from the flame to the solid as compared to a flat slab and a corrective factor is introduced to account for this enhancement [19]. The convective heat flux transferred from the flame to the polymer in the preheat region, $E_{(gs,pr)}$, can be estimated by using assumptions vi to viii [[18], [19]]:

$$E_{(gs,pr)} = 2\pi R_s \dot{q}''_{(fl,c)} L_g = 2\pi R_s E'_{(gs,pr)}. \tag{2.1}$$

In Eq. 2.1, L_g represents a gas-phase thermal diffusion length given by:

$$L_g = \frac{D_g}{u_\infty} = \frac{k_g}{\rho_g c_g u_\infty}, \tag{2.2}$$

and $\dot{q}''_{(fl,c)}$ is the heat flux per unit area transferred from the flame to the solid. The diffusivity D is obtained from the conductivity (k_g), density (ρ_g) and heat capacity (c_g). The subscript g denotes gas properties. $E'_{(gs,pr)} L_g$ is expressed as:

$$E'_{(gs,pr)} = \underbrace{\frac{\sqrt{\pi}\frac{L_g}{R_s}}{\ln(1+\sqrt{\pi}L_g/R_s)}}_{c} \times \underbrace{k_g \frac{[B - r_f]L_{vap}}{c_g}}_{E'_{(gs,pr,flat)}}. \tag{2.3}$$

$B = [Y_{(O2,\infty)}\Delta h_c/s - c_g(T_p - T_\infty)]/L_{vap}$ is the mass transfer number and $r_f = Y_{(O2,\infty)}/s$ is the mass fuel-to-air ratio. $E'_{(gs,pr)}$ is composed of two contributions: the heat flux estimated for a flat slab, $E'_{(gs,pr,flat)}$, and a corrective factor for a cylindrical geometry. As discussed in the literature [18], the estimation of $E'_{(gs,pr,flat)}$ from the infinitely fast kinetics assumption leads to an overestimation of the heat flux from the flame to the unpyrolyzed polymer. For a given oxidizer composition, this property will be estimated from experiments for the Type#2 wire under a pressure of 101 kPa and an oxidizer velocity of 150 mm/s and will be applied to other wire and ambient conditions. The underlying assumption is:

x $E'_{(gs,pr,flat)}$ does not depend on the oxidizer flow rate, pressure, and wire geometry whose effects are captured through C and L_g.

2.2.2 Governing equations

Based on the aforementioned assumptions, the axi-symmetric heat transfer equations and the corresponding boundary conditions for the LDPE coating and the

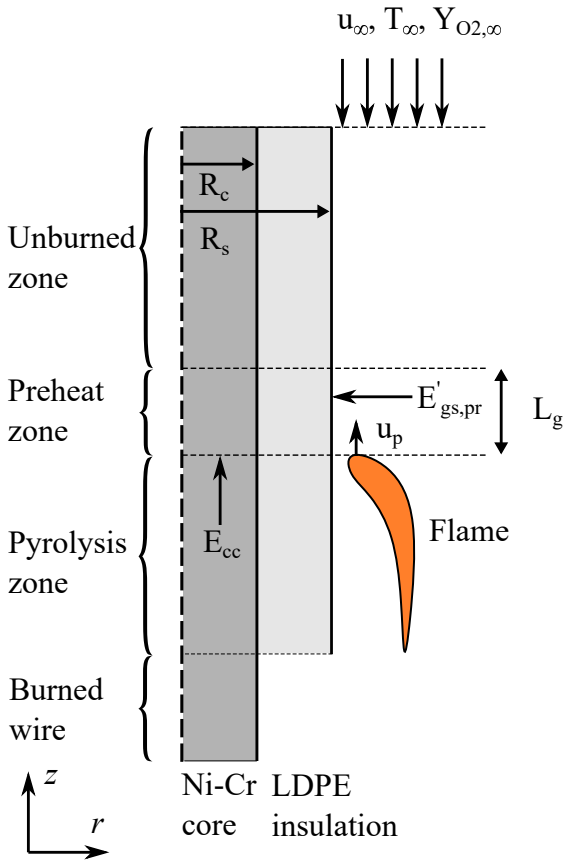

Figure 2.6: Scheme of the engineering flame spread model (not in scale). The distinction between the preheat and unburned zones is reproduced from the works of Konno and co-workers [21].

NiCr core are given below. The assumption iii defines the pyrolysis front as $z_p(t) = \max_z \left(z|_{T_{s(R_s,z,t)=T_p}} \right)$ and the flame spread rate as:

$$u_p = \frac{dz_p(t)}{dt}. \tag{2.4}$$

The assumption v allows to simplify the problem by ignoring the heat flux transferred from the bare NiCr to the preheat zone and by reducing the computational domain to the pyrolysing zone, located for $z_p(t) - L_p \leq z \leq z_p(t)$, and the zone located ahead of the pyrolysis zone, $z > z_p(t)$, including the preheat zone and the unburned zone (see Fig. 2.6). The pyrolysis length, L_p is assumed to be of 10 mm in accordance with experimental observations [41].

- For the LDPE: $R_c \leq r \leq R_s$
  - For $z \leq z_p(t)$:

$$T_s(r,z,t) = T_p \tag{2.5a}$$

- For $z > z_p(t)$:

$$\frac{\partial \rho_s h_s}{\partial t} = \frac{1}{r}\frac{\partial}{\partial r}\left(r k_s \frac{\partial T_s}{\partial r}\right) + \frac{\partial}{\partial z}\left(k_s \frac{\partial T_s}{\partial z}\right) + \frac{1}{r}\frac{\partial}{\partial r}\left[\left(\int_{R_c}^{r} \frac{1}{\rho_s}\frac{\partial \rho_s}{\partial t} r\, dr\right)\rho_s h_s\right] \tag{2.5b}$$

for $T_s < T_m$ and $T_s > T_m$

$$0 = \frac{1}{r}\frac{\partial}{\partial r}\left(r k_s \frac{\partial T_s}{\partial r}\right) + \frac{\partial}{\partial z}\left(k_s \frac{\partial T_s}{\partial z}\right) - \dot{m}'''_m L_m \tag{2.5c}$$

for $T_s = T_m$

where $h_s = \int_0^{T_s} c_s dT$.

The third term in the right-hand side of Eq. 2.5b represents the heat transfer associated with contraction or expansion of the material object. Equation 2.5c describes the melting process.

The following boundary conditions are applied:

$$k_s \frac{\partial T_s}{\partial r} = \dot{q}''_{fl,c} \tag{2.6a}$$

For $r = R_s$ and $z_p \le z \le z_p + L_g$;

$$k_s \frac{\partial T_s}{\partial r} = h\,(T_\infty - T_s) \tag{2.6b}$$

For $r = R_s$ and $z \ge z_p + L_g$;

$$k_s \frac{\partial T_s}{\partial r} = k_c \frac{\partial T_c}{\partial r} \tag{2.6c}$$

For $r = R_c$ and $\forall z$;

$$\frac{\partial T_s}{\partial z} = 0 \tag{2.6d}$$

For $z \to \infty$;

$$T_s = T_p \tag{2.6e}$$

For $z < z_p - L_p$.

The convective coefficient h is computed as $h = k_g Nu/2R_s$, with $Nu = 0.32 + 0.155 Re^{0.5}$ [89]. $Re = \rho_g u_\infty R_s/\mu_g$ is the Reynolds number with μ_g the kinematic viscosity.

The following initial conditions are also considered:

$$T_s(r,z,t=0) = T_p \tag{2.7a}$$

For $z \leq z_p(t=0)$;

$$T_s(r,z,t=0) = T_\infty \tag{2.7b}$$

For $z > z_p(t=0)$;

- For the NiCr: $0 \leq r \leq R_c$

$$\rho_c c_c \frac{\partial T_c}{\partial t} = \frac{1}{r}\frac{\partial}{\partial r}\left(r k_c \frac{\partial T_c}{\partial r}\right) + \frac{\partial}{\partial z}\left(k_c \frac{\partial T_c}{\partial z}\right) \tag{2.8}$$

The following boundary conditions are applied:

$$k_s \frac{\partial T_s}{\partial r} = k_c \frac{\partial T_c}{\partial r} \tag{2.9a}$$

For $r = R_c$ and $\forall z$;

$$\frac{\partial T_c}{\partial z} = 0 \tag{2.9b}$$

For $z \to \infty$;

$$\frac{\partial T_c}{\partial z} = 0 \tag{2.9c}$$

For $z = z_p - L_p$ and $\forall r$;

The initial condition is also applied:

$$T_c(r,z,t=0) = T_\infty. \tag{2.10}$$

The heat transfer equations for the polymer and the metal core were solved in a coupled manner by using the finite volume method [90], a first-order backward Euler scheme for time integration and a second-order centered scheme for diffusion terms. The heat conductivity at the interface between LDPE and NiCr was computed with the harmonic mean to handle the large differences in conductivity between NiCr and LDPE [90].

A steady state flame front propagation was achieved approximately 1 s after the beginning of the simulations for all the wire geometries and ambient conditions, and an interval of $\Delta t = 1$ s between $t = 2$ and $t = 3$ s was used to capture the average spread rate from Eq. 2.4. A time step $\Delta t = 5.0 \times 10^{-5}$ s is used in all configurations.

Multiplying or dividing this value by a factor of 10 was found to provide minor changes on the results. The spatial discretization is uniform, with a cell sizing of $\Delta z = 0.03$ mm and $\Delta r = 0.04$ mm. Multiplying or dividing these values by a factor of 2 was found to provide minor changes on the results.

2.2.3 Material and gas phase properties

The heat capacity, the melting temperature and the heat of melting were obtained from differential scanning calorimetry. The evolution of the density of the LDPE with temperature was taken from literature [91] and it has been checked that the literature values at room temperature are equal to those measured in our experiments. The thermal conductivity of LPDE was measured using the transient line source method. These data as well as the density, heat capacity and conductivity of the NiCr are given in Table 2.2. The gas-phase density, heat capacity and conductivity are evaluated by assuming that the gas is air and by using a temperature evaluated as the average between the adiabatic flame temperature of ethylene in the investigated conditions and the ambient temperature. The LDPE pyrolysis temperature has been estimated in the literature [21] and is consistent with the value obtained from the TGA experiments in this work, shown in Chapter 4.

Property	LDPE	NiCr
Density (kg/m^3)	$\rho_s = 948.2$ for $T_\infty < T_s < T_m$ $\rho_s = 948.2 - 0.94(T_s - T_\infty)$ for $T_m < T_s < T_p$	$\rho_c = 8670$
Heat capacity (J/kg/K)	$c_s = 0.2T^2 - 105.7T + 15773$ for $T_\infty < T_s < T_m$ $c_s = 3.4T + 1228.3$ for $T_m < T_s < T_p$	$c_c = 440$
Thermal conductivity (W/m/K)	$k_v = 0.38$ $k_m = 0.45$	$k_c = 17.4$
Heat of melting (J/kg)	$L_m = 101000$	—
Melting temperature (K)	$T_m = 384$	—
Pyrolysis temperature (K)	$T_p = 690$ [39]	—

Table 2.2: Thermal properties of the LDPE and Nickel-Chrome

2.3 Results and discussions

2.3.1 Calibration of the model parameters

As previously discussed in the model assumption ix, the infinitely fast kinetics assumption led to a systematic overestimation of the heat flux transferred from the flame to the unpyrolyzed polymer [18]. A calibration procedure is performed to estimate the model parameters L_g and $E'_{gs,pr,flat}$. L_g is determined from its definition (Eq. 2.2) and $E'_{gs,pr,flat}$ is calibrated by assuming that the geometry effects are modelled through the geometric correction C and the effects of the oxidizer flow rate and ambient pressure are captured solely through L_g. A consequence is that $E'_{gs,pr,flat}$ is expected to depend only on the oxygen concentration in the oxidizer, X_{O2}.

The calibration procedure consists in fitting the experimental spread rate for the Type#2 wire, a pressure of 101 kPa and an inflow velocity of 150 mm/s. The fitted values are reported in Table 2.3. As expected, $E'_{gs,pr,flat}$ increases with X_{O2}. It can be also observed that the fitted values represent 30% of the theoretical value given by Eq. 2.3 whatever X_{O2}. The quality of the fit is demonstrated in Fig. 2.7.

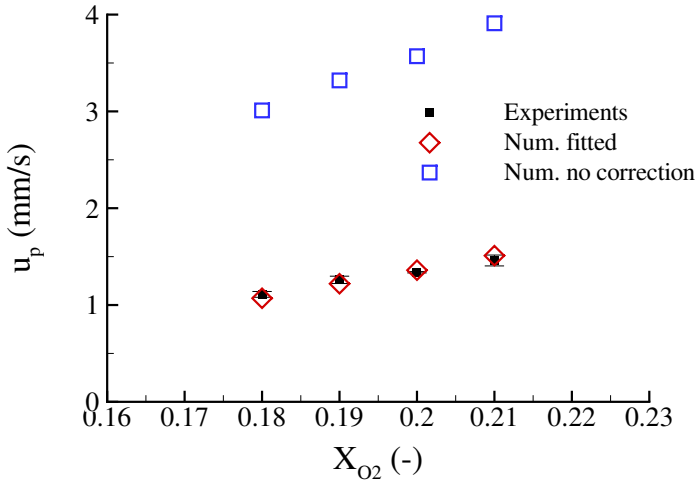

Figure 2.7: Spread rate as a function of X_{O2} for the Type#2 wire, an oxidizer velocity of 150 mm/s and a pressure of 101 kPa. The blue symbols represent the spread rate computed by using Eq. 2.3 whereas the red symbols represent that computed with the fitted $E'_{gs,pr,flat}$.

2.3.2 Flame spread rate

The model along with the calibrated values of $E'_{gs,pr,flat}$ is applied to the other wire geometries and ambient pressures. Figure 2.8 shows the predicted FSR as a function

X_{O2}		0.18	0.19	0.20	0.21
$\left[E'_{(gs,pr,flat)}\right]_{Calibrated}$	(W/m)	17.66	20.14	22.45	25.12
$\frac{\left[E'_{(gs,pr,flat)}\right]_{Calibrated}}{\left[E'_{(gs,pr,flat)}\right]_{Real}}$		0.30	0.30	0.30	0.30

Table 2.3: Values of $E'_{(gs,pr,flat)}$ for the different values of X_{O2}.

of X_{O2} for the Type#1, Type#2 and Type#3 wires. As expected from experimental observations in microgravity for electrical wires [21, 92], the FSR increases with X_{O2} for all the cases owing to an increase in flame temperature, which results in an increase of the flame heat flux transferred to the solid surface. This behavior is well captured by the model.

The effect of wire geometry on the FSR is also well reproduced by the model. For a given X_{O2}, decreasing the wire diameter leads to an increase in the flame heat flux and, in turn, an increase in the FSR. This behavior was also observed in experiments involving black LDPE-coated copper wires [39].

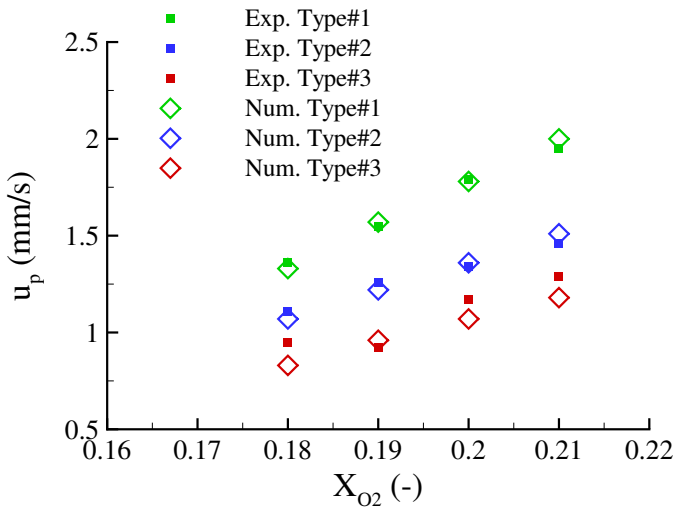

Figure 2.8: Spread rate as a function of X_{O2} for different wire geometries. The oxidizer velocity and the pressure are 150 mm/s and 101 kPa, respectively.

The evolution of the FSR with X_{O2} is displayed for the Type#2 wire for different pressures in Fig. 2.9. For a given oxygen concentration, the FSR slightly decreases while increasing the pressure due to an enhancement in the gas-phase density, ρ_g and, in turn, a reduction in L_g. This behaviour is well captured by the model. The good agreement between the model and the experiments for the different wire geometry

and pressures supports the assumption x.

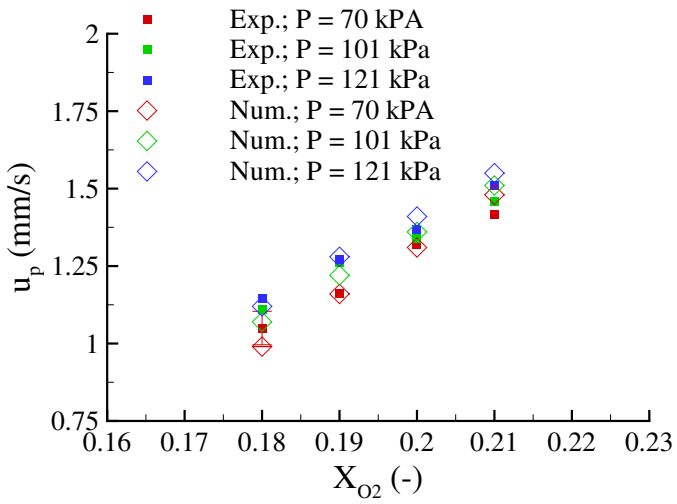

Figure 2.9: Spread rate as a function of X_{O2} for different pressures. The oxidizer velocity is 150 mm/s and the Type#2 wire is considered.

2.3.3 Heat transfer analysis

Contours of temperature at steady spread rate for two LDPE thicknesses (Type#1 and Type#2 wires) are depicted in Fig. 2.10. In this figure, the flame propagates from the bottom toward the top and the two heat fluxes as well as the preheat length, L_g, are indicated. The pyrolysis front is located at $z = 0$, and the vertical line shows the separation between the NiCr and LDPE.

The following conclusions may be drawn from analysis of Fig. 2.10:

1. The temperature gradients in the radial direction r observed in the LDPE coating in preheat as well as the unburned zones clearly suggest that the thermally-thin assumption, widely used in previous studies, is not valid (see Refs. [32, 21, 39] for example).

2. In the preheat zone, the surface temperature of LDPE is larger than that of the metallic core. This behavior is observed for all the investigated conditions. This suggests that the heat transfer from the flame dominates in this region.

3. The metallic core has a significant impact on the temperature field, and, therefore, on the FSR. In order to quantify this effect, simulations have been run by assuming that the core is also LDPE with a conductivity significantly lower than NiCr. Figure 2.11(b) shows the temperature distribution at steady state in this case for the Type #1 wire and a comparison with the temperature distribution

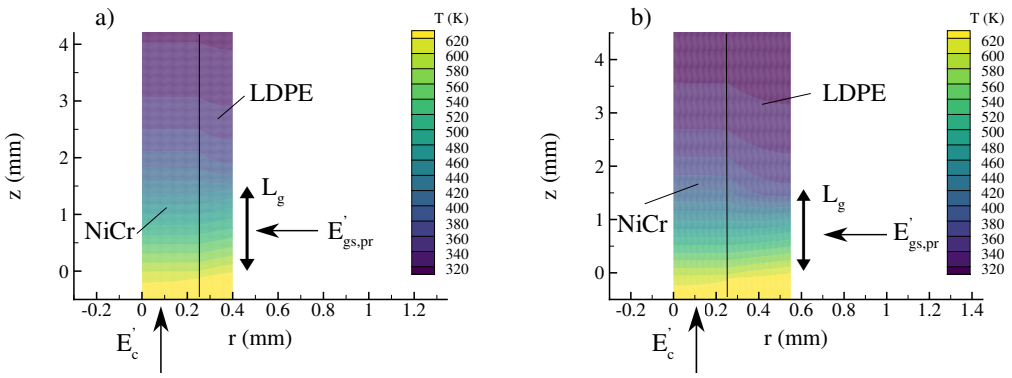

Figure 2.10: Temperature fields in the wire at steady state for (a) Type#1 and (b) Type#2. In both cases, the oxygen concentration and the pressure are 19 % and 101 kPa, respectively. The axis are not in the same scale.

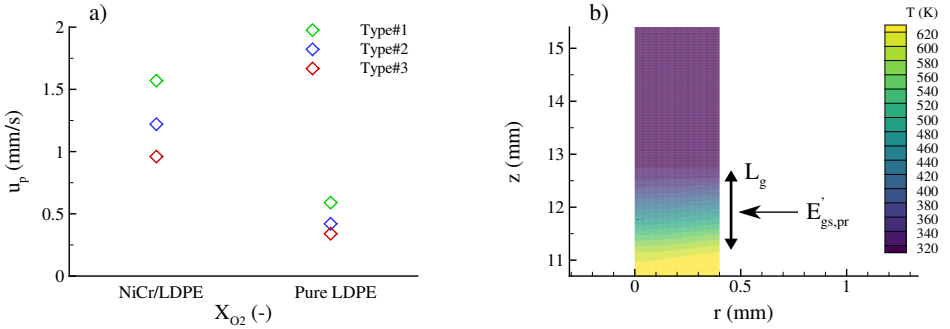

Figure 2.11: (a) Evaluation of the FSR for NiCr/LDPE and pure LDPE wires. (b) Temperature field of Type #1 pure LDPE wire hypothesis. The oxygen concentration and the pressure are 19 % and 101 kPa, respectively.

for the NiCr Type #1 wire in Fig. 2.10(a) illustrates clearly the role of metallic core. When pure LDPE is considered, the heating beyond the preheat zone ($z > L_g$) is negligible and the FSRs are substantially lower for all wire geometries, as shown in Fig. 2.11(a). This behavior agrees with previous experimental observations [30].

4. In the preheat zone, particularly at the vicinity of the flame front, temperature gradients observed in Fig. 2.10 show that heat is transferred from the LDPE to the NiCr, i.e., the core acts as a heat sink for both depicted wire geometries. The heat balance in the preheat zone governs the flame extinction process, and this behavior could suggest that the metallic core has a role in this phenomena [39]. An opposite behavior is observed in the unburned zone with the heat being transferred from the metallic core to the LDPE. The metallic core acts then as a heat source in this region, heating the LDPE before the preheat zone. A

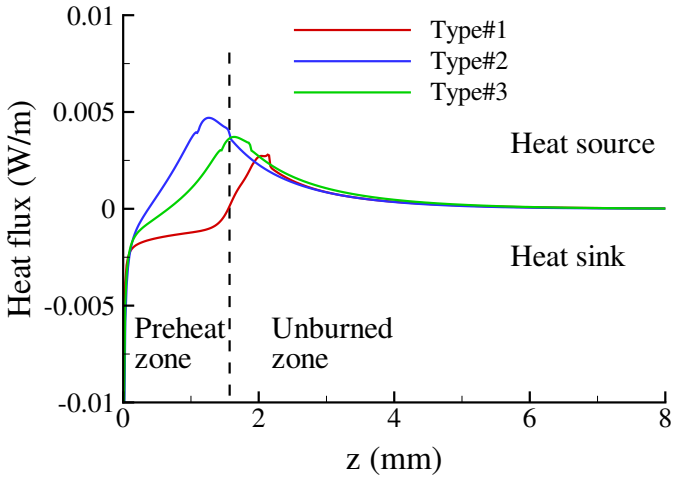

Figure 2.12: Conductive heat flux between the NiCr core and the LDPE coating, in W/m, in the preheat and unburned zones, for three wire geometries, along the wire length. The oxygen concentration and the pressure are 19 % and 101 kPa, respectively. Positive (negative) heat flux values denote heat transfer from the NiCr (LDPE) to the LDPE (NiCr), i.e., the core acts as a heat source (sink).

quantitative analysis of the heat transfer between the NiCr and LDPE along the wire length is shown in Fig. 2.12. The pyrolysis front is at $z = 0$ and both preheat ($0 < z < L_g$) and unburned ($z > L_g$) zones are depicted. This figure illustrates the change of heat transfer direction between the preheat and the unburned zones. It also highlights also the role of the LDPE thickness in the heat transfer between the LPDE and NiCr in the preheat zone. It appears that the length over which the NiCr core acts as a sink increases with decreasing the LDPE thickness. For the thinner wire (Type #1), it acts as a heat sink over the entire preheat zone while, for the other wires, the length of the heat sink zone reduces. The role of the metallic core on the preheating process is further illustrated in Fig. 2.13 which shows the elevation of LDPE surface temperature ahead of the flame front. For the thinner wire (Type #1), the surface temperature at the transition between the unburned and preheat zone exceeds the LDPE melting temperature.

2.4 Conclusions

An engineering solution for a creeping flame spread model over idealized electrical wires composed of a NiCr metallic core and a LDPE coating in microgravity has been proposed and validated against experimental data obtained in parabolic flights. It has been shown that the heat transfer problem can be simplified by ignoring the heat flux from the bare metallic core and solving the coupled heat transfer equations for

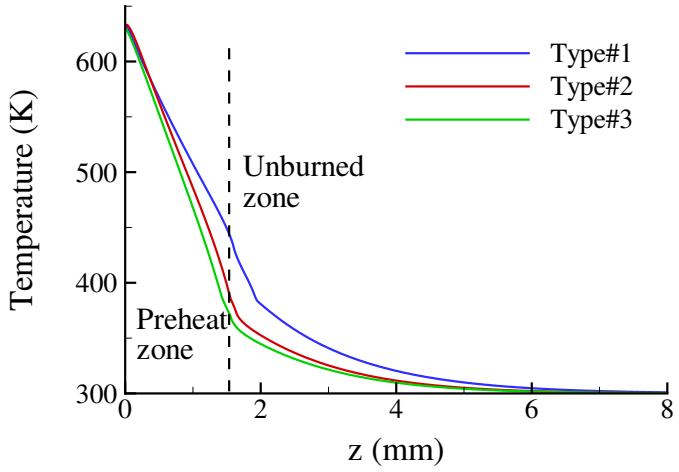

Figure 2.13: LDPE surface temperature, in K, in the preheat and unburned zones.

LDPE and NiCr in the pyrolysis zone and ahead of the pyrolysis front in conjunction with a simple phase-change based pyrolysis model for LDPE, an Oseen approximation of the flow and a infinitely fast chemistry for gas-phase combustion. The model was then reduced to two parameters, the diffusive heat length and the heat conveyed from the flame to a flat surface, this latter depending only on the oxygen concentration in the oxidizer. The first parameters has been estimated from its definition whereas the second has been calibrated to match experimental flame spread rate as a function of the oxygen concentration for given wire geometry and ambient pressure and inflow velocity. The model with the calibrated parameters has been applied successfully to predict flame spread rates for other wire geometries and pressure conditions. A full validation of this model would require more experimental data on wire geometries and natures of the metallic core, which is a main perspective of this work.

The heat transfer mechanisms ahead of the pryolysis front have been investigated. The polymer has been shown to be thermally thick for all tested wire geometries. It has been showed that, in the preheat zone, the contribution of the flame flux dominate the LDPE heating process whereas the metallic core acts as a heat sink for the thinner LDPE coating and mainly as a heat source for the other wire geometries. Upstream to the preheat zone, the metallic core behaves as a heat source whatever the wire geometry, heating the polymer before it is heated by the flame itself.

3 Solid-phase modelling

Sommaire

Polymers have been used in a wide variety of industrial and household applications due to their common characteristics such as low density, low toxicity, good electrical insulation, chemical resistance, and mechanical durability [93]. However, their high flammability constitutes a major drawback for their applications [94]. Indeed, most thermoplastics are shown to undergo chemical decomposition during their gasification when exposed to an external heat flux. The long carbon chains that constitute polymeric materials break into smaller carbon-based gases, which are often flammable when exposed to ambient air. This process is referred to as pyrolysis. The engineering flame spread model developed in Chapter 2 over-simplifies this phenomenon, treating it as a phase-change. An improvement of this model should take the material's phase and chemical transformations into consideration in both preheat and pyrolysis zones. The fuel mass loss and heat release rates during the burning process may be then better understood and compared with experimental results.

The need to understand and predict their pyrolysis behavior and, as a result, their propensity to sustain and spread flames has motivated the development of simple pyrolysis models [43, 44]. Since then, generalized pyrolysis codes capable of simulating a wider range of degradation, smoldering and flaming combustion scenarios have been implemented [46, 45, 95]. These semi-empirical models, well-designed for the simulation of fire growth [96, 48], can effectively correlate the material properties to their thermal decomposition behavior, through physics-based descriptions of in-solid heat and mass transfer and simplified chemical processes. Pyrolysis modeling requires a robust reaction mechanism along with apparent properties including kinetics,

thermodynamics and heat and mass transport related parameters which most of time cannot be directly measured. A consequence is that a careful calibration process associated with an experimental database is necessary [49].

A solution for determining these core parameters was proposed by Lautenberger et al., based on the inverse modelling of bench-scale experiments [97]. However, the large number of unknown parameters may result in a non-unique solution when using a single reference experimental data and the domain of validity of the model can be limited to the conditions that were used during the calibration [98]. In order to overcome these limitations, Stoliarov and colleagues [50, 51, 79] proposed to obtain the kinetics, thermodynamics and transport related parameters from specific experiments that isolate the individual processes. In their strategy, thermogravimetric analysis (TGA) and differential scanning calorimetry (DSC) performed in an inert atmosphere were first used to develop a reaction mechanism of consecutive first-order reactions describing the polymer decomposition and to calibrate the relevant kinetics and thermodynamics parameters. Cone calorimeter experiments in an inert atmosphere were then used for inverse modelling, targeting the sample mass loss rate and surface temperature for calibrating the thermal parameters including conductivity and absorption coefficient of the condensed material and thus validating the overall model.

Modeling of TGA and DSC experiments are among the most frequently used techniques for building a semi-global reaction mechanism, as well as to establish the kinetics and thermodynamics parameters that control the degradation of pyrolyzable solids. The main advantage of these techniques lies on the minimization of the effects of heat and mass transport inside the sample, by using a small material sample (typically weighting 3-10 mg) in slow and steady heating rates (1-20 K min^{-1}) [99]. This allows the inverse modelling to exclude the transport from data analysis and interpretation. Modeling of the cone calorimeter has been of great interest in parameterization of pyrolysis codes [54, 97]. The radiation-driven gasification of the material under controlled, near one-dimensional heating conditions allows for analysis of the heat transfer through the solid and its effect on the material mass loss rate.

An in-house, semi-empirical pyrolysis model is developed in this chapter, inspired by both the Thermakin [45] and Gpyro [46] codes. The decision of an in-house code development is based on the final objective of coupling with CFD fire simulators developed in our group [86, 100]. The relevant kinetic, thermodynamic and thermal properties of each species and reactions that are involved in these processes must be then determined. The multi-step parameter fitting methodology for calibrating such parameters based on experimental procedures is presented, based on the works of Stoliarov and colleagues [50, 51, 79]. The required material properties which could be eventually inserted into the previously developed solid phase two-dimensional flame spread model may be then determined.

The model, used in the rest of this work, that predicts the materials thermal decompositions is first presented. The governing equations and assumptions are presented and discussed, along with the time and spatial discretization techniques and boundary conditions. After presenting these models, the material properties that need to be de-

termined will be evidenced. The methodology to calibrate them with the bench-scale experimental data will be then discussed. A brief description of each experimental procedure is first given, and their relevance on the determination of specific material parameters is explained. For illustration and verification purposes, the model and the methodology are applied to three materials previously investigated by Stoliarov and co-workers [50, 51]: polymethyl methacrylate (PMMA), high-impact polystyrene (HIPS) and polyoxymethylene (POM). The experiments performed in Refs. [50, 51] are used for calibration purposes and the retrieved parameters are compared with those obtained in these studies.

3.1 Numerical methodology

3.1.1 Governing equations

The numerical pyrolysis model is developed in this section. It solves the unsteady mass and energy conservation equations and can consider a reaction mechanism with first- and second-order chemical reactions. In line with the underlying thermally-thin assumption of simultaneous thermal analysis (TGA and DSC), a zero-dimensional version of the model was considered, i.e., only species mass conservation is solved with the time evolution of the temperature specified from the experimental test. On the other hand, a one-dimensional approach that considers heat and mass transfers within the condensed-phase is adopted when modelling cone calorimeter experiments. The chemical mechanism considers N_s chemical species involved in N_r first- or second-order reactions:

$$\theta_1 X_1 + \theta_2 X_2 \rightarrow \theta_3 X_3 + (1-\theta_3)\mathrm{GAS} + H, \tag{3.1}$$

where θ_i represent the stoichiometric coefficients and H is the heat of reaction. If gaseous degradation products are formed by a reaction, they are assumed to leave the condensed phase instantly, and therefore do not contribute to the current mass, thermal and kinetic properties.

The Arrhenius rate of reaction k_r^j, for the j^{th} reaction is computed as:

$$k_r^j = A_j \exp\left(\frac{-E_j}{\bar{R}T}\right) m_{X_1} m_{X_2} \tag{3.2}$$

where A_j and E_j are the Arrhenius pre-exponential factor and activation energy, and $\bar{R}$ is the molar gas constant. The symbol m_{X_i} denotes the mass of the component X_i. If the reaction is of first order, m_{X_2} is set equal to unity.

The mass conservation for the species i is:

$$\frac{dm_{X_i}}{dt} = \sum_{j=1}^{N_r} (-1)^{\sigma_j^i} \theta_i^j k_r^j \tag{3.3}$$

where t is time. The symbol σ_j^i is equal to 1 when i is a reactant in the j-th reaction and 2 when i is a product in the j-th reaction. The thermoplastic melting process may be also considered as a reaction, though it produces no impact on the material mass loss in the system.

In the one-dimensional version, the medium is composed of N_s condensed-phase components, each of mass m_i, volume Δx_i and density ρ_i. With the assumption that the gaseous products leave the condensed phase instantly, the total mass m and volume Δx are defined as:

$$m = \sum_{i=1}^{Ns} m_i, \tag{3.4}$$

and:

$$\Delta x = \sum_{i=1}^{Ns} \Delta x_i, \tag{3.5}$$

with $\Delta x_i = m_i/\rho_i$. In addition, the mass fractions Y_i and volume fractions ν_i can be defined as:

$$Y_i = m_i/m; \tag{3.6a}$$

$$\nu_i = \Delta x_i/\Delta x. \tag{3.6b}$$

Material components properties are model input. Each material property (density, ρ, heat capacity, c and thermal conductivity, k) is defined as an adjustable function of the temperature:

$$\phi = \phi_0 + \phi_1 T + \phi_2 T^2, \tag{3.7}$$

where ϕ can be either ρ, c or k. ϕ_0, ϕ_1 and ϕ_2 are fitting curve parameters. The material emissivity and radiation absorption coefficients must also be specified, as single (constant) values.

The material average conductivity is determined by calculating its upper and lower limits. When materials are stacked in uniform layers normal to the direction of heat flow, the average conductivity is obtained as [45]:

$$k_n = \frac{1}{\sum_{i=1}^{N_s} \frac{\nu_i}{k_i}}, \tag{3.8}$$

When layers are parallel to the direction of the heat flow, the thermal conductivity is [45]:

$$k_p = \sum_{i=1}^{N_s} k_i \nu_i. \tag{3.9}$$

Considering an arbitrary spatial distribution of components and that components do not affect the thermal conductivities of each other, the average thermal conductivity is assumed to be [45]:

$$k = \frac{k_n + k_p}{2}. \tag{3.10}$$

The heat conduction inside the condensed phase is described by the Fourier's law:

$$q_x = -k\frac{\partial T}{\partial x}, \tag{3.11}$$

where x is the axial coordinate, as illustrated in Fig. 3.3.

The thermal radiation from an external source is given by a generalized version of the Beer-Lambert law [45]:

$$\frac{\partial I_{ex}}{\partial x} = -I_{ex}\Sigma_{i=1}^{N_s}\Delta x_i \alpha_i, \tag{3.12}$$

where I_{ex} is the radiative flux in the x direction and α_i is the absorption coefficient of the i^{th} component. The energy reradiation is represented by [45]:

$$\frac{\partial I_{rr}}{\partial x} = \frac{\sigma T^4}{I_{ex^0}}\frac{\partial I_{ex}}{\partial x}, \tag{3.13}$$

where I_{rr} is the heat flux radiated by a material boundary, I_{ex}^0 is the external radiation incident onto that boundary and σ is the Stefan-Boltzmann constant.

The 1D conservation of energy is:

$$\sum_{i=1}^{N_s} c\frac{\partial}{\partial t}(m_i T) = \frac{\partial}{\partial x}\left(k\frac{\partial T}{\partial x}\right) + \frac{\partial I_{ex}}{\partial x} - \frac{\partial I_{rr}}{\partial x} + \sum_{j=1}^{Nr} H_j k_r^j. \tag{3.14}$$

where c is the average material specific heat, obtained by mass-weighting each component specific heats, $c = \frac{1}{m}\Sigma_{i=1}^{N_s} m_i c_i$.

3.1.2 Boundary conditions

A scheme of the one-dimensional material sample subjected to the cone heater flux is shown in Fig. 3.3. At the heated top surface, $x = 0$, the sample is subjected to the external incident heat flux:

$$I_{ex}^0 = (1 - R_{ex}) \times \dot{q}''_{\text{cone}}, \tag{3.15}$$

where R_{ex} is the material surface reflectivity and $\dot{q}''_{\text{cone}}$ is the radiant heat flux from the heating system. A constant value of $R_{ex} = 0.05$ is attributed, considering the average value of a large number of common polymers [52].

The boundary condition for heat losses at the top surface is given by:

$$k\frac{\partial T}{\partial x} = -\bar{h}_1(T - T_{\infty,top}) - \sigma\epsilon(T^4 - T^4_{\infty,top}), \tag{3.16a}$$

for $x = 0$,

The heat transfer coefficient h_1 is evaluated as $\bar{h}_1 = 5$ W m^{-2} K^{-1}, and the mean ambient temperature, $T_{\infty,top}$ evolves from $T_{\infty,top} = 330$ to $T_{\infty,top} = 380$ K as the radiant heat flux increases from $I^0_{ex} = 20$ to $I^0_{ex} = 70$ kW m^{-2} [101]. The radiative heat loss follows the Stefan-Boltzmann law, with an assumed emissivity of $\epsilon = 1.0$. The second term on the R.H.S. is not considered if the assumption that radiation emission penetrates the solid volume (3rd term on RHS of Eq. 3.14).

At the rear surface, $x = L$, the boundary condition is given by:

$$k\frac{\partial T}{\partial x} = -\bar{h}_2(T - T_{\infty,bottom}) - \sigma\epsilon(T^4 - T^4_{\infty,bottom}), \tag{3.16b}$$

For $x = L$.

$T_{\infty,bottom}$ is the mean ambient temperature computed for this region, given a constant value of $T_{\infty,bottom} = 310$ K. For the rear surface, the convection coefficient is evaluated as $\bar{h}_2 = 4$ W m^{-2} K^{-1} [101].

3.1.3 Numerical methods

The species mass fraction and heat transfer equations were solved by using the finite volume method with a first-order backward Euler scheme for time integration and a second-order centered scheme for the diffusion term [90]. The heat conductivity at the cell interface was computed with the harmonic mean. In addition, the consumption part of the reaction rates was treated implicitly to avoid nonphysical solutions [90]. The time step $\Delta t = 0.05$ s is used in all the configurations. Multiplying or dividing this value by 5 was found to provide minor changes on the results. In the 1D model, the spatial discretization is initially uniform, with a cell size of $\Delta x = 0.025$ mm. Multiplying or dividing this value by a factor of 2 was found to provide minor changes on the results. The release of pyrolysis gases induces change in the size of each cell. To account for this process a resizing of each cell element is done at the end of each time step:

$$\Delta x^n = \Delta x^{n-1}\frac{m^n}{m^{n-1}}. \tag{3.17}$$

The subscripts n and $n-1$ denote the current and previous time steps, respectively.

3.1.4 Model parameters and optimization

The material kinetic, thermodynamic and thermal apparent properties needed to describe the degradation of polymers appears clearly from the governing equations on the last section. In order to describe material phase changes and/or thermal decompositions, the Arrhenius pre-exponential factor A_j, activation energy E_j, stoichiometric coefficients and heat of reaction H_j for each j^{th} reaction are needed. The density ρ_i and heat capacity c_i for each i^{th} component also need to be determined, as a function of temperature. When heat transport plays a significant role inside the condensed phase, thermal conductivities k_i (also as a function of temperature) must be set for each individual species. The polymers density are shown to be well documented by the literature [91], and no further experiments have been conducted for their determination. The aforementioned properties have been calibrated by inverse modeling, i.e., fitting the developed models into gasification experiments data.

Table 3.1 summarizes each relevant kinetic, thermodynamic and thermal parameters and the experimental procedures used for their determination. Details and relevance of each procedure, as well as the fitting methodology are discussed in the next section.

Property	Symbol	Experimental procedure
Arrhenius pre-exponential factor	A	TGA
Arrhenius activation energy	E	TGA
Stoichiometric coefficient	θ	TGA
Heat of reaction	H	DSC
Heat capacity	c	DSC
Thermal conductivity	k	Cone calorimeter
Absorption coefficient	α	Cone calorimeter

Table 3.1: Kinetic, thermal and thermodynamic parameters describing the polymer pyrolysis.

Final determination of the model parameters is obtained from inverse numerical modelling of the experiments presented in Table. 3.1. The optimization was performed by using an evolutionary optimization algorithm, the Shuffled Complex Evolution (SCE) [102]. Its accuracy, efficiency, and robustness have been verified in previous pyrolysis parameters optimization [53]. A general description of the SCE steps is presented here, and an overall functionality of the optimization algorithm is shown in Fig. 3.1. A more detailed presentation of the underlying theory of the algorithm can be found in Refs. [102, 103].

1. **Sample generation:** s sample points are randomly generated within the feasible parameter spectrum and the criterion value is computed at each point. In this work, the criterion value is the relative discrepancy to the targeted experimental

data. The root mean squared relative error was used to compute the difference between the experimental and modeled data in the optimization process:

$$\text{RMSRE} = \sqrt{\frac{1}{N}\sum_{i=1}^{n}\left(\frac{X_i - P_i}{P_i}\right)^2}, \tag{3.18}$$

where N is the total number of sample points and X and P represent the modeled and experimental data, respectively. The targeted experimental points used for optimization are precised for each situation in their corresponding results section. This initial random sampling provides the potential for locating the global optimum without being biased by pre-specifying starting points.

2. **Point ranking:** The s point are sorted in order of increasing RMSRE.
3. **Partition into complexes:** The s points are partitioned into p complexes, each containing m points ($s = p \times m$). The partition in more numerous communities enhances the exploration of the feasible space in more directions, allowing for the possibility that the problem has more than one region of attraction.
4. **Evolution of complexes:** Complexes are evolved using the competitive complex evolution (CCE) algorithm. This algorithm is based on the Nelder and Mead Simplex downhill search scheme [104], which introduces competitiveness by forming subcomplexes, promoting search towards promising regions. Further details regarding this algorithm can be found in refs. [104, 102, 103].
5. **Shuffling the complexes:** The points of the evolved complexes are recombined into a single sample population. The s points are re-sorted in order of increasing RMSRE value and re-partitioned into p complexes as specified in steps 2 and 3.
6. **Check convergence:** If the pre-specified convergence criteria is satisfied, stop; otherwise, continue.
7. **Reduction in the number of complexes:** As long as the number of complexes p is greater than the minimum established value p_{min}, remove the complex with the lowest ranked value $p = p - 1$ and $s = p \times m$. Return to step 4.

The targeted data for parameter fitting in TGA was the mass loss and mass loss rate of the sample. For the cone calorimeter data, the mass loss rate (or heat release rate in a non-inert atmosphere) and back surface temperature were considered.

3.2 Experimental procedure

The adopted experimental procedure for determining the relevant kinetic, thermodynamic and thermal parameters identified in the previous section for the studied pyrolyzing thermoplastics [50, 51].

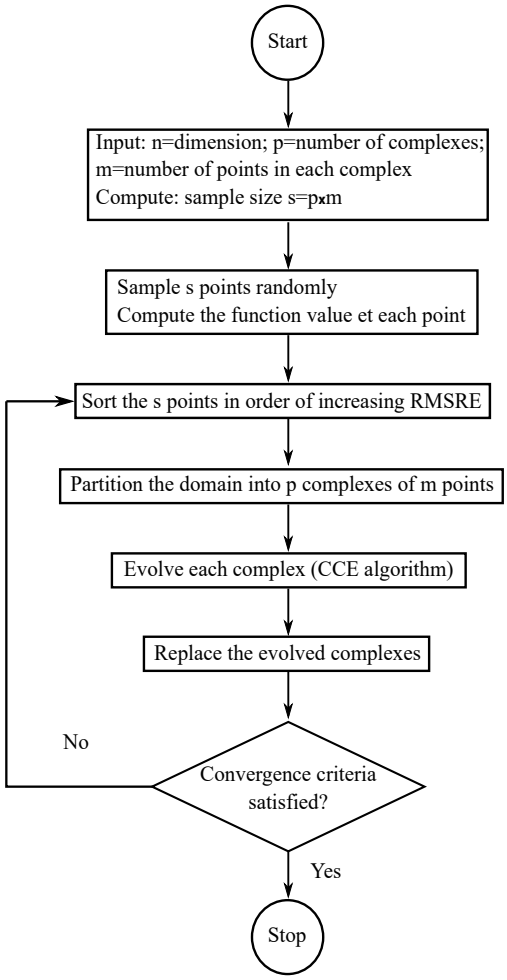

Figure 3.1: Flow chart of the shuffled complex evolution method. Adapted from Duan et al. 1993 [102].

The first step of the parameter fitting methodology involves the analysis and interpretation of Simultaneous Thermal Analysis (STA) experiments. It comprises two experimental techniques, simultaneously employed to determine, on the one hand, the kinetics and, on the other hand, the thermodynamic parameters: a thermogravimetric analysis (TGA) and differential scanning calorimetry (DSC). A schematic of the STA configuration is shown in Fig. 3.2.

TGA is a technique where the mass of a material is measured as a function of temperature or time while the sample is subjected to a controlled temperature program in a controlled atmosphere [105]. The temperature program in commercial TGAs typically vary between ambient temperature to 1200 K or higher, which is sufficient to analyse the polymers full degradation process. As shown in Fig. 3.2, a purge gas, commonly nitrogen, flows through the balance to ensure an inert atmosphere. Additionally, the moisture content of the purge gas can be controlled. Typical sample size ranges from

3 to 10 mm, which ensures a constant temperature inside the material throughout the heating program. With the assumption that the polymers degrade through consecutive Arrhenius-based reactions, their respective decomposition kinetics parameters may be determined by the aforementioned zero-dimensional numerical model, by fitting into the material mass and mass loss profile.

DSC measures the heat flux with respect to a reference as a function of temperature (see Fig. 3.2). In this process, the difference in the amount of heat required to increase the temperature of a sample and a reference is measured as a function of temperature. Sample and reference are maintained at the same temperature throughout the experiment. DSC curves plot the heat flux versus temperature or time. The heat capacity, the heat of melting and the heat of decomposition can be determined by this technique.

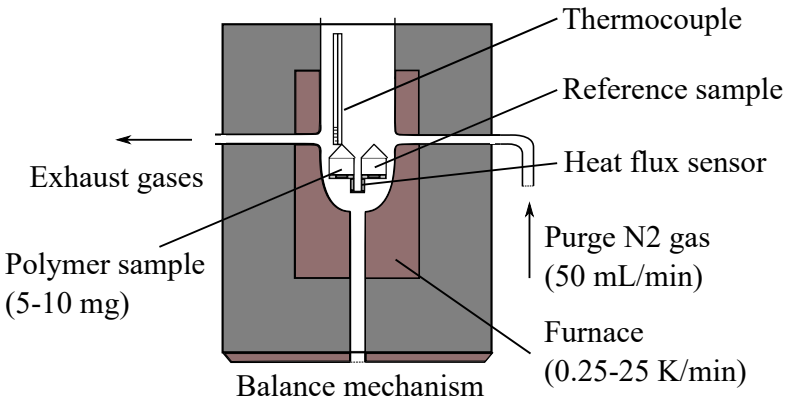

Figure 3.2: Schematic of the simultaneous thermal analysis configuration.

Once the kinetic Arrhenius parameters, heat capacities and heats of melting and decomposition are obtained, the heat transport related properties are obtained through gasification experiments of thermally-thick samples under specified heat fluxes. A schematic of the one-dimensional configuration for a radiation-driven pyrolysis under a cone calorimeter is shown in Fig. 3.3. This experiment typically considers an extruded sheet of a polymeric material, with an initial length, mass and temperature of $L = L_0$, $m = m_0$ and $T = T_\infty$, respectively, exposed to a controlled radiant heat of $I^0_{ex} = \dot{q}''_{\text{cone}}$. The temperature evolution at the rear surface, as well as its mass evolution may be measured, and these data are fitted by the aforementioned one-dimensional model and optimization algorithm to determine the material thermal conductivity evolution with temperature, as well as for validating the whole pyrolysis model.

For the experimental data used in this chapter [51], gasification experiments have been performed in a cone calorimeter with samples of L = 6-7 mm under controlled radiant heating in an inert atmosphere. Additionally, the radiant heat was assumed to be fully absorbed at the solid top surface. A consequence is that the material absorption coefficient does not need to be determined. A precision balance is used to monitor the sample mass. An infrared camera pointed at the back surface of the polymer sheet allows for measuring the back surface temperature, granting additional

data for the model calibration and verification.

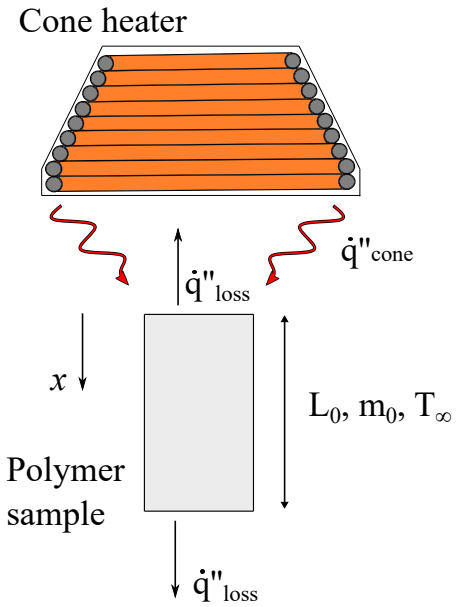

Figure 3.3: Schematic of a one-dimensional pyrolysis of a polymer sample under a cone calorimeter configuration.

3.3 Model calibration methodology

The methodology for parameter calibration over the three experimental procedures described in the last section is presented in this section [50, 51]. The step-by-step procedures for parameter fitting of polyoxymethylene (POM) are explained. The experiments used for parameters determination are taken from Refs. [50, 51]. This material has been chosen for this purpose because it is characterized by a melting process and two chemical reaction decompositions, allowing for a complete analysis of each experimental and numerical procedure. The resulting fitted parameters are then compared with the ones retrieved from the original study of Stoliarov and colleagues [50, 51], and differences between the obtained values are discussed.

The TGA of POM is presented in Fig. 3.4. In these figures and, in the following of the manuscript, m, m_0 and $MLR = dm(t)/dt$ represent the current mass, the initial mass and the mass loss rate, respectively. The left-side column (index a) shows the ML whereas the right-side column (index b) shows the MLR. Analysis from mass loss rate of POM from Fig. 3.4(b) shows two peaks. Each is attributed to a distinct chemical reaction.

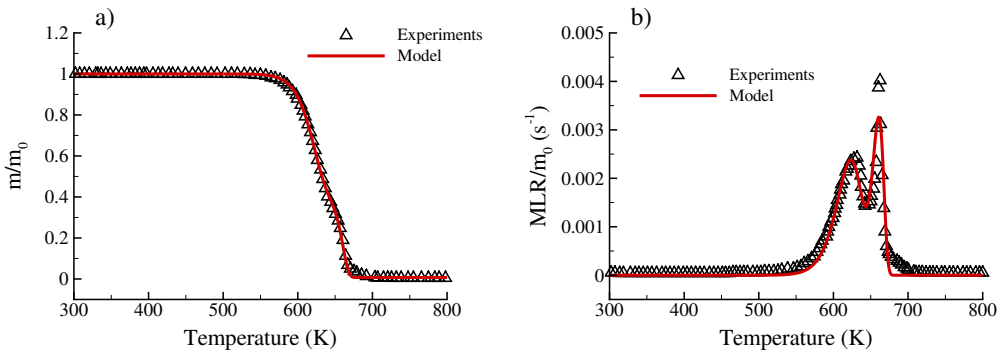

Figure 3.4: Experimental [50] and fitted model for TGA of POM at 10 K min^{-1}. (a) Normalized mass of the burning sample as a function of temperature. (b) Normalized mass loss rate as a function of temperature.

Moreover, differential scanning calorimetry (DSC) suggests a third peak of heat flow, at a lower temperature than the other two, as shown in Fig. 3.5. It is not accompanied by mass loss, and it is therefore assumed to be associated to the phase change (melting) process.

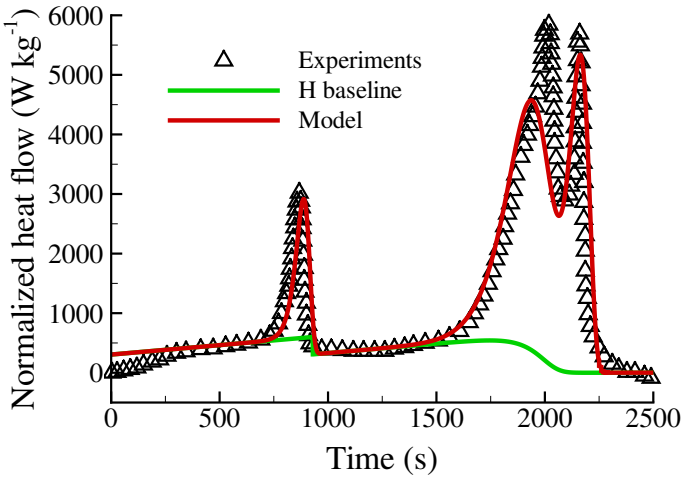

Figure 3.5: Experimental [50] and simulated DSC of POM at a heating rate of 10 K min^{-1}.

With the gathered information of decompositions and phase-change process, the reactions are schematized here, and the first parameters to be determined are evidenced:

$$\begin{aligned} \text{POM} &\rightarrow \theta_m \text{POM\_melt} + \text{H}_m; \\ \text{POM\_melt} &\rightarrow \theta_1 \text{POM\_int} + \text{H}_1; \\ \text{POM\_int} &\rightarrow \theta_2 \text{POM\_res} + \text{H}_2. \end{aligned} \tag{3.19}$$

Number subscripts represent decomposition reactions, while m represents the melting reaction. Subscripts $melt$, int and res represent the distinct components of POM degradation: melting, intermediate component and residue, respectively.

The mass loss and mass loss rate are obtained by solving Eq. 3.3. Fitting the experimental data allows for calibration of the Arrhenius pre-exponential and activation energy. An initial guess for these values are obtained from the following expressions [50]:

$$E = \frac{eRT_{max}^2 \frac{\text{MLR}_{max}}{m_{init}}}{(1-\theta)\frac{dT}{dt}}, \tag{3.20}$$

$$A = \frac{\text{MLR}_{max}}{m_{init}} \exp\left(\frac{E}{RT_{max}}\right). \tag{3.21}$$

Here, the subscript max represents the maximum values taken at maximum of the corresponding mass loss rate peak. m_{init} is the initial reactant mass and e is the base of the natural logarithm. The subsequent refinement of these parameters was obtained with inverse modelling of the material mass loss and mass loss rate data, with the optimization algorithm described in section 3.1.4.

As shown in Fig. 3.4, tendencies for mass loss and mass loss rate were well captured by the fitted model, considering both reactions. The second peak has been slightly under-predicted in this fitting. Property names, units, values and error margins (if any) are documented in Table 3.2. Even though good fitting with experimental data was achieved, the optimized values occasionally diverged from the values determined in the literature [50, 51]. This corroborates the statement of a non-unique solution for the model input parameters.

Once the kinetic Arrhenius parameters are obtained, the heat capacities, heats of reaction and melting may be determined from DSC data, presented in Fig. 3.5. Heat capacities of solid and melted phases may be extracted directly from measured heat flow data. Solid POM is assumed to be the only specie in the region before the heat flow peak attributed to melting. The region after the melting peak and before the reaction peaks are assumed to represent melted POM only. A simple linear fit is executed in these areas in order to obtain the heat capacities that correspond with the predominant condensed material. A heat flow baseline is computed to account for the pure heat flow that corresponds to the material heating as if no chemical reactions

Property	Unit	Value	Error	Literature value [50, 51]
A_1	s^{-1}	4.34×10^{14}	50 %	3.84×10^{14}
E_1	kJ mol^{-1}	187	5 %	200
θ_1	-	0.400	-	0.400
A_2	s^{-1}	9.46×10^{35}	20 %	4.76×10^{44}
E_2	kJ mol^{-1}	466	2 %	590
θ_2	-	0.018	-	0.018
A_m	s^{-1}	2.70×10^{42}	-	2.70×10^{42}
E_m	kJ mol^{-1}	382	-	382
H_1	kJ kg^{-1}	1005	5 %	1192
H_2	kJ kg^{-1}	1700	5 %	1352
H_m	kJ kg^{-1}	192	6 %	192
c_{POM}	kJ kg^{-1} K^{-1}	$-1.60 + 0.011T$	-	$-1.86 + 0.0099T$
$c_{\text{POM\_melt}}$	kJ kg^{-1} K^{-1}	$3.36 + 0.0011T$	-	$1.65 + 0.0012T$
$c_{\text{POM\_int}}$	kJ kg^{-1} K^{-1}	$3.36 + 0.0011T$	-	$1.65 + 0.0012T$
k_{POM}	W m^{-1} K^{-1}	$0.44 + 7.5 \times 10^{-4}T$	-	$0.25 + 1.6 \times 10^{-5}T$
$k_{\text{POM\_melt}}$	W m^{-1} K^{-1}	$0.29 - 4.9 \times 10^{-5}T$	-	$0.21 + 8 \times 10^{-6}T$
$k_{\text{POM\_int}}$	W m^{-1} K^{-1}	$0.25 - 1.4 \times 10^{-5}T$	-	$0.19 + 6 \times 10^{-5}T$

Table 3.2: Kinetic, thermal and thermodynamic parameters describing POM melting and decomposition.

or melting occurred. The heat flow difference between experimentally measured and the baseline is integrated in time in order to obtain the heats of melting and decomposition. In the case of POM, where the two chemical reactions juxtapose, a total heat of degradation may be obtained ($H_1 + \theta_1 H_2$), and fitting of the solution of the zero-dimensional version of Eq. 3.14 allows for determination of heats of the first and second reactions. A good prediction of the melting reaction is obtained. The optimization of the combined parameters allowed for the separation between heats of decomposition of the two reactions, and a relatively good fitting is obtained.

The cone calorimeter experimental data is used as means of thermal conductivities determination and overall model verification. Six sets of experimental data are used for the model fitting: mass loss rate and back surface temperature as a function of time, for three different levels of radiant heat flux. Solution of Eq. 3.3 and Eq. 3.14 allows for determining the thermal conductivities as a function of temperature for each individual chemical species.

Cone calorimeter experiments and numerical fitting are shown in Fig. 3.6 and Fig. 3.7. Model results are within 5 % for back surface temperature measurements. Agreement with measurements of mass loss rate is also remarkable, considering the complexity of this material.

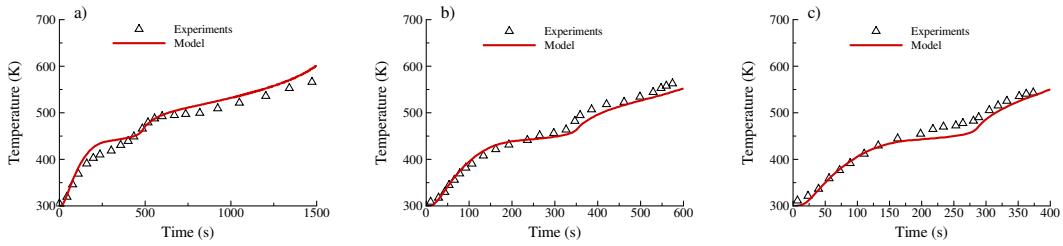

Figure 3.6: Experimental [51] and simulated back surface temperature histories obtained for POM at different radiant heat intensities. (a) $\dot{q}''_{\mathrm{fl}} = 30$ kW m^{-2}; (b) $\dot{q}''_{\mathrm{fl}} = 50$ kW m^{-2}; (c) $\dot{q}''_{\mathrm{fl}} = 70$ kW m^{-2}.

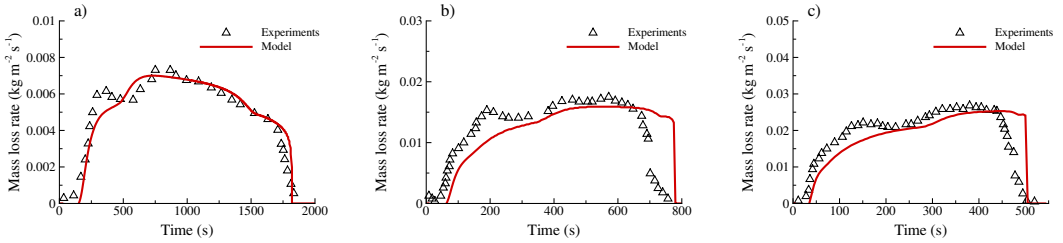

Figure 3.7: Experimental [51] and simulated mass loss rate histories obtained for POM at different radiant heat intensities. (a) $\dot{q}''_{\mathrm{fl}} = 30$ kW m^{-2}; (b) $\dot{q}''_{\mathrm{fl}} = 50$ kW m^{-2}; (c) $\dot{q}''_{\mathrm{fl}} = 70$ kW m^{-2}.

3.4 Results and discussion

The parameter-calibrated model fittings are now presented over their correspondent experimental data [50, 51] for the other two tested materials in this section. The calibrated parameter values are presented and discussed.

3.4.1 Polymethylmethacrylate (PMMA)

PMMA shows a change in its structure to a glass phase at $T = 403$ K. This is assumed to occur instantly when the material reaches this temperature, and causes a change in its thermal conductivity. The calibrated PMMA parameters are shown in Table 3.3.

The fitted zero-dimensional model over the TGA experimental data [50] is presented in Fig. 3.8. The mass evolution normalized by the initial mass as a function of temperature is shown in Fig. 3.8(a), and the normalized mass loss rate is depicted in Fig. 3.8(b). For PMMA, only one reaction is considered, based on the single mass loss rate peak at $T \approx 650$ K. A good agreement is obtained with experimental results for both cases.

Property	Unit	Value	Error	Literature value [50, 51]
A_1	s^{-1}	3.80×10^{12}	40 %	8.6×10^{12}
E_1	kJ mol^{-1}	183	2 %	188
θ_1	-	0.015	-	0.015
H_1	kJ kg^{-1}	915	5 %	846
c_{PMMA}	kJ kg^{-1} K^{-1}	$1.27 + 0.0006T$	-	$0.6 + 0.0036T$
c_{PMMA_glass}	kJ kg^{-1} K^{-1}	$1.27 + 0.0006T$	-	$0.6 + 0.0036T$
k_{PMMA}	W m^{-1} K^{-1}	$0.49 - 4.7 \times 10^{-4}T$	-	$0.45 - 3.8 \times 10^{-4}T$
k_{PMMA_glass}	W m^{-1} K^{-1}	$0.42 - 4.6 \times 10^{-4}T$	-	$0.27 - 2.4 \times 10^{-4}T$

Table 3.3: Kinetic, thermal and thermodynamic parameters describing PMMA melting and decomposition.

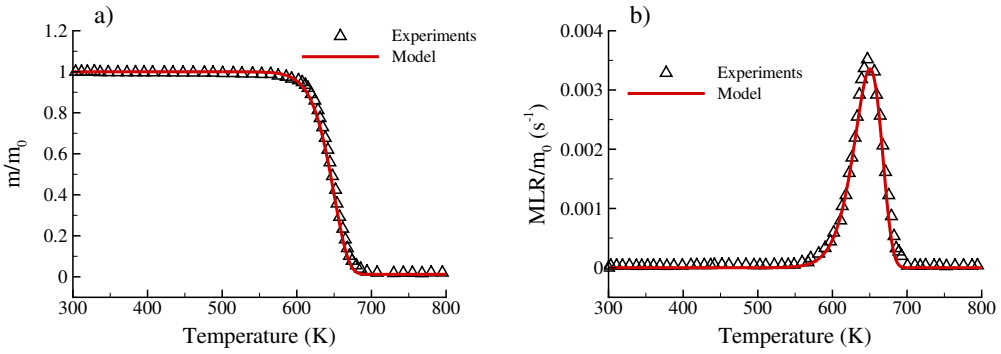

Figure 3.8: Experimental [50] and fitted model for TGA of PMMA at 10 K min^{-1}. (a) Normalized mass of the burning sample as a function of temperature. (b) Normalized mass loss rate as a function of temperature.

Figure 3.9 shows the experimental and numerically fitted evolution of the mass-normalized heat flow in time, obtained at the differential scanning calorimetry experiments. The heat flow baseline is also displayed, evidencing the area that is integrated in order to determine the heat of decomposition. A slight shift of the reaction peak may be observed this time for the model, when using the recently determined Arrhenius parameters. These properties will be later re-calibrated over the cone calorimeter experiment, considering their error margins.

The final thermal parameters are calibrated, along with the gathered parameters from TGA and DSC on the cone calorimeter gasification experiments. PMMA possesses the particularity of a glass phase change, assumed to happen instantaneously at $T = 403$ K. As a consequence, additional thermal conductivities must be recalculated through the optimization procedure.

The back surface temperature evolution in time for the PMMA gasification is analysed in Fig. 3.10, for three levels of incident heat flux. Good agreement with experi-

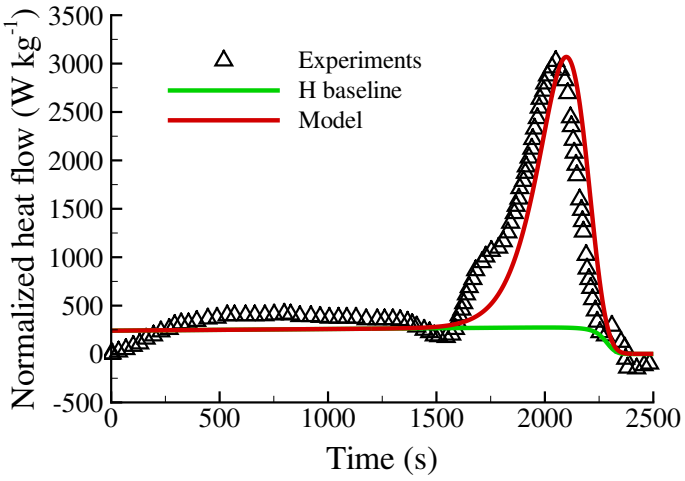

Figure 3.9: Experimental [50] and simulated DSC of PMMA at a heating rate of 10 K min^{-1}.

mental results is obtained for all three cases.

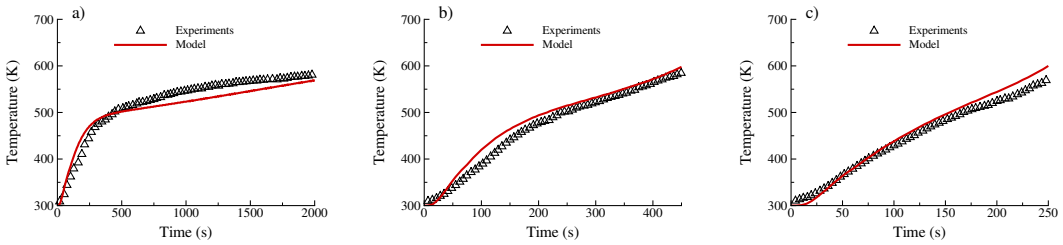

Figure 3.10: Experimental [51] and simulated back surface temperature histories obtained for PMMA at different radiant heat intensities. (a) $\dot{q}''_{fl} = 20$ kW m^{-2}; (b) $\dot{q}''_{fl} = 40$ kW m^{-2}; (c) $\dot{q}''_{fl} = 60$ kW m^{-2}.

Mass loss rate data is also used as means of parameter fitting. The one-dimensional model results fitted over the experimental data are shown in Fig. 3.11. The agreement is not perfect, but the curves tendencies are well captured for the three tested radiant heat levels.

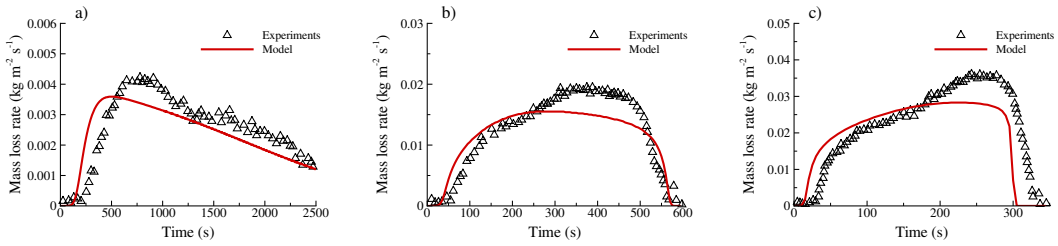

Figure 3.11: Experimental [51] and simulated mass loss rate histories obtained for PMMA at different radiant heat intensities. (a) $\dot{q}''_{\text{fl}} = 20$ kW m^{-2}; (b) $\dot{q}''_{\text{fl}} = 40$ kW m^{-2}; (c) $\dot{q}''_{\text{fl}} = 60$ kW m^{-2}.

3.4.2 High-impact polystyrene (HIPS)

The same procedure is now applied for parameter calibration over gasification experiments of high-impact polystyrene. This may be considered as the "simplest" material over the three tested polymers in this section. Similarly to PMMA, it possesses only one chemical reaction, as evidenced by TGA results, and no melting reaction, as evidenced by DSC results. Moreover, no other particular phase transition is observed. Therefore, one set of chemical reaction parameters needs to be determined, as well as thermal properties for only one species. The calibrated parameters are shown in Table 3.4.

Property	Unit	Value	Error	Literature value [50, 51]
A_1	s^{-1}	2.42×10^{19}	40 %	1.7×10^{20}
E_1	kJ mol^{-1}	285	5 %	301
θ_1	-	0.043	-	0.043
h_1	kJ kg^{-1}	716	5 %	689
c_{HIPS}	kJ kg^{-1} K^{-1}	$2.23 + 0.0002\,T$	-	$0.59 + 0.0034\,T$
k_{HIPS}	W m^{-1} K^{-1}	$0.49 - 6.3 \times 10^{-4}\,T$	-	$0.1 + 1.0 \times 10^{-4}\,T$

Table 3.4: Kinetic, thermal and thermodynamic parameters describing HIPS thermal decomposition.

The fitted TGA model is first presented in Fig. 3.12. The curve tendencies are similar to TGA of PMMA. Good agreement is observed for mass loss and mass loss rate curves.

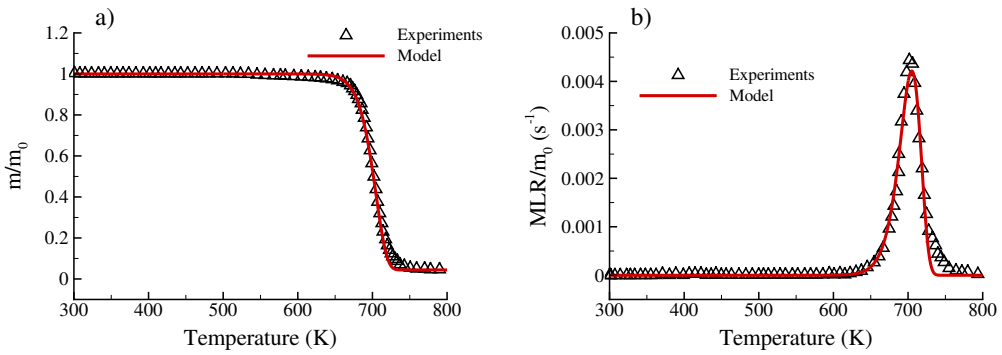

Figure 3.12: Experimental [50] and fitted model for TGA of HIPS at 10 K min^{-1}. (a) Normalized mass of the burning sample as a function of temperature. (b) Normalized mass loss rate as a function of temperature.

The DSC of HIPS is presented in Fig. 3.13. Once more, curve tendencies are well predicted, though the pre-calibrated Arrhenius parameters under-predict its heat flow of the reaction peak. The inert heat flow baseline is also plotted for evidencing the reaction heat of decomposition, which is considerably smaller in magnitude that the one observed for PMMA.

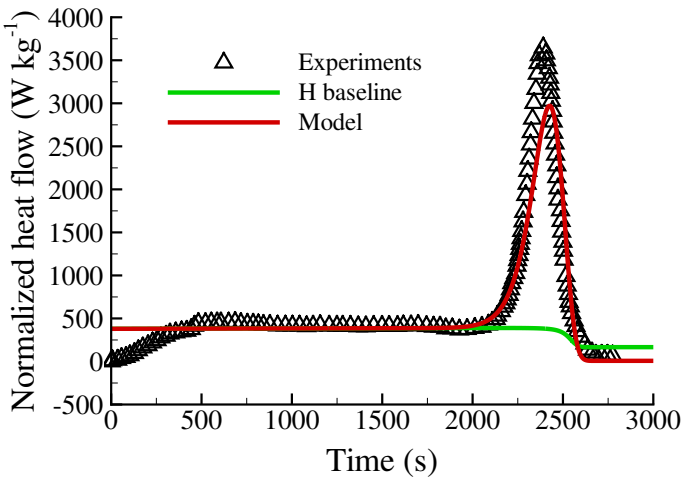

Figure 3.13: Experimental [50] and simulated DSC of HIPS at a heating rate of 10 K min^{-1}.

The cone calorimeter experiments and fitted model results are finally presented in Fig. 3.14 and Fig. 3.15. It can be said that a good agreement with experimental results has been achieved for both set of data, for the three heat flow intensities. Moreover, numerical results were largely similar to the original fitted model, even if different

properties were determined. This corroborates again the statement of non-unique solution for these parameters fitting.

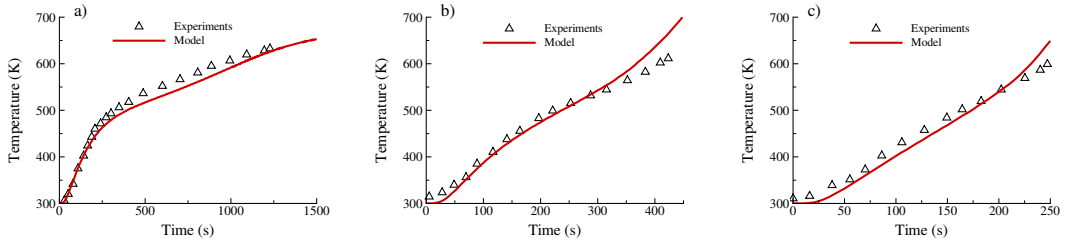

Figure 3.14: Experimental [51] and simulated back surface temperature histories obtained for HIPS at different radiant heat intensities. (a) $\dot{q}''_{\mathrm{fl}} = 30$ kW m^{-2}; (b) $\dot{q}''_{\mathrm{fl}} = 50$ kW m^{-2}; (c) $\dot{q}''_{\mathrm{fl}} = 70$ kW m^{-2}.

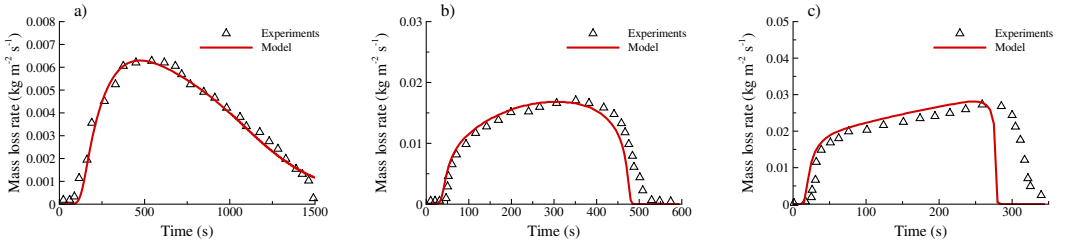

Figure 3.15: Experimental [51] and simulated mass loss rate histories obtained for HIPS at different radiant heat intensities. (a) $\dot{q}''_{\mathrm{fl}} = 30$ kW m^{-2}; (b) $\dot{q}''_{\mathrm{fl}} = 50$ kW m^{-2}; (c) $\dot{q}''_{\mathrm{fl}} = 70$ kW m^{-2}.

3.5 Conclusions

In order to predict the polymers behaviour as they thermally degrade, a numerical pyrolysis model that is to be implemented on the flame spread model has been developed. The governing equations of the zero and one-dimensional approaches have been presented, as well as their boundary conditions. This model requires the determination of several material parameters, related to their kinetic, thermodynamic and transport properties. A methodology has been applied to calibrate these parameters over three experimental procedures: thermogravimetric analysis, differential scanning calorimetry and cone calorimeter gasification. An optimization algorithm has been employed for calibrating the numerical results using the same configurations of each experiments, allowing to determine each material parameter. Three polymers have been investigated for these purposes: polymethylmethacrylate (PMMA), high-impact polystyrene (HIPS) and polyoxymethylene (POM). A last comparison of each numeri-

cal results with their corresponding experimental data shows good agreement, thus validating the developed model and optimization procedures.

The calibrated properties have often diverged from other models observed in the literature, even if extremely similar results of mass loss, mass loss rate, heat flow and back surface temperature were obtained. This corroborates the assessment that the solution is not unique, and therefore a methodology that calibrates one (or one small group of) parameter at a time over numerous experiments is necessary in order to minimize errors.

Overall agreement with experimental results is remarkable. In the case of PMMA cone calorimeter fitting, a larger discrepancy has been observed. This may be due to this material change to glass phase from a certain temperature, and it could result in a difficulty to predict the material thermal transport within the material. Numerical results for HIPS and POM (not shown) have been identical to the Thermakin code, when using the same properties and configurations.

Thermal conductivities have been shown to be particularly difficult to determine with precision. A slight change in other parameters or configurations has resulted in large changes of this property among a material's components. This problem has also been observed in other studies [46]. This should not result in significant error propagation when applying the developed pyrolysis model inside the 2D flame spread. As thoroughly discussed in Chapter 2, heat transfer is significantly more impactful inside a metallic wire core than in its polymer insulation.

The implementation of this model on the tested low-density polyethylene (LDPE) coating is the subject of the next chapter. The gasification of this material on a non-inert atmosphere (i.e. in the presence of oxygen) needs be considered, as combustion will occur and new heat fluxes must be taken into consideration. The model must be then reformulated to a two-dimensional (in cylindrical coordinates) model, and attention must be drawn to the material deformation, since LDPE shows a change in its density with the temperature increase.

4 Thermal decomposition of low-density polyethylene

Sommaire

Polyethylene, with its broad spectrum of attractive physical properties, is employed in a multitude of industrial applications, such as packaging, containers, piping, wire and cable insulation [106]. It also has potential consideration for applications in the context of space exploration, which is the current research interests of the authors, as polyethylene-based composite materials are currently being investigated as a solution for radiation shielding material in spacecrafts [107]. However, its high flammability constitutes a major drawback for these applications. Such as studied in Chapter 2, the variant low-density polyethylene (LDPE) has been used as coating of laboratory wires as an international target configuration to investigate flammability properties of electrical cables in both normal and microgravity conditions [22, 86, 30, 100]. It is therefore of great interest to understand and predict the thermal decomposition of this material.

In this chapter, the previously developed and validated pyrolysis code is applied to simultaneously reproduce the thermal decomposition of LDPE in the aforementioned described experimental procedures. The experiments (TGA, DSC, cone calorimeter) reported in this Chapter and the next one have been conducted at the UMET Lille in collaboration with Professor Serge Bourbigot. The cone calorimeter experiments have been performed in a non-inert atmosphere. In this configuration, a flame that covers the pyrolysing sample is observed once ignition occurs. As a consequence, additionally to the heat flux from the cone heater, an flame heat flux must be modeled over the solid top surface. An empirical flame model for the burning of common polymer samples has been proposed by Stoliarov [48], where the interaction between the flame

and the sample surface was characterized by adding a 12-24 kW m^{-2} radiative heat flux source term once ignition occurs. This heat flux was not directly measured but was determined from inverse analysis of the burning material heat release rate (HRR).

In the next section, the material is described, along with its previously gathered properties. The experimental methodologies are also presented. In the following section, the results relative to TGA and DSC experiments are first discussed, followed by those concerning the cone calorimeter experiments. Details about the determination of the flame heat flux are presented. Finally, the conclusions drawn from this study are summarized.

4.1 Numerical methodology

The methodology and details for determining the apparent properties that control the thermal degradation of LDPE have been presented in Chapter 3. Modelling of the gasification experiments follows the governing equations presented in section 3.1. The parameter calibration methodology is thoroughly described in section 3.2 and the optimization of the model parameters uses the algorithm described in section. 3.1.4.

Due to a non-inert atmosphere in the cone calorimeter experiments, a flame appears over the pyrolyzing LDPE surface which alters the incident heat flux onto the top sample surface. The boundary conditions are thus updated to account for the flame heat feedback. Once ignition occurs, the modeled incident heat flux, which differs from Eq. 4.1 from Chapter 3, becomes:

$$I^0_{ex} = (1-R) \times (\dot{q}''_{\text{cone}} + \dot{q}''_{\text{flame}}), \tag{4.1}$$

where $\dot{q}''_{\text{flame}}$ is the flame heat flux, applied once the sample is ignited. Consistently with the modelling approach of Stoliarov et al. 2009 [48], the flame heat flux is assumed to be radiative in nature and will be determined by fitting the results of one of the cone calorimetry experiments. Ignition is assumed to occur (t_{ig}) when the solid surface reaches its pyrolysis temperature T_{pyr} (see Table 4.1). The surface reflectivity is set to $R = 0.05$ (Table 4.1). Prior to ignition, boundary conditions are described in Eq. 3.16. After ignition, heat losses are neglected at the top surface:

$$k\frac{\partial T}{\partial x} = 0, \tag{4.2}$$

for $x = 0$, $t > t_{ig}$.

4.2 Experimental methodology

4.2.1 Material

LDPE was supplied by Sabic (Netherlands) in the commercial grade Sabic®LDPE 2602X1 00900. The LDPE properties, also discussed in Chapter 2, are presented in Table 4.1. The broadband surface reflectivity was estimated from the average of a wide range of thermoplastics [52].

Property	LDPE_solid	LDPE_melt
Density, ρ (kg/m^3)	948.2	$948.2 - 0.94 \times (T - T_\infty)$
Reflectivity, R	0.05	0.05
Pyrolysis temperature, T_{pyr} (K)	-	660

Table 4.1: LDPE properties.

4.2.2 Simultaneous Thermal Analysis (STA)

Thermogravimetric analysis (TGA) and Differential scanning calorimetry (DSC) were conducted simultaneously using a Netzsch 449 F3 Jupiter thermal analyser. An overall configuration of these experiments has been shown in Fig. 3.2. STA tests utilized a temperature program that consisted of a conditioning period, when the sample was maintained at 303 K for 25 min, followed by linear heating at a nominal rate of 5 K min^{-1}. This heating rate was chosen to be sufficiently slow to ensure that the sample did not experience significant temperature or composition gradients. The samples were heated through decomposition up to the temperature where no significant mass loss was detected.

Additional TGA tests were carried out using a Netzsch TG 209 F1 Libra at five linear heating rates of 1,2,5,10 and 20 K min^{-1} from 300 K to 1000 K. These heating rates were generally sufficiently slow to ensure that the sample did not experience significant temperature or composition gradients. The tests were performed in an anaerobic environment established by continuously purging the furnace with nitrogen at a flow rate of 50 cm^3 min^{-1}. Samples of an initial mass of m_0 = 10 mg (±0.3 mg) were put in open alumina pans to maximize temperature uniformity. The sample mass was collected as a function of time and temperature. Each test was repeated 3 times and recorded mass signals were averaged prior to further analysis. The TGA experiments provide the evolution of the sample mass loss (ML) and mass loss rate (MLR) with the temperature and the peaks of MLR are interpreted as apparent chemical reactions. So, this approach does not resolve the detailed chemical species involved in the decomposition.

4.2.3 Cone calorimetry

FTT (Fire Testing Technology) Mass Loss Calorimeter (MLC) was used to carry out measurements on samples following the procedure defined in ASTM E 906. An overall configuration of these experiments has been shown in Fig. 3.3. The equipment is identical to that used in oxygen consumption cone calorimetry (ASTM E-1354-90), except that a thermopile in the chimney is used to obtain heat release rate (HRR) rather than employing the oxygen consumption principle. The procedure consists in exposing 100 mm×100 mm×6 mm samples in a horizontal orientation to external radiative heat fluxes of 25, 35, 50 and 60 kW m^{-2}. The heat flux of 35 kW m^{-2} corresponds to a common heat flux in a mild fire scenario [63]. MLC was used to determine heat release rate (HRR) and total heat release (THR). When measured at 35 kW m^{-2}, HRR is reproducible within ±10 %. The cone data reported in this work are the average of two replicated experiments.

4.3 Results and analysis

4.3.1 STA Experiments

The mean experimental DSC data of LDPE at a heating rate of 5 K min^{-1} is shown in Fig. 4.1. The peak normalized heat flow depicted in Fig. 4.1 occurs at a temperature of $T \approx 400\ K$. Since no mass loss was found to be associated to this process in the TGA experiments, it is assumed to be related to the melting reaction. Below the melting temperature, LPDE is in solid form and its heat capacity was fitted by a second-order polynomial, $c_{LDPE_{solid}} = 15773 - 105.7T + 0.2T^2$ J kg^{-1} K^{-1}. Above this temperature, LDPE is in molten phase and its heat capacity is $c = 1228.3 + 3.4T$ J kg^{-1} K^{-1}. The heat of melting was determined by integrating in time the difference between the experimental heat flow and the baseline one (green curve in Fig. 4.1), this latter being computed by assuming that no melting reactions occurred (see Fig. 4.1). The kinetic parameters that describe the melting reaction of LDPE are obtained from inverse modeling of DSC at this given heating rate and the quality of the fit is illustrated by the red curve in Fig. 4.1.

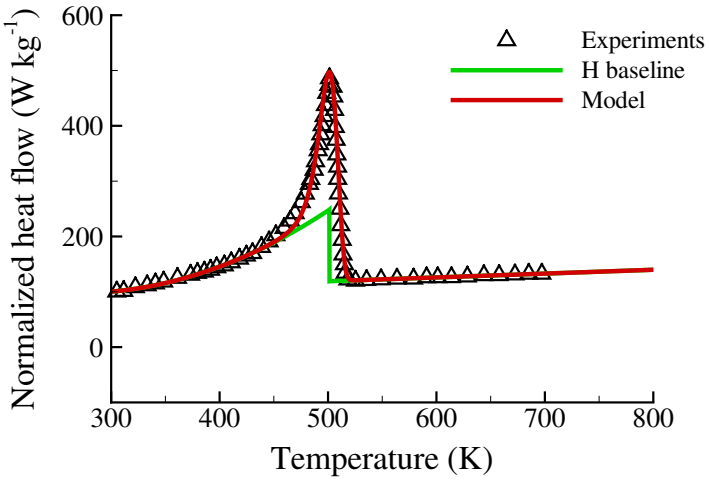

Figure 4.1: Experimental and simulated DSC of LDPE at a heating rate of 5 K min^{-1}.

The TGA of LDPE at heating rates of 1, 2, 5, 10 and 20 K min^{-1} are plotted in Fig. 4.2. Figure 4.2 indicates that the pyrolysis of LDPE can be represented by a single first-order reaction, which peaks between 680 K and 730 K. In addition, almost no condensed-phase residue remains at the end of each test ($\theta \approx 0.35$ wt%). The kinetic parameters were then obtained from an inverse modeling of the TGA at 2 and 10 K min^{-1}. Both ML and MLR were targeted during the optimization process.

The resulting LDPE reaction mechanism is provided in Table 4.2, and the corresponding optimized parameters are listed in Table 4.3. Reaction (1) describes the LDPE melting, observed experimentally in DSC experiments, whereas reaction (2) describes the LDPE pyrolysis (gasification), observed in TGA experiments. Number subscripts represent decomposition reactions. The optimized activation energy for LDPE gasification reaction is consistent with the upper range reported in the literature [108]. The value for the enthalpy of LDPE melting is slightly lower than the range reported in the literature ($-100 < H_1 < -50$ J g^{-1}) [109, 110]. However, it should be pointed out that these latter values were not determined from a heat baseline such as done in the present work. The enthalpy of pyrolysis (H_2) is determined and discussed in the next section. Figures 4.1 and 4.2 show that the computed normalized heat flow, ML and MLR reproduce well the experimental data, not only for the heating rates used for the optimization (2 and 10 K min^{-1} for TGA experiments) but also for the other heating values, demonstrating the robustness of the mechanism.

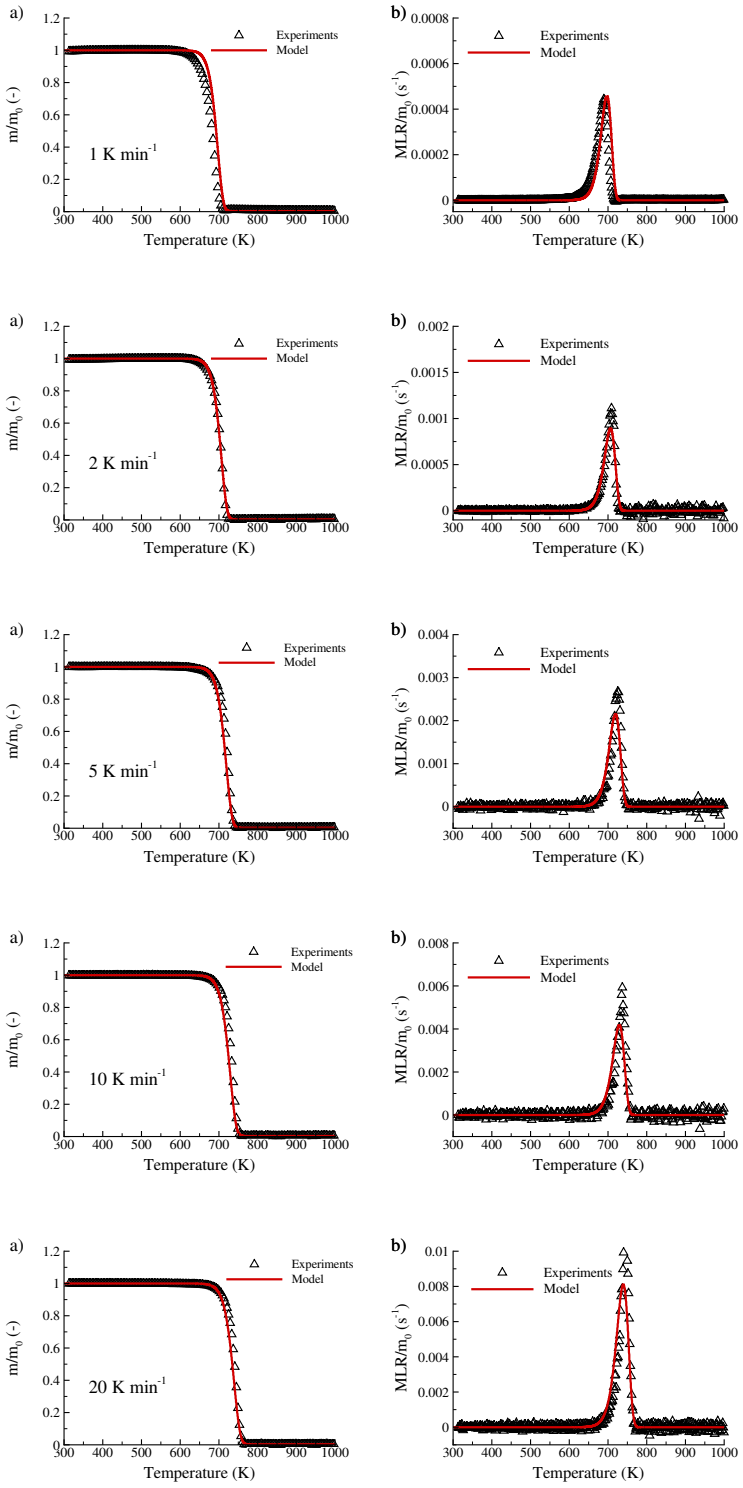

Figure 4.2: Experimental and simulated TGA of LDPE at the heating rates of 1, 2, 5, 10 and 20 K min^{-1}. (a) Normalized mass loss. (b) Normalized mass loss rate.

	Reaction
(1)	LDPE_solid $\rightarrow \theta_1$LDPE_melt
(2)	LDPE_melt $\rightarrow \theta_2$LDPE_res + $(1-\theta_2)$LDPE_gas

Table 4.2: Reaction mechanism of LDPE thermal decomposition.

Reaction	A(s^{-1})	E (J mol^{-1})	θ	H (J kg^{-1})
(1)	2.4×10^{48}	372000	1	-32700
(2)	8.4×10^{18}	291500	0.0035	-1140000

Table 4.3: Kinetic and thermodynamic parameters describing LDPE thermal decomposition.

4.3.2 Cone calorimeter

The experimental heat release rates (HRR) obtained from cone calorimeter experiments at different cone heat fluxes are shown in Fig. 4.3. When the cone radiative flux is increased, the time to ignition and burning duration decrease while the peak of HRR increases. The time evolution of the HHR is similar for the four cases: ignition is followed by a rapid increase in HRR until a short plateau or peak. Then, the HRR decreases until extinction. The final residual mass represents in average 3.5 % of the initial mass of the sample.

Assuming that the instantaneous heat of combustion is constant [60], the HRR has been obtained numerically by multiplying the MLR by the heat of combustion of polyethylene $\Delta H_{c,PE} = 43.28$ kJ g^{-1} [111]. Four apparent properties were optimized by the inverse modelling of cone calorimetry experiments: the thermal conductivity (and its linear evolution with temperature) and radiation absorptivity, α, of LDPE_solid and LDPE_melt, and the enthalpy of the pyrolysis reaction (H_2). These parameters were obtained by optimizing the HRR for $\dot{q}''_{cone} = 25$ and 60 kW m^{-2}. The flame heat flux has also been numerically fitted in this step, targeting the HRR in the optimization process for the same cone heat fluxes as those used for the parameter fitting. Increments of 1 kW m^{-2} were applied to the flame heat flux until best agreement with the experimental data was achieved in the optimization algorithm. The flame heat flux for LDPE was found to be $\dot{q}''_{cone} = 12$ kW m^{-2}, which is consistent with values obtained by [48] for similar polymers (PMMA and HDPE) when using the same methodology.

Table 4.4 shows the final optimized parameters. The thermal conductivity of LDPE_solid at ambient temperature is within the range of the values reported in the literature (approximately 0.3 W m^{-1} K^{-1} [93]). No reference value was found in the literature for thermal conductivity of LDPE_solid. The absorption coefficients of solid and melt LDPE were also in the range of the average values of thermoplastics [52]. The value of the heat of pyrolysis (shown in Table 4.3) is also in the range of the heats of decomposition of common plastics and polymers [112]. Figure 4.3 shows that the

model represents the HRR accurately, not only for the targeted cases of incident heat flux used for the optimization ($\dot{q}''_{\text{cone}} = 25$ and 60 kW m^{-2}) but for the two other cases, showing the robustness of the model and its calibrated parameters. The peak and total HHRs are within 15 % of experimental results in all observed cases. The numerically determined ignition time also represents well the experimental data qualitatively, as shown in Fig. 4.4.

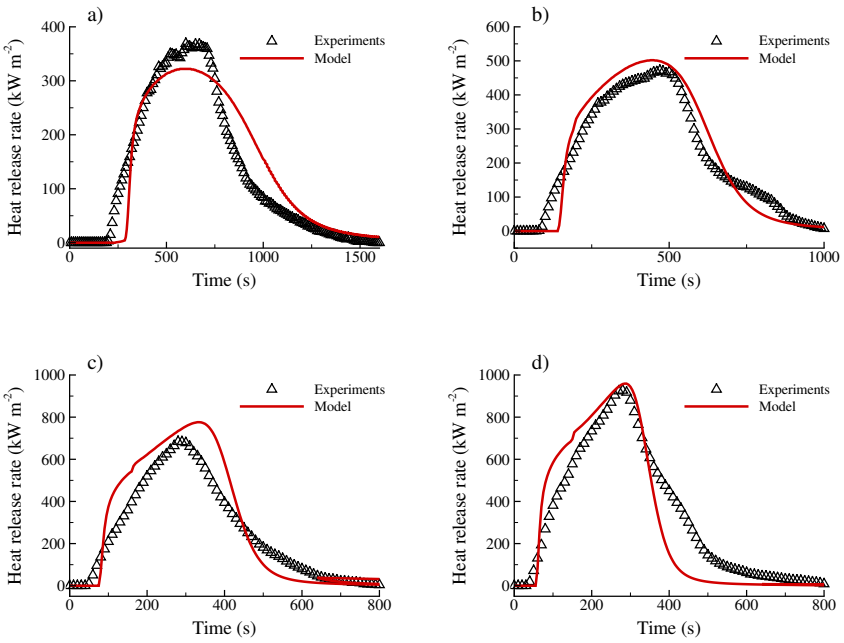

Figure 4.3: Experimental and simulated heat release rate history of LDPE at the at different radiant heat intensities. (a) $\dot{q}''_{\text{cone}} = 25$ kW m^{-2}. (b) $\dot{q}''_{\text{cone}} = 35$ kW m^{-2}. (c) $\dot{q}''_{\text{cone}} = 50$ kW m^{-2}. (d) $\dot{q}''_{\text{cone}} = 60$ kW m^{-2}.

Component	k(W m^{-1} K^{-1})	α (m^{-1})
LDPE_solid	$0.31 - 9 \times 10^{-5}$ T	1.52
LDPE_melt	$0.2 - 8.8 \times 10^{-5}$ T	1.13

Table 4.4: Heat transfer parameters describing LDPE thermal decomposition.

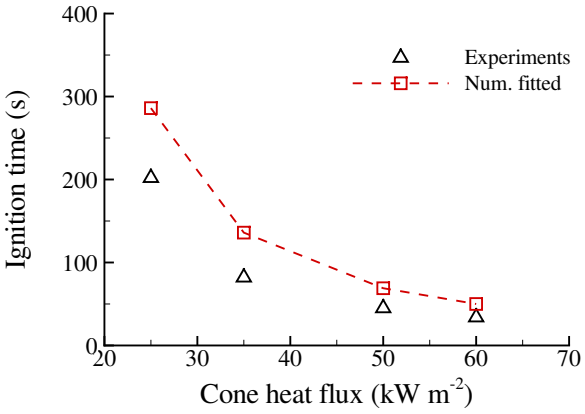

Figure 4.4: Experimental and numerically calculated time to ignition for the four observed cases of cone heat flux.

4.4 Conclusions

A semi-empirical model involving a semi-global mechanism based on first- and second-order reaction and a detailed description of the heat transfer mechanism have been exercised to characterize the thermal decomposition of LDPE. The kinetic, thermodynamic ad thermal parameters are obtained from inverse modelling of TGA, DCS and cone colorimeter experiments over a wide range of heating rate and cone radiative fluxes, respectively, using the Shuffled Complex Evolution optimization algorithm. The semi-global reaction mechanism for the degradation of LDPE consists of two consecutive first-order reactions for the melting and gasification. The derived parameters as well as the flame heat flux in cone calorimeter experiments are in line with those measured and reported in the literature. The final model and fitted parameters are shown to predict the time to ignition and the time evolution of the heat release rate of experiments within the engineering accuracy.

5 Modeling of the thermal decomposition of an intumescent flame retardant system in a LDPE matrix

Sommaire

A practical solution to mitigate the high fire risks attributed to polymers is the incorporation of fire retardants. These additives typically work by lowering the material flammability and/or slowing down the flame spread. One of the most promising solutions to improve fire resistance of polymeric materials are intumescent flame retardants (IFR) [113]. Their fire mitigation mechanism is based on the formation of a swollen char that acts as a thermal shield towards external heat sources [11, 12, 13]. Their efficiency in reducing flammability was well documented [65]. In this chapter, the intumescent flame retardant additive studied is a combination of ammonium polyphosphate (APP), which works as an acid source and blowing agent, and pentaerythritol (PER) as the charring agent. The reaction process of the APP/PER mixture was intensively studied in the 80s and 90s [66, 67, 68, 114]. It was shown that the addition of 15 wt% of APP/PER to a matrix of polypropylene achieves a Limiting Oxygen Index of 30 %, which is the requirement for polymer commercial applications [67]. The addition of APP, PER and melamine was found to improve polypropylene's flammability in terms of heat release rate, limiting oxygen concentration and smoke release, while retaining its mechanical properties [115].

The multi-step pyrolysis code and inverse modelling methodology for input parameter determination, thoroughly discussed in Chapter 3, to develop a pyrolysis model for polymers, has been extended to multi-component blends and, more specifically, to

flame retardant additives in a polymeric matrix by Ding and colleagues [78]. An intumescent flame retardant system of Poly(lactic acid), melamine and APP with different concentrations was considered for building a semi-global reaction mechanism consisting of first and second-order reactions. Inverse numerical modelling of TGA, DSC and microscale combustion calorimetry (MCC) were used to determine the relevant kinetics and thermodynamics parameters. Following the work of Ding and colleagues, cone calorimeter experiments over the same IFR system were used to measure the mass loss rate (MLR), back surface temperature and shape profile of the pyrolyzing sample in an anaerobic environment [80]. Their modeling framework Thermakin2Ds [45] was used for inverse analysis of the experimental data, allowing to determine the relationship between thermal transport properties and material composition. The controlling of the model apparent properties allowed to simulate the effects of intumescence on the reduction of the material heat release rate upon gasification. This same methodology was also applied to build a semi-global reaction mechanism and determine the kinetics and thermodynamics parameters of chopped glass fiber reinforced polyamide (PA66) blended with a condensed-phase-active flame retardant red phosphorus [82]. This reaction mechanism was considered for the inverse modelling of cone calorimetry data in view to characterize heat and mass transport parameters [116]. The final pyrolysis model was found to predict accurately the evolution of the heat release rate in the gasification of disk-shaped samples subjected to well-defined radiant heating in an anaerobic environment for different blend compositions.

In this work, a semi-global reaction mechanism for the thermal decomposition of an intumescent flame retardant system is built based on TGA and DSC experiments. The inverse modeling technique used in this work is applied again to determine the kinetics and thermodynamics of thermal decomposition of the multi-component mixture. Cone calorimetry data in a non-inert atmosphere is then conducted, and the thermal transport properties are determined. The IFR system chosen in this chapter is low-density polyethylene (LDPE) blended with ammonium polyphosphate (APP), and pentaerythritol (PER). The experimental and numerical procedures follow the guidelines described in Chapters 3 and 4 and will be not mentioned in this chapter.

5.1 Materials

Three neat materials are considered in this chapter: low-density polyethylene (LDPE), ammonium polyphosphate (APP) and pentaerythritol (PER), whose formulation names, blends and compositions are provided in Table 5.1. LDPE was supplied by Sabic (Netherlands) in the commercial grade Sabic®LDPE 2602X1 00900. APP is the commercial grade of Clariant (Germany) with the brand name Exolit AP422. PER was supplied by Aldrich.

Neat APP, PER and AP, that refers to APP/PER fire retardant with the ratio 3:1 (wt/wt) hereafter, were tested in the form of powder. The ratio of $APP/PER = 3$ was selected as it can lead to the formation of an intumescent maximum [117].

APP/PER samples were prepared by conventional powder mixing. LDPE was blended

with 10 wt% of AP in a twinscrew extruder. Compounding was performed using HAAKE Rheomix OS PTW 16 twin-screw extruder. The extruder is a co-rotating intermeshing twin screw with a barrel length of 400 mm and a screw diameter of 16 mm ($L/D = 25$) with 10 zones. LDPE and AP were incorporated using two gravimetric side feeders into the extruder. The polymer flow rate is fixed to extrude about 500 g/h with a screw speed of 300 rpm. For the TGA analysis of the LDPE90AP10 samples (see Table 5.1), small pieces of material were cryogenically grinded into powder and about 7 mg of powder was put in alumina pan

Formulation name	LDPE (wt. %)	APP (wt. %)	PER (wt. %)
Pure LDPE	100	0	0
Pure APP	0	100	0
Pure PER	0	0	100
AP	0	75	25
LDPE90AP10	90	7.5	2.5

Table 5.1: Material and blend compositions.

5.2 STA Results

5.2.1 Methodology

The methodology to develop a semi-global kinetic mechanism for the thermal decomposition of the intumescent flame retardant system is described here. The first step consisted in developing a kinetic mechanism for each of the neat materials separately (APP, and PER, such as previously performed for LDPE). In a second step, a semi-global reaction mechanism for the flame retardant blend AP was developed. During this stage, strong interactions between the neat components, i.e. APP and PER, were observed and a physically-based semi-global mechanism was built by relating the chemical reactions, deduced from analysis of the mass loss rate from TGA, to the main steps of the mechanism of intumescence [13]. Finally, the individual mechanisms of LPDE and AP were combined to generate the mechanism for the LDPE/APP/PER blend. This mechanism was validated in a 90%LDPE/10% AP system and was slightly updated to account for the possible interactions between the LDPE and the APP/PER additive.

5.2.2 TGA of neat materials

The mean experimental TGA data of the neat APP and PER are shown in 5.1 and 5.2, respectively. The TGA of LDPE, which is also used in this chapter, was shown and analysed in Fig. 4.2.

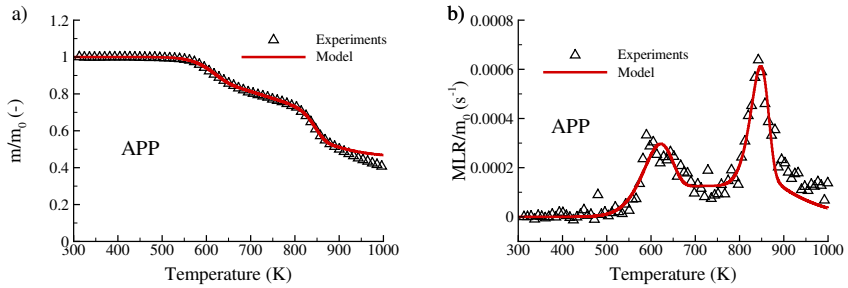

Figure 5.1: Experimental and simulated TGA of APP at 10 K min^{-1}. (a) Normalized mass loss. (b) Normalized mass loss rate.

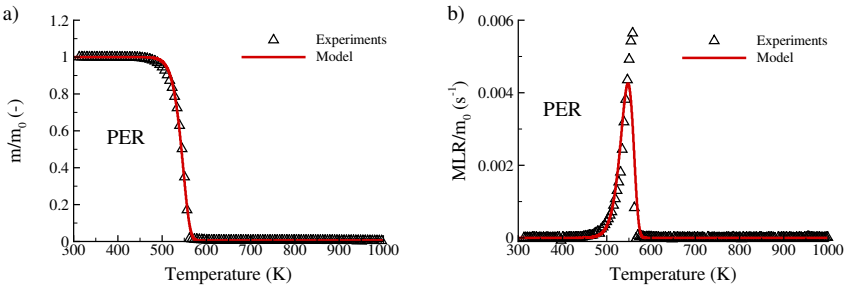

Figure 5.2: Experimental and simulated TGA of PER at 10 K min^{-1}. (a) Normalized mass loss. (b) Normalized mass loss rate.

Figure 5.1 suggests that the decomposition of APP is characterized by three distinct first-order reactions at $T \approx 600, 700$ and 850 K whereas the solid residue at the end of the test is estimated to be around 40%. The second reaction peak at $T \approx 700$ K is less distinguishable than the two others as the corresponding reaction is characterized by a low reaction rate. However, it was found crucial to account for it to match experimental data at this region. A similar analysis of Fig. 5.2 indicates that the degradation of PER is represented by a single first-order reaction at $T \approx 550$ K. The reaction models and the optimized kinetic parameters for the neat APP and PER are given in Table 5.2 and Table 5.3, respectively, and the quality of the fits is illustrated in Figs. 5.1 and 5.2. Both the mass and MLR histories were targeted in the optimization process. Reactions (1) and (2), not shown in these tables, correspond to the decomposition of neat LDPE, previously presented in Tables. 4.2 and 4.3.

The TGA of APP reported by Ding et al. [78] is qualitatively consistent with that reported in this study with the three reactions occurring at similar temperatures. However, some differences are observed, in particular, concerning the magnitude of the third reaction peak which was found higher in the experiments of [78]. This explains that different kinetic parameters were obtained. On the other hand, TGA of PER was reported in Ref. [118] with a similar behaviour as observed in the present

Mechanism	Reaction
APP MECH	(3) APP $\rightarrow \theta_3$APP_res1 + $(1-\theta_3)$APP_gas
	(4) APP_res1 $\rightarrow \theta_4$APP_res2 + $(1-\theta_4)$APP_res1_gas
	(5) APP_res2 $\rightarrow \theta_5$APP_res3 + $(1-\theta_5)$APP_res2_gas
PER MECH	(6) PER $\rightarrow \theta_6$PER_res + $(1-\theta_6)$PER_gas

Table 5.2: Reaction models of the decomposition of the neat materials.

Reaction	A(s^{-1})	E (J mol^{-1})	θ
(3)	1.40×10^5	88200	0.87
(4)	0.05	23800	0.76
(5)	1.71×10^{15}	280400	0.68
(6)	7.30×10^{13}	165900	0.006

Table 5.3: Kinetic parameters describing the neat materials thermal decompositions.

study. However, no kinetic model was proposed in this study.

5.2.3 TGA of the intumescent blend AP

A first attempt to simulate the decomposition of the intumescent blend AP was made by assuming that APP and PER do not interact. In this case, the mass of the sample is computed as a mass weighted sum of APP and PER and the individual mass loss rates of APP and PER are obtained from the reaction models given in Table 5.2. Figure 5.3 shows that this approach produces large discrepancies between simulated and experimental results, indicating that strong interactions between APP and PER occur throughout the process. This behaviour is consistent with previous experimental observations [66]. A semi-global reaction model is designed to account for these interactions by relating the reaction events in the MLR to the mechanism of intumescence.

The TGA of AP is shown in Fig. 5.4(a), for five sets of heating rates of 0.25, 1, 2, 10 and 20 K min^{-1}. A systematic behavior is observed for the different heating rates and the MLR for an heating rate of 20 K min^{-1} is selected for analysis (see Fig. 5.4(b)). Figure 5.4(b) shows that five apparent reactions can be clearly identified. Similar observations were made by [70] in TGA at an heating rate of 10 K min^{-1}. These different reactions can be related to the three-step in the mechanism of intumescence [66, 68, 119, 120, 13]:

1. The acidic species (APP and its degradation products into orthophosphates and phosphoric acids) reacts with the char forming agent (PER) to produce ester mixtures ($T < 550$ K). At the end of this process, the carbonisation process takes place via a free radical process. This sequence of chemical events is modeled by a single second-order reaction, reaction I, between APP and PER leading to formation of the ester mixtures AP_1 (see Table 5.4).

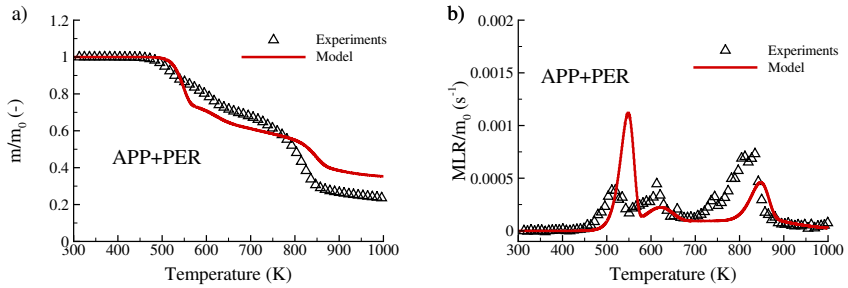

Figure 5.3: Experimental and calculated TGA of AP, based on the reactions 3-6 of Table 5.2 at 10 K min^{-1}. (a) Normalized mass loss. (b) Normalized mass loss rate.

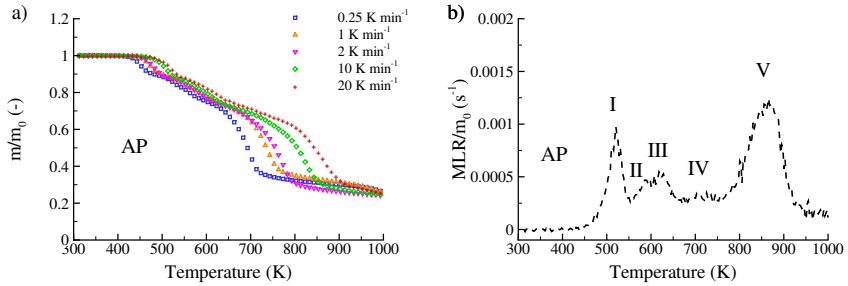

Figure 5.4: TGA of AP. (a) Normalized mass loss at 0.25, 1, 2, 10 and 20 K min^{-1}. (b) Normalized mass loss rate at at 20 Kmin^{-1}.

2. The blowing agent decomposes to yield gaseous products (i.e. ammonia evolved from the decomposition of APP), forming the char to swell (550 < T < 620 K). This sequence of chemical events is modelled by a second-order reaction, reaction II, and a first-order reaction, reaction III (see Table 5.4).

3. The intumescent material decomposes and loses its foamed character (T > 700 K). Concurrently, the heat conductivity of the char decreases with the high temperatures, enhancing the insulation of the substrate [64]. This sequence of chemical events is modelled by reaction IV (see Table 5.4).

Finally, a strong vaporization of the remaining material (reaction peak V) is observed at 750 < T < 850 K, which can be assigned to the degradation of phospho-carbonaceous species and to the subsequent sublimation of phosphorus oxide [120]. A peak at similar temperature is observed in the TGA of neat APP (see Fig. 5.1) and, accordingly, this reaction was attributed to the final decomposition of the remaining APP and its decomposition products (see Table 5.4).

Most of the information on the APP/PER products and their physical characteristics discussed previously come from visual observations. However, the information on the

morphology of the foam and the thermal conductivity of the system were deduced from direct measurements, involving X-ray computed tomography and Hot Disk thermal constants analyzer, respectively, in a polyurethane matrix filled either by 30 wt.% of APP or by a combination of 28 wt.% of APP and 2 wt.% of nano-magnesium oxide [64].

Mechanism	Reaction
AP MECH	(I) α_IAPP + PER $\rightarrow \theta_I$AP$_1$ + $(1-\theta_I)$AP_gas
	(II) α_{II}APP + AP$_1$ $\rightarrow \theta_{II}$INTUM + $(1-\theta_{II})$INTUM_gas
	(III) INTUM $\rightarrow \theta_{III}$INTUM2 + $(1-\theta_{III})$INTUM2_gas
	(IV) INTUM2 $\rightarrow \theta_{IV}$INTUM2_res + $(1-\theta_{IV})$INTUM2_res_gas
	(V) APP $\rightarrow \theta_V$APP_res + $(1-\theta_V)$APP_res_gas

Table 5.4: Reaction model of AP.

The terms INTUM and INTUM2 denote the intumescent material, and they are treated in the model as single, uniform components, as described in the item 2. It is also important to note that the term APP, in reactions I, II and V may not refer to as the exact same component. As discussed in the item 1, APP decomposes into ammonia, orthoposphates and phosphoric acids [13] and it has been assumed that this decomposition is infinitely fast throughout the overall process and plays little effect in the mass loss of the system. A consequence is that APP can be treated as the same component in the semi-global reaction model. All gaseous products nominations are theoretical, and they likely consist of a mixture of degradation products, such as water, ammonia and other boiling products [66].

In order to inverse-model the AP degradation, the optimization procedure was performed from the ML and the MLR at 1 and 10 K/min^{-1} and the kinetic parameters are listed in Table. 5.5. The accuracy and the robustness of the AP MECH reaction model are illustrated in Figs. 5.5 which shows that both experimental ML and MLR are well reproduced at all the heating rates. The assumption of thermally-thin sample may become questionable at a heating rate of 20 K min^{-1} which may explain the larger discrepancies observed for this specific rate.

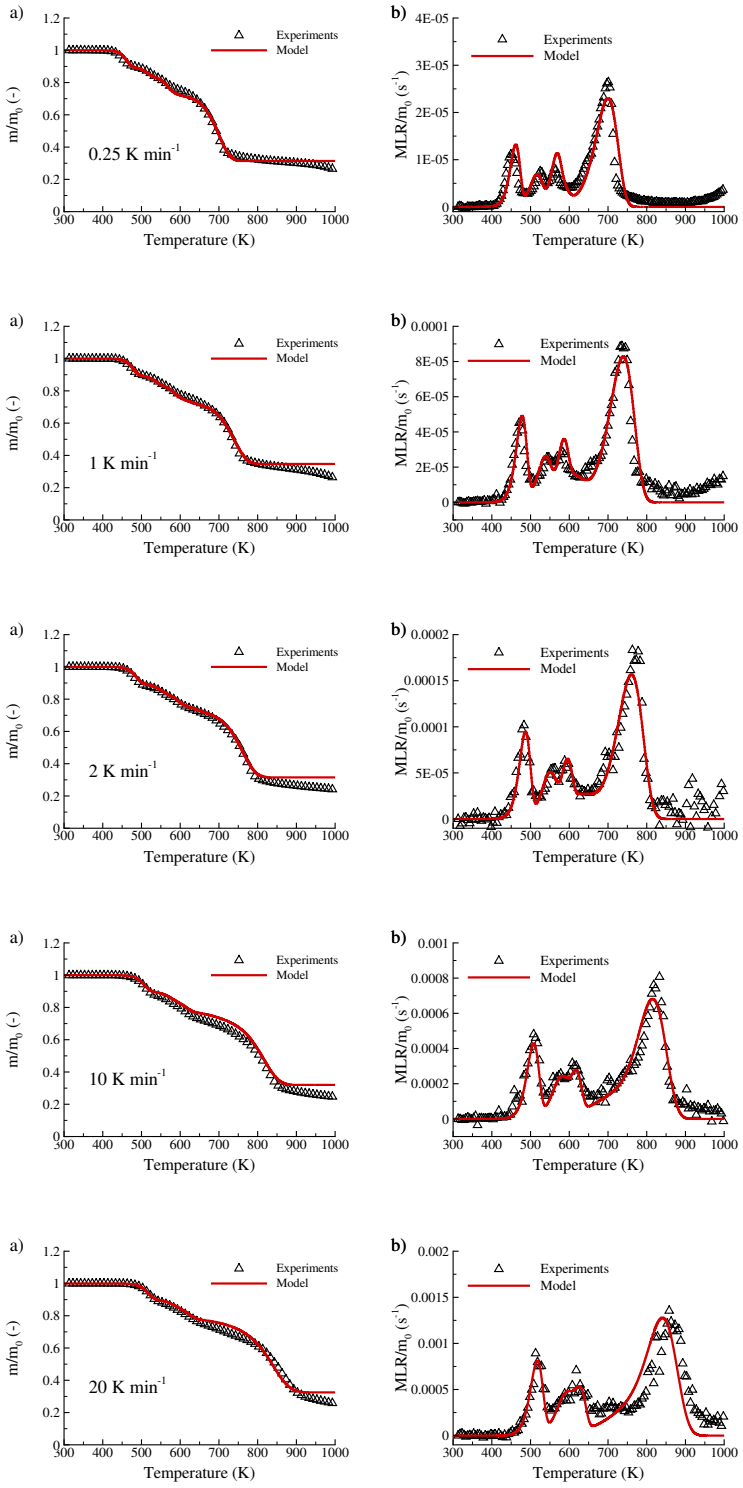

Figure 5.5: Experimental and simulated TGA of AP, using AP MECH, at the heating rates of 0.25, 1, 2, 10 and 20 K min^{-1}. (a) Normalized mass. (b) Normalized mass loss rate.

Reaction	A(s^{-1})	E (J mol^{-1})	θ	α
(I)	3.5×10^{15}	146300	1.13	0.54
(II)	2.7×10^{13}	143000	1.02	0.25
(III)	2.8×10^{14}	194100	0.79	-
(IV)	2.2×10^{3}	77000	0.78	-
(V)	3.5×10^{6}	139200	0.25	-

Table 5.5: Kinetic parameters describing AP thermal decompositions.

5.2.4 TGA of the intumescent system LDPE/AP

Comparisons between the experimental TGA of LDPE90AP10 and predictions using the decomposition (gasification only) reaction model of neat LDPE (reaction 2 from Table 4.2) and the isolated intumescent system AP (reactions I-V from Table 5.4) are shown in Fig. 5.6 for a heating rate of 10 K min^{-1}. The simulation predicts the experimental data reasonably well. However, two main discrepancies are observed:

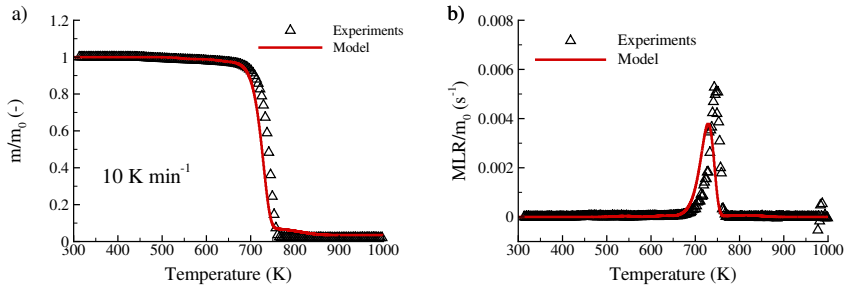

Figure 5.6: Experimental and calculated TGA of LDPE90AP10, using reactions 2 and I-V (see Tables 4.2 and 5.4) at 10 K min^{-1}. (a) Normalized mass loss. (b) Normalized mass loss rate.

1. The predicted decomposition of LDPE is shifted to sightly lower temperatures as compared to the experiments, as shown in Fig. 5.6(a). Moreover, the associated peak of MLR is lower as compared to the experiments, as shown in Fig. 5.6(b).

2. The final decomposition of APP (reaction V, depicted in Table. 5.4), which occurs at $T = 750 - 800$ K, is not observed in the experiments.

Similar discrepancies between simulations and experiments are observed for the other heating rates (not shown). This indicates that LDPE and APP/PER interact sightly. This assumption is supported by the fact that the experimental mass loss of LDPE90AP10 and that computed by neglecting the interactions as the mass-weighted sum of the experimental mass losses of neat LDPE and AP ($m(t) = 0.9 \times m^{exp}_{LDPE}(t) + 0.1 \times m^{exp}_{AP}(t)$) exhibits similar discrepancies (see Fig. 5.7). We assume that these interactions have a physical origin rather than a chemical one and the kinetic parameters

Reaction	A(s^{-1})	E (J mol^{-1})	θ	α
(2)	$\mathbf{1.1 \times 10^{22}}$	**339600**	0.0035	-
(I)	3.5×10^{15}	146300	1.13	0.54
(II)	2.7×10^{13}	143000	1.02	0.25
(III)	2.8×10^{14}	194100	0.79	-
(IV)	2.2×10^{3}	77000	0.78	-
(V)	$\mathbf{3.5 \times 10^{7}}$	139200	0.25	-

Table 5.6: Kinetic parameters describing LDPE-AP thermal decomposition.

of two decomposition reactions, namely reaction 1 and V, are modified to account for this. In particular, reaction V is assumed to occur more rapidly when AP is added to the LDPE matrix. The updated set of kinetic parameters are provided in Table 5.6 with the modified parameters evidenced in bold characters. The corresponding model predictions are compared with experimental data in Fig. 5.8, exhibiting a satisfactory overall agreement for all the heating rates.

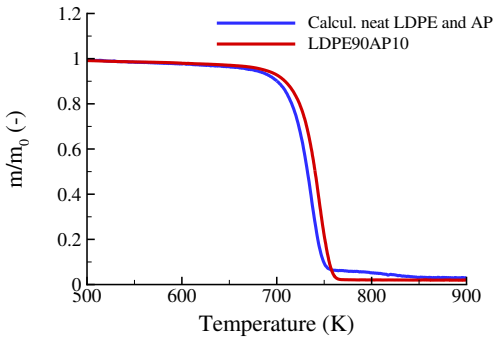

Figure 5.7: Experimental mass loss of the LDPE90AP10 system (red curve) and mass loss calculated as the mass-weighted sum of the experimental mass losses of neat LDPE and AP (blue curve) at 10 K min^{-1}.

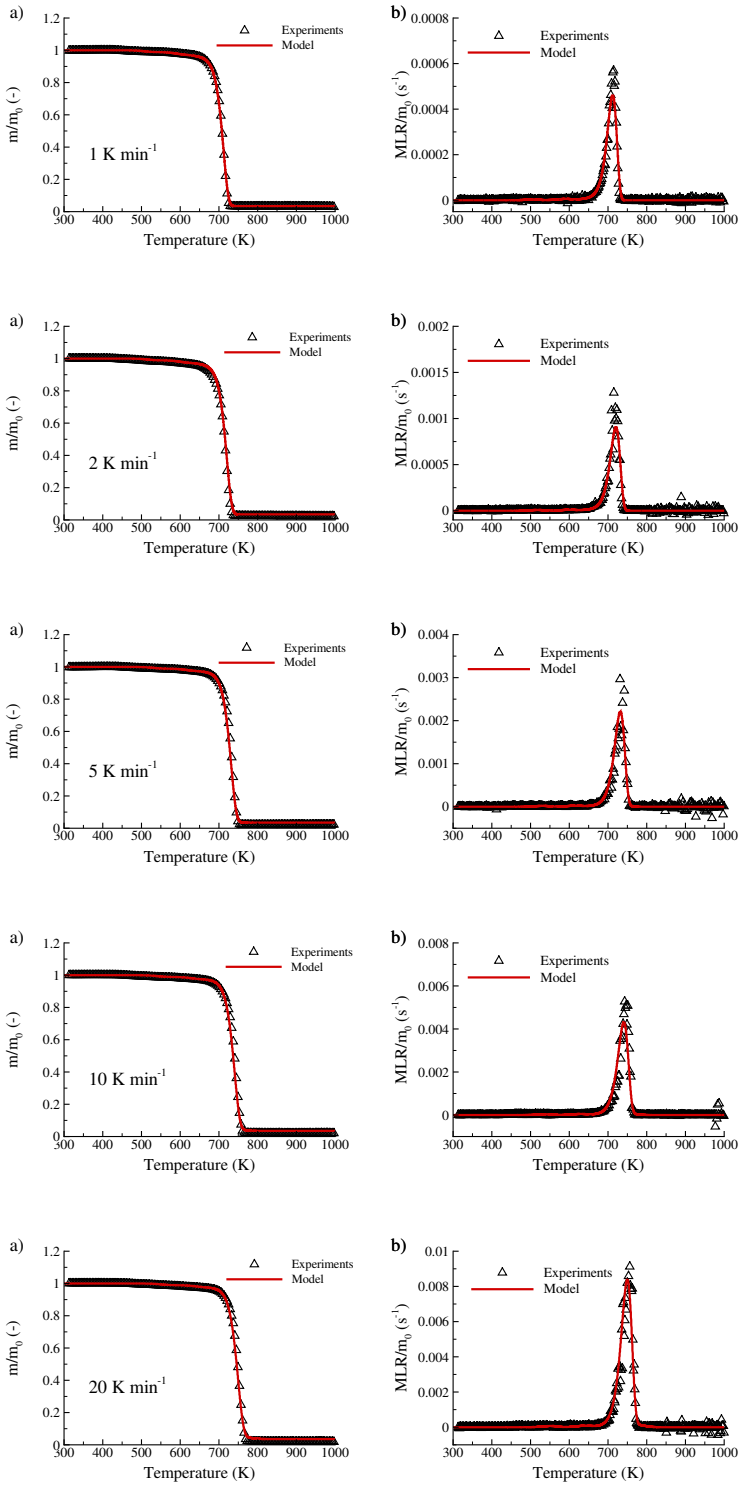

Figure 5.8: Experimental and simulated TGA of LDPE90AP10 at a heating rates of 1, 2, 5, 10 and 20 K min^{-1}. (a) Normalized mass loss. (b) Normalized mass loss rate.

5.3 Cone calorimeter results

The experimental heat release rate (HRR) histories obtained from cone calorimeter experiments for the intumescent flame retardant system LDPE90AP10 and their comparison with pure LDPE are shown in Fig. 5.9 for three different cone heat fluxes. The flame retardant additive is shown to improve the flammability of the polymer. The addition of 10 % of AP significantly reduces the peak release rate (pHRR) of the burning LDPE down to 24, 26 and 37 % reduction for the cone heat fluxes of 35, 50 and 60 kW m^{-2}, respectively. The behavior of the HRR of LDPE90AP10, and its comparison with that of pure LDPE, remain similar for the three observed cone heat fluxes. Ignition is followed by a rapid increase in HRR, both similar in time and magnitude with those observed from pure LDPE. After increase of HRR, a longer plateau is observed, though lower in magnitude, until decrease in burning until extinction.

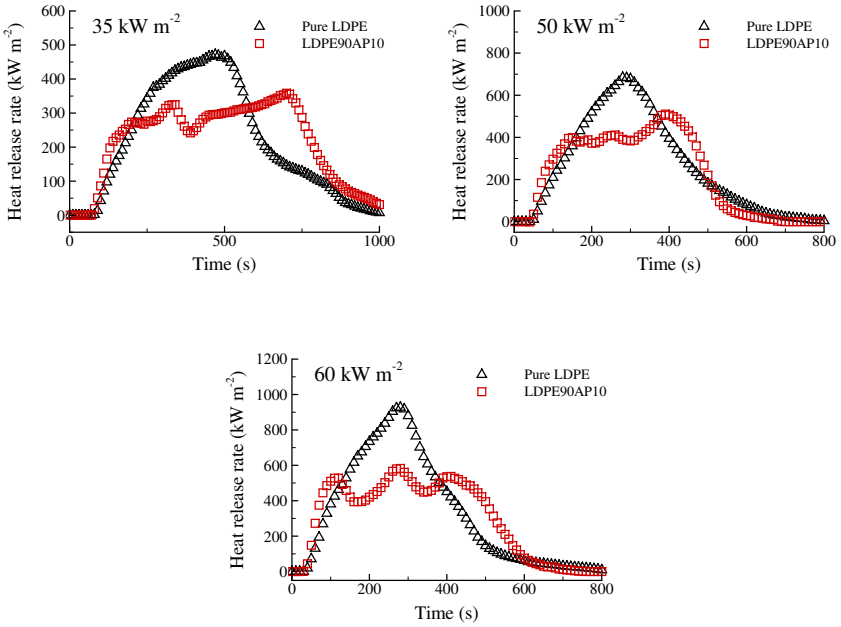

Figure 5.9: Experimental heat release rate history of pure LDPE and LDPE90AP10 at three different radiant heat intensities.

Inverse modeling of cone calorimetry data of LDPE90AP10 requires the previously developed reaction model from STA experiments, globally summarized in Table 5.7 and their kinetics properties (see Tables 4.3 and 5.6). The gaseous products have been removed from the reaction mechanism in Table 5.7 for simplification purposes. The enthalpy of AP decomposition reactions have not been determined in this work. However, it has been assessed by our numerical model that they do not significantly contribute to the overall enthalpy of the system, as these species masses are minor, compared to the LDPE. An estimated value of $H = -800000$ J kg^{-1} has been given

Mechanism	Reaction	H (J kg^{-1})
LDPE MECH	(1) LDPE_solid → θ_1LDPE_melt	-32700
	(2) LDPE_melt → θ_2LDPE_res	-1140000
AP MECH	(I) α_IAPP + PER → θ_IAP$_1$	-800000
	(II) α_{II}APP + AP$_1$ → θ_{II}INTUM	-800000
	(III) INTUM → θ_{III}INTUM2	-800000
	(IV) INTUM2 → θ_{IV}INTUM2_res	-800000
	(V) APP → θ_VAPP_res	-800000

Table 5.7: Reaction model of LDPE90AP10.

to this set of reactions, and multiplying or dividing these values by 30% was found to provide minor changes on the results. Values measured by DSC for the heat of decomposition of pure APP were found to be within this range [78]. The enthalpy of decomposition reactions are also shown in Table 5.7.

An image of the LDPE90AP10 sample residue after combustion in the cone calorimeter is shown in Fig. 5.10. An expanded carbonaceous char has been formed, which acts as a heat barrier. The internal structure is foamy, with random voids of irregular volumes and the cohesion of the structure is relatively high. The key to the modeling of the burning IFR system is the determination of apparent properties associated with the swollen char: density, thermal conductivity and radiation absorptivity [80]. These properties can control the material swelling effect, which slows down burning as characterized in section 5.2.3.

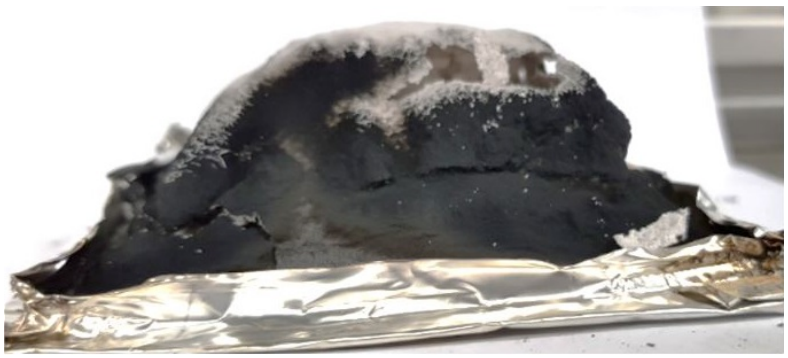

Figure 5.10: LDPE-AP sample after combustion.

The remaining condensed-phase properties used in the pyrolysis model of LDPE90AP10 are summarized in Table 5.8. The targeted HRR values for inverse modeling were 35 and 60 kW m^{-2}, and the optimized parameters are evidenced in bold characters.

The densities of APP and PER were taken from literature [121, 122], and the density of AP$_1$ is estimated to be the weighted average of its original products. The density of the residue APP_res is given as the same value as its original component, assuming

Component	ρ (kg m^{-3})	k (W m^{-1} K^{-1})	α (m^{-1})
LDPE_solid	948.2	$0.31 - 9 \times 10^{-5}$ T	1.52
LDPE_melt	$948.2 - 0.94 \times (T - T_\infty)$	$0.2 - 8.8 \times 10^{-5}$ T	1.13
LDPE_res	948.2	0.2	1.5
APP	1900	0.25	**1.12**
PER	1390	0.25	**1.12**
AP_1	1773	0.25	**1.12**
INTUM	**28**	**0.19**	**1.52**
INTUM2	**4**	**0.2**	**1.44**
INTUM_res	**396**	**0.2**	**9.6**
APP_res	1900	**0.15**	**8.2**

Table 5.8: Intumescence parameters describing LDPE-AP thermal decomposition.

that pure APP degradation products do not swell. The apparent densities of the intumescent components INTUM, INTUM2 and INTUM_res were significantly decreased in order to model the material swelling. The resulting evolution of the material deformation under an incident heat flux of 35 kW m^{-2} is shown in Fig. 5.11(a). The materials swells when the IFR components decompose to form INTUM and INTUM2 and, then, the foamed character decreases when INTUM_res is formed and LDPE gasifies. Experimental measurements of the condensed-phase deformation for validation of the proposed apparent properties and swelling modeling are not available, and are a main perspective of this work.

The thermal conductivity of APP, PER and AP_1 were given constant, estimated values. They were not mathematically fitted through inverse modeling, as these values were found to not significantly contribute to the overall HRR. The conductivity values of the intumescent components and APP_res were found to be inferior than their original components, as expected from the mechanisms of intumescence [76, 64]. The evolution of the mean thermal conductivity with the mean sample temperature is reported in Fig. 5.11(b). This behavior is qualitatively in accordance to thermal conductivity measurements of another intumescent system (28%APP and 2% nano magnesium oxide in a polyurethane matrix) using the transient plane source method (see Fig. 1.13) [64].

The fitted absorption coefficient values for APP, PER, AP_1, INTUM and INTUM2 are within the range of engineering polymers [52]. The values of the residual components INTUM_res and APP_res were found to be significantly higher. This is expected as the intumescent residues were observed to appear very optically dark and graphite in nature [63, 80].

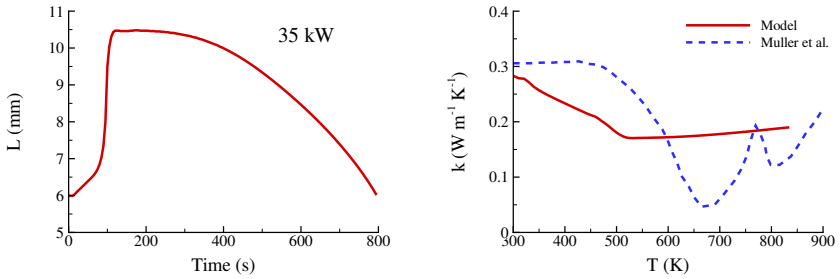

Figure 5.11: Simulated condensed-phase deformation (a) and mean thermal conductivity (b) of LDPE90AP10 at 35 K min^{-1}. Measurements of the heat conductivity of an IFR consisting of 28%APP and 2% nano magnesium oxide in a polyurethane matrix are also shown for comparison purposes.

The final quality of the fit is shown in Fig. 5.12. A good overall qualitative agreement is observed with the experimental data, not only for the targeted optimized values (35 and 60 kW m^{-2}) but for 50 kW m^{-2}, showing robustness of the model at the proposed range of incident heat flux. The total HRR was within 10% of the measured values in cone calorimetry, and the numerically determined ignition time also represents well the experimental data qualitatively, as show in Fig. 5.13.

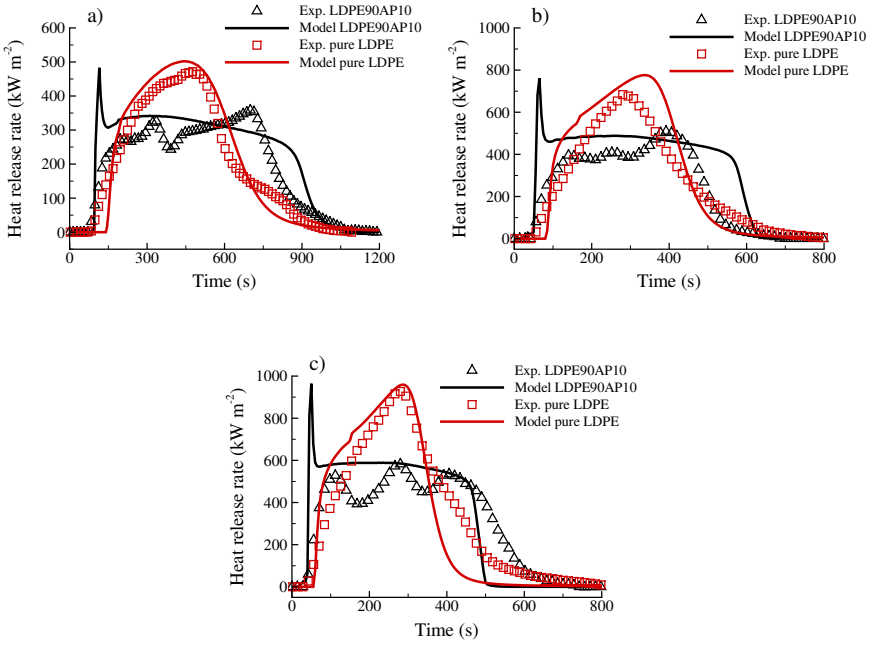

Figure 5.12: Experimental and simulated heat release rate history of pure LDPE and LDPE90AP10 at the at different radiant heat intensities. (a) $\dot{q}''_{\text{cone}}$ = 35 kW m^{-2}. (b) $\dot{q}''_{\text{cone}}$ = 50 kW m^{-2}. (c) $\dot{q}''_{\text{cone}}$ = 60 kW m^{-2}.

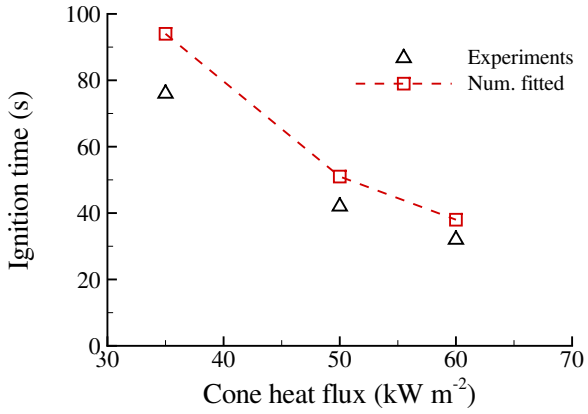

Figure 5.13: Experimental and numerically calculated time to ignition for the three observed cases of cone heat flux.

5.4 Conclusions

This chapter presents the development of a semi-empirical model that describes the decomposition process of an intumescent fire retardant system consisting of ammonium polyphosphate/pentaerythritol in a LDPE matrix according to TGA, DSC and cone calorimeter experiments. Based on TGA experiments over a wide range of heating rates, from 0.25 to 20 K min^{-1}, a semi-global reaction mechanism for the decomposition process of LDPE-APP/PER is built. The methodology relies, on the one hand, on the development of intermediate reaction models for neat materials and, on the other hand, on the knowledge of the intumescent mechanism to account for the interactions between neat species. The reaction mechanism and its determined input parameters were then used for determination of thermal transport properties for modeling cone calorimetry data over a range of incident heat fluxes, from 35 to 60 kW m^{-2}. The model was found to predict that system mass loss and associated heat release rates within engineering accuracy. The resulting semi-global reaction model can serve as a basis to build a pyrolysis model for the LDPE-APP/PER system which, coupled to CFD fire simulators, can be used to predict fire growth, which is a main perspective of this line of work.

The following conclusions can be drawn:

1. Accurate and robust reaction mechanisms for neat LDPE, APP and PER are developed involving one, three and one first-order reactions, respectively.

2. APP and PER interact during the decomposition of the APP/PER fire retardant system and the generation of an accurate reaction model from those of neat APP and PER seems to be difficult.

3. An accurate and robust 5 step physically-based reaction mechanism, combining first and second order reaction, was built for APP/PER with ratio 1:3 (wt/wt).

4. The direct coupling of the 1-step reaction mechanism for LDPE and the 5-step mechanism for APP/PER provides a reasonable prediction of TGA experiments for the 90% LDPE/10% APP/PER fire retardant system, despite noticeable interactions between the LDPE matrix and the APP/PER. These interactions are simply taken into account by slightly updating the kinetic parameters of two reactions.

5. Modeling of the intumescent components apparent properties, in particular density, thermal conductivity and radiative absorption coefficients was shown to be effective for modeling the increased fire performance of the IFR system inside the polymeric matrix.

Conclusion

In the context of fire safety in manned space vehicle, the condensed-phase mechanisms, processes and properties that influence the flammability of polymers in microgravity were numerically and experimentally studied in this PhD thesis. An in-house engineering flame spread model and pyrolysis model were developed with the objective of creating a fully predictive flame spread model over wires in microgravity.

The problem of opposing air-flow flame spread over a solid fuel was first approached with an engineering model for creeping flame spread. The studied configuration was that of LDPE-coated NiCr wires, since unexpected overheating of wires by electrical current overshoots has been identified as a primary cause of fire initiation and growth in space vehicles. The values of flame spread rate were validated against data from DIAMONDS, an experimental rig that studied the flammability of wires, designed for parabolic flights. The coupled heat transfer equations for LDPE and NiCr were solved in the pyrolysis zone and ahead of the pyrolysis front, in conjunction with a simple phase-change based pyrolysis model for LDPE. By considering an Oseen approximation for the flow and infinitely fast chemistry for the gas-phase combustion, the model was show to be reduced to two parameters: the diffusive heat length and the heat conveyed from the flame to a flat surface, this latter depending only on the ambient oxygen concentration. The model was shown to successfully predict the creeping flame spread rate as a function of the oxygen concentration, for different wire geometries and levels of ambient pressure. The heat transfer mechanisms that control flame spread within the wire were then investigated. It was shown that, in the preheat zone adjacent to the flame, the contribution of the flame flux dominate the LDPE heating process whereas the metallic core acts as a heat sink for the thinner LDPE coating and mainly as a heat source for the other wire geometries.

In order to develop a comprehensive flame spread model, a condensed-phase thermal decomposition model was then developed. These developments were performed in collaboration with the group of Serge Bourbigot at UMET Lille. It solved the transient chemical species and energy equations to predict the burning rate of engineering polymers and flame retardants. The materials apparent properties related to heat transfer and decomposition kinetics must be determined as the model input parameters. A strategy for determining these parameters based on inverse modeling of gasification experiments that isolate individual pyrolysis processes was implemented. This strategy was thoroughly described and discussed, based on the Shuffled Complex Evolution, an optimization algorithm used for numerically fitting the target experimental data through inverse modeling. The developed model and optimization algorithm were validated against gasification tests of three commercial polymers retrieved from the literature.

The developed semi-empirical pyrolysis model and strategy were exercised to investigate the flammability of LDPE. The kinetic, thermodynamic and thermal parameters were obtained from inverse modeling of TGA, DSC and cone calorimeter experiments over a wide range of heating rates and cone radiative fluxes. A semi-global reaction mechanism for the degradation of LDPE consisting of two consecutive first-order reactions for the melting and gasification was proposed, and the obtained parameters and flame heat feedback from the burning LDPE were in-line with the values reported in the literature.

The pyrolysis code and parameter determination strategy were finally applied to an intumescent flame retardant system consisting of LDPE blended with ammonium polyphosphate and pentaerythritol on a ratio of 3:1 (wt/wt). A reaction model was developed for the decomposition of the intumescent system based on knowledge of the intumescent mechanism, including first- and second-order reactions that account for physical and chemical interactions between components. The resulting model was shown to simultaneously reproduce TGA and cone calorimetry data for a wide range of heating rates and cone heat fluxes. The main contribution of this work is to propose a reliable methodology based on the mechanistic (physic and chemistry) understanding of the intumescent process to determine a semi-global reaction mechanism with robust kinetic parameters. This approach and methodology could be extended to all forms of decomposition. In addition, this semi-global reaction mechanism was used as a basis to build and validate a pyrolysis model for the LDPE-APP/PER system. The remaining transport parameters, including the apparent densities of the intumescent materials, their thermal conductivity and absorption coefficients, were determined from inverse modelling of cone calorimeter experiments.

The pyrolysis models for LDPE and the intumescent flame retardant system can be coupled with a detailed modelling of the gas phase combustion in order to predict the flame spread over electrical wires at both normal and microgravity with and without flame retardant. This is the main perspective of this study. Additionally, the modelling and calibration approaches, developed during this thesis, can be used to develop pyrolysis models for other materials, including non-charring and charring solids with and without additives.

During my Phd, I have also participated to different works of my research group that have led to two accepted publications: one in *Combustion and Flame* and another in the *The Proceedings of the Combustion Institute*. The first study was a numerical investigation of the effects of oxygen on soot production and emission from electrical wires in microgravity, whereas the second consisted in an experimental work with DIAMONDS in parabolic flights to investigate the effects of flame retardants on extinction limits, spread rate, and smoke emission. These two papers are provided in Annexe.

Bibliography

[1] G Madhavan Nair et al. “Strategic, technological and ethical aspects of establishing colonies on Moon and Mars”. In: *Acta astronautica* 63.11-12 (2008), pp. 1337–1342.

[2] Roland Martinez et al. “ISECG global exploration roadmap: A stepwise approach to deep space exploration”. In: *AIAA SPACE 2013 Conference and Exposition*. 2013, p. 5504.

[3] Space Studies Board et al. *Recapturing a future for space exploration: life and physical sciences research for a new era*. National Academies Press, 2012.

[4] Odor Flammability. “Offgassing, and Compatibility Requirements and Test Procedures for Materials in Environments That Support Combustion (NHB 8060.1 C). Office of Safety and Mission Quality”. In: *National Aeronautics and Space Administration, Washington* (1991).

[5] D Mulville. *Flammability, odor, offgassing, and compatibility requirements and test procedures for materials in environments that support combustion*. Tech. rep. NASA-STD-6001, 1998.

[6] Osamu Fujita. “Solid combustion research in microgravity as a basis of fire safety in space”. In: *Proceedings of the Combustion Institute* 35.3 (2015), pp. 2487–2502.

[7] Shuhei Takahashi et al. “Simplified model for predicting difference between flammability limits of a thin material in normal gravity and microgravity environments”. In: *Proceedings of the Combustion Institute* 35.3 (2015), pp. 2535–2543.

[8] Jean-Marie Citerne et al. “Fire Safety in Space–Investigating flame spread interaction over wires”. In: *Acta Astronautica* 126 (2016), pp. 500–509.

[9] Augustin Guibaud. “Flame spread in microgravity environment: influence of ambient flow conditions”. PhD thesis. Sorbonne université, 2019.

[10] A Guibaud et al. “Broadband modulated absorption/emission technique to probe sooting flames: Implementation, validation, and limitations”. In: *Proceedings of the Combustion Institute* 37.3 (2019), pp. 3959–3966.

[11] JR Anderson et al. “Intumescent Reaction Mechanisms”. In: *Journal of Fire Sciences* 3.3 (1985), pp. 161–194.

[12] Serge Bourbigot et al. “Modeling of Heat Transfer of a Polypropylene-Based Intumescent System during Combustion”. In: *Journal of Fire Sciences* 17.1 (1999), pp. 42–56.

[13] Serge Bourbigot et al. “Recent Advances for Intumescent Polymers”. In: *Macromolecular Materials and Engineering* 289.6 (2004), pp. 499–511.

[14] Indrek S Wichman. “Theory of opposed-flow flame spread”. In: *Progress in Energy and Combustion Science* 18.6 (1992), pp. 553–593.

[15] Robert F McAlevy III et al. “The mechanism of flame spreading over the surface of igniting condensed-phase materials”. In: *Symposium (international) on combustion*. Vol. 12. 1. Elsevier. 1969, pp. 215–227.

[16] JN De Ris. “Spread of a laminar diffusion flame”. In: *Symposium (international) on Combustion*. Vol. 12. 1. Elsevier. 1969, pp. 241–252.

[17] John Norval De Ris. “The spread of a diffusion flame over a combustible surface”. PhD thesis. Harvard University, 1968.

[18] Michael A Delichatsios. “Creeping flame spread: energy balance and application to practical materials”. In: *Symposium (International) on Combustion*. Vol. 26. 1. Elsevier. 1996, pp. 1495–1503.

[19] Michael A. Delichatsios et al. “Creeping flame spread along fuel cylinders in forced and natural flows and microgravity”. In: *Proceedings of the Combustion Institute* 28.2 (2000), pp. 2835–2842.

[20] Michael A. Delichatsios. “Relation of opposed flow (creeping) flame spread with extinction/ignition”. In: *Combustion and Flame* 135.4 (2003), pp. 441–447.

[21] Yusuke Konno et al. “Downward flame spreading over electric wire under various oxygen concentrations”. In: *Proceedings of the Combustion Institute* 37.3 (2019), pp. 3817–3824.

[22] Osamu Fujita et al. “Effect of low external flow on flame spread over polyethylene-insulated wire in microgravity”. In: *Proceedings of the Combustion Institute* 29.2 (2002), pp. 2545–2552.

[23] Osamu Fujita et al. “Effective mechanisms to determine flame spread rate over ethylene-tetrafluoroethylene wire insulation: Discussion on dilution gas effect based on temperature measurements”. In: *Proceedings of the Combustion Institute* 28.2 (2000), pp. 2905–2911.

[24] Yuji Nakamura et al. “Flame spread over polymer-insulated wire in sub-atmospheric pressure: Similarity to microgravity phenomena”. In: *Progress in scale modeling*. Springer, 2008, pp. 17–27.

[25] Maria Thomsen et al. “On simulating concurrent flame spread in reduced gravity by reducing ambient pressure”. In: *Proceedings of the Combustion Institute* 37.3 (2019), pp. 3793–3800.

[26] Lauren Gagnon et al. “Effect of reduced ambient pressures and opposed airflows on the flame spread and dripping of LDPE insulated copper wires”. In: *Fire Safety Journal* 120 (2021), p. 103171.

[27] Yanli Zhao et al. “Pressure effect on flame spread over polyethylene-insulated copper core wire”. In: *Applied Thermal Engineering* 123 (2017), pp. 1042–1049.

[28] Yanli Zhao et al. “Experimental study on flame spread along fuel cylinders in high pressures”. In: *Fire and Materials* 43.8 (2019), pp. 1022–1030.

[29] Andres F Osorio et al. “Microgravity flammability limits of ETFE insulated wires exposed to external radiation”. In: *Proceedings of the Combustion Institute* 35.3 (2015), pp. 2683–2689.

[30] Xinyan Huang et al. “A Review of Fundamental Combustion Phenomena in Wire Fires”. In: *Fire Technology* 56 (2020), pp. 315–360.

[31] Akira Umemura et al. “Physical model analysis of flame spreading along an electrical wire in microgravity”. In: *Proceedings of the Combustion Institute* 29.2 (2002), pp. 2535–2543.

[32] Shuhei Takahashi et al. “Extinction limits of spreading flames over wires in microgravity”. In: *Combustion and Flame* 160.9 (2013), pp. 1900–1902.

[33] Shuhei Takahashi et al. “Study on unsteady molten insulation volume change during flame spreading over wire insulation in microgravity”. In: *Proceedings of the Combustion Institute* 34.2 (2013), pp. 2657–2664.

[34] Masashi Nagachi et al. “Effect of flow direction on the extinction limit for flame spread over wire insulation in microgravity”. In: 47th International Conference on Environmental Systems. 2017.

[35] Amit Kumar et al. “A comparison of extinction limits and spreading rates in opposed and concurrent spreading flames over thin solids”. In: *Combustion and flame* 132.4 (2003), pp. 667–677.

[36] Masashi Nagachi et al. “Can a spreading flame over electric wire insulation in concurrent flow achieve steady propagation in microgravity?” In: *Proceedings of the Combustion Institute* 37.3 (2019), pp. 4155–4162.

[37] Masashi Nagachi et al. “Effect of Ignition Condition on the Extinction Limit for Opposed Flame Spread Over Electrical Wires in Microgravity”. In: *Fire Technology* 56 (2020), pp. 149–168.

[38] Yusuke Konno et al. “Role of wire core in extinction of opposed flame spread over thin electric wires”. In: *Combustion and Flame* 220 (2020), pp. 7–15.

[39] Yusuke Konno et al. “Opposed-Flow Flame Spread and Extinction in Electric Wires: The Effects of Gravity, External Radiant Heat Flux, and Wire Characteristics on Wire Flammability”. In: *Fire Technology* 56 (2020), pp. 131–148.

[40] A. Guibaud et al. “Soot Production and Radiative Heat Transfer in Opposed Flame Spread over a Polyethylene Insulated Wire in Microgravity”. In: *Fire Technology* 56 (2020), pp. 287–314.

[41] Guibaud et al. “Experimental Evaluation of Flame Radiative Feedback: Methodology and Application to Opposed Flame Spread Over Coated Wires in Microgravity”. In: *Fire Technology* 56 (Jan. 2020), pp. 185–207.

[42] Augustin Guibaud et al. “On the effects of opposed flow conditions on non-buoyant flames spreading over polyethylene-coated wires – Part I: Spread rate and soot production”. In: *Combustion and Flame* 221 (2020), pp. 530–543.

[43] J.B. Henderson et al. “A Model for the Thermal Response of Polymer Composite Materials with Experimental Verification”. In: *Journal of Composite Materials* 19.6 (1985), pp. 579–595.

[44] Christian Vovelle et al. “Experimental and Numerical Study of the Thermal Degradation of PMMA”. In: *Combustion Science and Technology* 53.2-3 (1987), pp. 187–201.

[45] Stanislav I. Stoliarov et al. “Two-dimensional model of burning for pyrolyzable solids”. In: *Fire and Materials* 38.3 (2014), pp. 391–408.

[46] Chris Lautenberger et al. “Generalized pyrolysis model for combustible solids”. In: *Fire Safety Journal* 44.6 (2009), pp. 819–839.

[47] Kevin B McGrattan et al. *Fire dynamics simulator–Technical reference guide*. National Institute of Standards, Technology, Building, and Fire Research ..., 2000.

[48] Stanislav I. Stoliarov et al. “Prediction of the burning rates of non-charring polymers”. In: *Combustion and Flame* 156.5 (2009), pp. 1068–1083.

[49] Mihyun Kim et al. “Parameter Estimation for Comprehensive Pyrolysis Modeling: Guidance and Critical Observations”. In: *Fire Technology* 51 (Mar. 2015), pp. 443–477.

[50] Jing Li et al. “Measurement of kinetics and thermodynamics of the thermal degradation for non-charring polymers”. In: *Combustion and Flame* 160.7 (2013), pp. 1287–1297.

[51] Li et al. “Gasification experiments for pyrolysis model parameterization and validation”. In: *International Journal of Heat and Mass Transfer* 77 (2014), pp. 738–744.

[52] Gregory Linteris et al. “Absorption and reflection of infrared radiation by polymers in fire-like environments”. In: *Fire and Materials* 36.7 (2012), pp. 537–553.

[53] Marcos Chaos et al. “Evaluation of optimization schemes and determination of solid fuel properties for CFD fire models using bench-scale pyrolysis tests”. In: *Proceedings of the Combustion Institute* 33.2 (2011), pp. 2599–2606.

[54] Brian T Rhodes et al. “Burning rate and flame heat flux for PMMA in a cone calorimeter”. In: *Fire Safety Journal* 26.3 (1996), pp. 221–240.

[55] Naeem Iqbal et al. “Flame heat fluxes in PMMA pool fires”. In: *Journal of Fire Protection Engineering* 6.4 (1994), pp. 153–162.

[56] D Hopkins Jr et al. “Material fire properties and predictions for thermoplastics”. In: *Fire safety journal* 26.3 (1996), pp. 241–268.

[57] Gregory Linteris et al. “Modeling solid sample burning”. In: *Fire Safety Science–Proceedings of the Eight International Symposium, International Association for Fire Safety Science, Boston, MA*. Citeseer. 2005, pp. 18–23.

[58] Ahmed Kacem et al. “A fully coupled fluid/solid model for open air combustion of horizontally-oriented PMMA samples”. In: *Combustion and Flame* 170 (2016), pp. 135–147.

[59] Germain Boyer. “Fully coupled CFD simulation of the pyrolysis of non-charring polymers: A predictive approach”. In: *Fire Safety Journal* 91 (2017), pp. 208–217.

[60] Conor G McCoy et al. “Empirical Model of flame heat feedback for simulation of cone calorimetry”. In: *Fire Safety Journal* 103 (2019), pp. 38–48.

[61] Takashi Kashiwagi. “Polymer combustion and flammability—Role of the condensed phase”. In: *Symposium (International) on Combustion*. Vol. 25. 1. Elsevier. 1994, pp. 1423–1437.

[62] Serge Bourbigot et al. “Fire retardant polymers: recent developments and opportunities”. In: *Journal of Materials Chemistry* 17.22 (2007), pp. 2283–2300.

[63] Serge Bourbigot et al. “Intumescent polypropylene: Reaction to fire and mechanistic aspects”. In: *Fire Safety Journal* 105 (2019), pp. 261–269.

[64] M Muller et al. “Investigation of the synergy in intumescent polyurethane by 3D computed tomography”. In: *Polymer degradation and stability* 98.9 (2013), pp. 1638–1647.

[65] Jenny Alongi et al. “Intumescence: Tradition versus novelty. A comprehensive review”. In: *Progress in Polymer Science* 51 (2015). Environmentally Relevant and Hybrid Polymer Materials, pp. 28–73.

[66] G. Camino et al. “Study of the mechanism of intumescence in fire retardant polymers: Part I—Thermal degradation of ammonium polyphosphate-pentaerythritol mixtures”. In: *Polymer Degradation and Stability* 6.4 (1984), pp. 243–252.

[67] G. Camino et al. “Study of the mechanism of intumescence in fire retardant polymers: Part II—Mechanism of action in polypropylene-ammonium polyphosphate-pentaerythritol mixtures”. In: *Polymer Degradation and Stability* 7.1 (1984), pp. 25–31.

[68] G. Camino et al. “Study of the mechanism of intumescence in fire retardant polymers: Part VI—Mechanism of ester formation in ammonium polyphosphate-pentaerythritol mixtures”. In: *Polymer Degradation and Stability* 12.3 (1985), pp. 213–228.

[69] Serge Bourbigot et al. “Synergistic effect of zeolite in an intumescence process: study of the carbonaceous structures using solid-state NMR”. In: *Journal of the Chemical Society, Faraday Transactions* 92.1 (1996), pp. 149–158.

[70] Lishui Sun et al. “Co-microencapsulate of ammonium polyphosphate and pentaerythritol and kinetics of its thermal degradation”. In: *Polymer Degradation and Stability* 97.3 (2012), pp. 404–409.

[71] Xiang Li et al. “Synergistic effects of pentaerythritol phosphate nickel salt (PPNS) with ammonium polyphosphate in flame retardant of polyethylene”. In: *Journal of Thermal Analysis and Calorimetry* 122.1 (2015), pp. 359–368.

[72] Santosh Khanal et al. “Effects of intumescent flame retardant system consisting of tris (2-hydroxyethyl) isocyanurate and ammonium polyphosphate on the flame retardant properties of high-density polyethylene composites”. In: *Composites Part A: Applied Science and Manufacturing* 112 (2018), pp. 444–451.

[73] Tsilla Bensabath et al. “Anisotropy of expandable graphite to explain its behavior as a flame-retardant”. In: *Journal of Fire Sciences* 39.2 (2021), pp. 109–118.

[74] Tsilla Bensabath et al. “Intumescent polypropylene: Interactions between physical and chemical expansion”. In: *Fire and Materials* 45.3 (2021), pp. 387–395.

[75] Sungwook Kang et al. “Mechanism of heat transfer through porous media of inorganic intumescent coating in cone calorimeter testing”. In: *Polymers* 11.2 (2019), p. 221.

[76] GJ Griffin. “The modeling of heat transfer across intumescent polymer coatings”. In: *Journal of fire sciences* 28.3 (2010), pp. 249–277.

[77] Jing Li et al. “Development of pyrolysis models for charring polymers”. In: *Polymer Degradation and Stability* 115 (2015), pp. 138–152.

[78] Yan Ding et al. “Determination of kinetics and thermodynamics of thermal decomposition for polymers containing reactive flame retardants: Application to poly(lactic acid) blended with melamine and ammonium polyphosphate”. In: *Polymer Degradation and Stability* 129 (2016), pp. 347–362.

[79] Stanislav Stoliarov et al. “Parameterization and Validation of Pyrolysis Models for Polymeric Materials”. In: *Fire Technology* 52 (May 2015).

[80] Qi Sun et al. “Development of a pyrolysis model for an intumescent flame retardant system: Poly (lactic acid) blended with melamine and ammonium polyphosphate”. In: *Composites Part B: Engineering* 194 (2020), p. 108055.

[81] Yan Ding et al. “Development of a semi-global reaction mechanism for thermal decomposition of a polymer containing reactive flame retardant”. In: *Proceedings of the Combustion Institute* 37.3 (2019), pp. 4247–4255.

[82] Yan Ding et al. “Development of a pyrolysis model for glass fiber reinforced polyamide 66 blended with red phosphorus: Relationship between flammability behavior and material composition”. In: *Composites Part B: Engineering* 176 (2019), pp. 107–263.

[83] Longhua Hu et al. “Flame spread over electric wire with high thermal conductivity metal core at different inclinations”. In: *Proceedings of the Combustion Institute* 35.3 (2015), pp. 2607–2614.

[84] Yoshinari Kobayashi et al. “Flame spread over horizontal and vertical wires: The role of dripping and core”. In: *Fire Safety Journal* 91 (2017). Fire Safety Science: Proceedings of the 12th International Symposium, pp. 112–122.

[85] Carlos Fernandez-Pello. “The solid phase”. In: *Combustion Fundamentals of Fire*. Ed. by G. Cox. New-York: Academic Press Limited, 1994, pp. 31–100.

[86] Augustin Guibaud et al. “Pressure effects on the soot production and radiative heat transfer of non-buoyant laminar diffusion flames spreading in opposed flow over insulated wires”. In: *Combustion and Flame* 222 (2020), pp. 383–391.

[87] Augustin Guibaud et al. “Experimental evaluation of flame radiative feedback: methodology and application to opposed flame spread over coated wires in microgravity”. In: *Fire Technology* 56.1 (2020), pp. 185–207.

[88] Augustin Guibaud. *Flame spread in microgravity environment: influence of ambient flow conditions*. Oct. 2019.

[89] Yuji Sano et al. “The Heat Transfer Coefficient of Fine Wires in Air Flow”. In: *Chemical engineering* 28.4 (1964), 275–284, a1.

[90] Suhas V Patankar. *Numerical heat transfer and fluid flow*. Series on Computational Methods in Mechanics and Thermal Science. Hemisphere Publishing Corporation (CRC Press, Taylor & Francis Group), 1980.

[91] J. E. Mark. *Physical Properties of Polymers Handbook*. Ed. by James E. Mark. 2007.

[92] Yoshinari Kobayashi et al. “Opposed Flame Spread over Polyethylene Under Variable Flow Velocity and Oxygen Concentration in Microgravity”. In: *Fire Technology* 56 (2020), pp. 113–130.

[93] J. E. Mark. *Physical Properties of Polymers Handbook*. Springer, 2007.

[94] C.P. Fenimore et al. “Flammability of polymers”. In: *Combustion and Flame* 10.2 (1966), pp. 135–139.

[95] A.Y. Snegirev et al. “A new model to predict pyrolysis, ignition and burning of flammable materials in fire tests”. In: *Fire Safety Journal* 59 (2013), pp. 132–150.

[96] Colomba Di Blasi. “Modeling and simulation of combustion processes of charring and non-charring solid fuels”. In: *Progress in Energy and Combustion Science* 19.1 (1993), pp. 71–104.

[97] Chris Lautenberger et al. “The application of a genetic algorithm to estimate material properties for fire modeling from bench-scale fire test data”. In: *Fire Safety Journal* 41.3 (2006), pp. 204–214.

[98] Zohreh Ghorbani et al. “Limitations in the predictive capability of pyrolysis models based on a calibrated semi-empirical approach”. In: *Fire Safety Journal* 61 (2013), pp. 274–288.

[99] Joseph D Menczel et al. *Thermal analysis of polymers: fundamentals and applications*. John Wiley & Sons, 2009.

[100] Jean-Louis Consalvi et al. “Effects of oxygen depletion on soot production, emission and radiative heat transfer in opposed-flow flame spreading over insulated wire in microgravity”. In: *Combustion and Flame* 230 (2021), p. 111447.

[101] MOLLIE R Semmes et al. “A model for oxidative pyrolysis of corrugated cardboard”. In: *Fire Saf. Sci* 11 (2014), pp. 111–123.

[102] Duan et al. “Shuffled complex evolution approach for effective and efficient global minimization”. In: *Journal of Optimization Theory and Applications* 76 (Mar. 1993), pp. 501–521.

[103] Qingyun Duan et al. “Optimal use of the SCE-UA global optimization method for calibrating watershed models”. In: *Journal of hydrology* 158.3-4 (1994), pp. 265–284.

[104] John A Nelder et al. “A simplex method for function minimization”. In: *The computer journal* 7.4 (1965), pp. 308–313.

[105] Charles Mansfield Earnest. *Compositional analysis by thermogravimetry*. Vol. 997. ASTM International, 1988.

[106] Andrew Peacock. *Handbook of polyethylene: structures: properties, and applications*. CRC press, 2000.

[107] Courtney Harrison et al. “Polyethylene/boron nitride composites for space radiation shielding”. In: *Journal of applied polymer science* 109.4 (2008), pp. 2529–2538.

[108] Ibrahim Dubdub et al. “Pyrolysis of low density polyethylene: Kinetic study using TGA data and ANN prediction”. In: *Polymers* 12.4 (2020), p. 891.

[109] Jennifer L Jordan et al. “Mechanical properties of low density polyethylene”. In: *Journal of dynamic behavior of materials* 2.4 (2016), pp. 411–420.

[110] AS Luyt et al. “Thermal, mechanical and electrical properties of copper powder filled low-density and linear low-density polyethylene composites”. In: *Polymer Degradation and Stability* 91.7 (2006), pp. 1629–1636.

[111] AE Martell et al. “Standard reference data program (national Institute of standards and technology (US)) NIST critically selected stability constants of metal complexes., US Dept, of Commerce”. In: *National Institute of Standards and Technology, Standard Reference Data Program, Gaithersburg, Md* (2001).

[112] Stanislav I Stoliarov et al. “Determination of the heats of gasification of polymers using differential scanning calorimetry”. In: *Polymer Degradation and Stability* 93.2 (2008), pp. 422–427.

[113] M Le Bras et al. “Fire retarded intumescent thermoplastics formulations, synergy and synergistic agents–A review”. In: (1998), pp. 64–75.

[114] S. Bourbigot et al. “Carbonization mechanisms resulting from intumescence association with the ammonium polyphosphate-pentaerythritol fire retardant system”. In: *Carbon* 31.8 (1993), pp. 1219–1230.

[115] Shih-Hsuan Chiu et al. “Dynamic flame retardancy of polypropylene filled with ammonium polyphosphate, pentaerythritol and melamine additives”. In: *Polymer* 39.10 (1998), pp. 1951–1955.

[116] Yan Ding et al. “Pyrolysis model development for a polymeric material containing multiple flame retardants: Relationship between heat release rate and material composition”. In: *Combustion and Flame* 202 (2019), pp. 43–57.

[117] Ren Delobel et al. “Invariant values of kinetic parameters — Evaluation of fire retardancy application to the PP-APP/PER system”. In: *Makromolekulare Chemie. Macromolecular Symposia* 74.1 (1993), pp. 59–69.

[118] K.P. Venkitaraj et al. “Experimental thermal degradation analysis of pentaerythritol with alumina nano additives for thermal energy storage application”. In: *Journal of Energy Storage* 22 (2019), pp. 8–16.

[119] René Delobel et al. “Thermal Behaviours of Ammonium Polyphosphate-Pentaerythritol and Ammonium Pyrophosphate-Pentaerythritol Intumescent Additives in Polypropylene Formulations”. In: *Journal of Fire Sciences* 8.2 (1990), pp. 85–108.

[120] Michel Le Bras et al. “New Intumescent Formulations of Fire-retardant Polypropylene—Discussion of the Free Radical Mechanism of the Formation of Carbonaceous Protective Material During the Thermo-oxidative Treatment of the Additives”. In: *Fire and Materials* 20.4 (1996), pp. 191–203.

[121] Clariant. “MATERIAL SAFETY DATA SHEET (EXOLIT AP 422)”. In: (2004).

[122] Sigma-Aldrich. “Safety data sheet (Pentaerythriton for synthesis)”. In: (2021).

ANNEX

Annex 1: Article published in Combustion and Flame journal
Annex 2: Article published in Proceedings of the Combustion Institute

Combustion and Flame 230 (2021) 111447

Contents lists available at ScienceDirect

Combustion and Flame

journal homepage: www.elsevier.com/locate/combustflame

Effects of oxygen depletion on soot production, emission and radiative heat transfer in opposed-flow flame spreading over insulated wire in microgravity

Jean-Louis Consalvi[a,*], Augustin Guibaud[b], Alain Coimbra[a], Jean-Marie Citerne[c], Guillaume Legros[d]

[a] Aix-Marseille Université, CNRS, IUSTI UMR 7343, 5 rue E. Fermi, 13013 Marseille, France
[b] Department of Civil, Environmental and Geomatic Engineering, University College London, United Kingdom
[c] Sorbonne Université, CNRS, UMR 7190, Institut Jean Le Rond d'Alembert, Paris F-75005, France
[d] CNRS-ICARE, 1C av. de la Recherche Scientifique, 45071 Orléans cedex 2, France

ARTICLE INFO

Article history:
Received 27 December 2020
Revised 2 April 2021
Accepted 3 April 2021

Keywords:
Solid fuel
Soot production
Oxygen depletion
Microgravity
Opposed-flow flame spread
Electrical wire

ABSTRACT

The main objective of this article is to investigate experimentally and numerically the effects of reduced-oxygen contents on the soot production and emission from solid fuels in microgravity, which constitute an important issue in terms of fire safety for manned space missions. Due to its convenience for the implementation of soot-related optical diagnostics, the configuration of a flame spreading in an opposed flow over thin nickel chromium (NiCr) wires coated by low density PolyEthylene (LDPE) is considered. Experiments are conducted at a pressure of 101.3 kPa and an oxidizer velocity of 150 mm/s. The oxygen mole fraction in the oxidizer, X_{O_2}, is varied from 18% to 21% by nitrogen dilution of air. The modeling strategy lies on a surrogate fuel to mimic the combustion of LDPE by preserving its stoichiometry and the laminar smoke-point (LSP) flame height. The numerical model considers a detailed chemistry, a two-equation soot production model involving laminar smoke point (LSP)-based soot formation rates and oxidation by OH and O_2, a radiation model coupling the Full-Spectrum correlated-k method with the finite volume method, and a simple degradation model for LDPE. Based on experimental evidence, the soot formation rate is scaled by the adiabatic flame temperature to account for thermal effects due to variation in X_{O_2}. The model reproduces quantitatively the increase in flame size, residence time, and soot volume fraction observed experimentally as X_{O_2} is enhanced as well as the transition from a non-smoking to a smoking flame, which occurs for X_{O_2} between 19% and 20%. The increase in soot volume fraction results of a combined enhancement in both residence time, owing to an increase in the fuel mass flow rate, and soot formation rate due to higher temperature in the soot formation region. The radiant fraction increases significantly with X_{O_2} from about 17% for X_{O_2} =18% to about 36% for X_{O_2} = 21%. This increase in radiative losses is accompanied by a reduction of the temperature in the soot oxidation region. Therefore, for increasing X_{O_2}, the soot oxidation process is governed by a competition between oxygen-enhanced conditions that promote the formation of soot oxidizing species and the increase in radiative losses that dampens their formation. For the present flames, the first mechanism prevails as X_{O_2} increases from 18% to 19% whereas the second dominates as X_{O_2} is further increased, leading to smoking flames as actually observed for X_{O_2}=20 and 21%. The radiant fraction at the smoke-point transition and the soot oxidation freezing temperature are in line with those reported at normal gravity. Finally, model results show that, whatever X_{O_2}, the contribution of radiation to the heating process is negligible ahead of the pyrolysis front and is largely overcome by surface radiative losses along the pyrolysis region.

1. Introduction

Ignition and flame spread over idealized thin electrical wires, composed by a metal core coated with a polymer, has received a considerable attention over the last twenty years due to the high interest of this configuration for fire safety [1]. In particular, elec-

* Corresponding author.
E-mail address: jean-louis.consalvi@univ-amu.fr (J.-L. Consalvi).

https://doi.org/10.1016/j.combustflame.2021.111447
0010-2180/

Nomenclature

A_S	soot surface area [m^{-1}]
E_a	activation energy [kJ/mol]
f_S	soot volume fraction [-]
L_{fl}	flame length [m]
L_S	distance from the molten droplet leading edge to the integrated SVF peak [m]
l_{sp}	laminar smoke point height [m]
$\dot{m}_p$	pyrolysis mass flow rate [kg•s^{-1}]
$\dot{m}''_p$	pyrolysis mass flow rate per unit area [kg•m^{-2}•s^{-1}]
N_A	Avogadro number [part•mol^{-1}]
NC_{min}	number of carbon atoms in the incipient soot particle [-]
N_S	soot number density per unit mass of mixture [part•kg^{-1}]
P	pressure [Pa]
P_{OH}	OH partial pressure [Pa]
P_{O_2}	O_2 partial pressure [Pa]
$\dot{q}''_{R,inc}$	incident radiative flux [W•m^{-2}]
$\dot{q}''_{R,w}$	surface re-radiation [W•m^{-2}]
r	radial coordinate [m]
r_{fl}	flame radius [m]
R_{wire}	wire radius [m]
R_u	universal gas constant (kJ/(mol K))
S	Stoichiometric oxidizer/fuel volumetric ratio [-]
s	Stoichiometric oxidizer/fuel mass ratio [-]
S_b	surface of the molten ball [m^2]
T	temperature [K]
T_{ad}	adiabatic flame temperature [K]
T^0_{ad}	adiabatic flame temperature for $X_{O_2} = 20\%$ [K]
u_F	Fuel injection velocity [m•s^{-1}]
u_p	spread rate [m•s^{-1}]
u_{ox}	oxidizer flow velocity [m•s^{-1}]
W_i	molecular weight of the i^{th} species [kg•mol^{-1}]
x_i	mole fraction of the i^{th} species [-]
X_{O_2}	mole fraction of oxygen in the oxidizer [-]
z	axial coordinate [m]
α_g	gas thermal diffusivity [m^2•s^{-1}]
δ	stand-off distance [m]
η_{OH}	collision efficiency of OH [-]
ξ	mixture fraction [-]
ρ_g	gas density [kg•m^{-3}]
τ	residence time [s]
χ_R	radiant fraction [-]
$\dot{\omega}_{coag}$	reaction rate for soot coagulation [part•m^{-3}•s^{-1}]
$\dot{\omega}_n$	reaction rate for soot nucleation [mol•m^{-3}•s^{-1}]
$\dot{\omega}_{N_S}$	reaction rate for soot number density [part•m^{-3}•s^{-1}]
$\dot{\omega}''_{O_2}$	reaction rate for soot oxidation by O_2 per unit soot surface area [kg•m^{-2}•s^{-1}]
$\dot{\omega}''_{OH}$	reaction rate for soot oxidation by OH per unit soot surface area [kg•m^{-2}•s^{-1}]
$\dot{\omega}_{OH}$	reaction rate for soot oxidation by OH [kg•m^{-3}•s^{-1}]
$\dot{\omega}_{SF}$	reaction rate for soot formation rate [kg•m^{-3}•s^{-1}]
$\dot{\omega}^{X^0_{O_2}}_{SF,P}$	peak of soot formation rate for $X^0_{O_2}$=20% [kg•m^{-3}•s^{-1}]
$\dot{\omega}^{X_{O_2}}_{SF,P}$	peak of soot formation rate for X_{O_2} [kg•m^{-3}•s^{-1}]
$\dot{\omega}_{Y_S}$	source term for soot mass fraction [kg•m^{-3}•s^{-1}]

Subscript

ad	adiabatic
b	molten ball
fl	flame
g	gas
inc	incident
max	maximum
p	pyrolysis
PE	polyethylene
R	radiation or radiative
sp	smoke point
S	soot
∞	ambient

Superscript

0	reference

Acronyms

BMAE	Broadband Modulated Absorption Emission
FSCK	Full-Spectrum correlated-k
LDPE	low density polyethylene
LSP	laminar smoke point
PE	polyethylene
SF	soot formation
SP	smoke point
SVF	soot volume fraction
SO	soot oxidation

trical wires were identified as the primary cause of fire initiation and growth in a space vehicle. This has resulted in specific experimental, theoretical and numerical studies in microgravity environments to get insights into flame spread characteristics and flammability properties [2–12].

The release of smoke is a critical aspect of fire safety, as evidenced by the various fire incidents reported in the context of manned space missions [13–18]. In addition, smoke and flame radiation constitute signatures of fire appearance to develop fire detection strategies in microgravity conditions [2]. Although most of these incidents, at the noticeable exception of that aboard Mir in 1997, involved smoke released in the absence of flame, and the early detection of fires from smoke generated by oxidative pyrolysis (such as smoldering) is desirable to allow the crew to respond before a larger flaming situation develops [19], the soot released from flaming solids, including polymers, is also of fundamental and applicative interest [20,21]. Beyond the study of material flammability, the opposed flow spreading of laminar diffusion flames over idealized cylindrical electrical wires in microgravity offers a unique configuration to investigate soot production, smoke release and, corresponding radiative heat transfer processes from flaming solid fuels [21–26]. The 2D axisymmetric geometry enables the implementation of advanced optical diagnostics based on extinction techniques, such as the BMAE (Broadband Modulated Absorption Emission) technique [27], to measure local soot volume fraction (SVF) and temperature. A proper selection of the metallic core enables the formation of a stable laminar boundary layer diffusion flame spreading at a steady rate over the 22 s of microgravity in parabolic flights [22–26]. In addition, the presence of the metallic core, on the one hand, ensures the rigidity of the configuration maintaining an axisymmetric boundary layer within the flame spread and, on the other hand, avoids the occurrence of a dripping process. Finally, the microgravity environment promotes longer residence times than those encountered in buoyant flames. The effects of ambient conditions, namely pressure, P, oxygen content in the oxidizer, X_{O_2}, and oxidizer flow velocity, u_{ox}, on soot production and emission were experimentally investigated using the BMAE in parabolic flights for flames propagating in opposed flow over thin electrical wires. The studied samples were

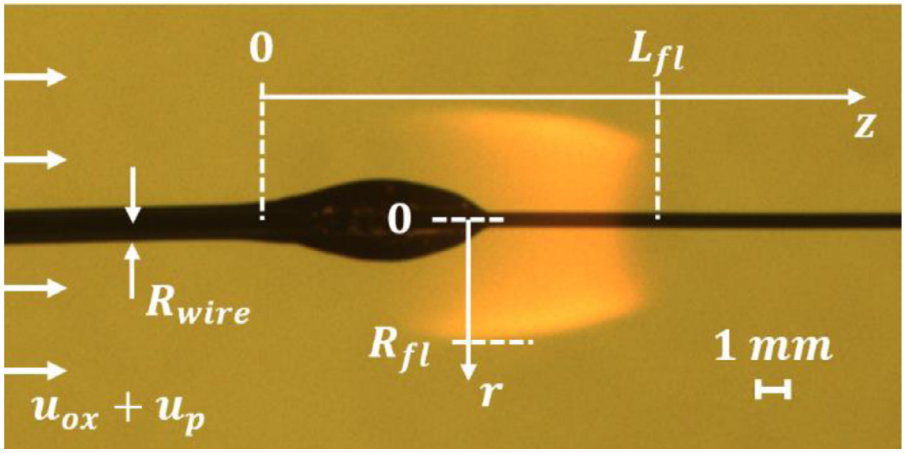

Fig. 1. Backlighted frame imaging a flame spreading over a wire in opposed flow conditions in microgravity. Main features of the flame geometry, subsequent notations adopted, and a 1 mm scale are overlaid.

made of a 0.5 mm in diameter NiCr metallic core coated by a 0.3 mm thick layer of LDPE [23,24]. P, X_{O_2}, and u_{ox} were varied between 51 kPa and 142 kPa, 18% and 21%, 100 mm/s and 200 mm/s, respectively. LDPE was selected as solid fuel for three main reasons. First, it corresponds to an international target configuration to investigate fundamentally the flammability properties of electrical wires [2,4,8–12,22–26]. Second, it produces SVF levels above the detection threshold of the BMAE over the ranges of pressure, oxygen content, and flow velocity considered. Finally, the corresponding flames undergo a transition from a non-smoking flame to a smoking one over these ranges.

These experimental investigations were accompanied by the development of a numerical model, involving the coupling of a detailed chemistry and a state-of-the-art radiation model, to help in the interpretation of data [25,26]. The main challenge in the modeling of the gas-phase processes resulting from the combustion of solid fuels lies in the fact that the gaseous pyrolysis products are generally not well identified and some simplifications, such as a global one-step chemical reaction, have to be introduced due to this lack of information. In order to circumvent this limitation and to be able to consider a detailed chemistry with access to soot precursors and soot oxidizing species such OH radicals, a numerical fuel surrogate, inspirited from the works of Refs. [28,29], was designed to mimic the gas-phase combustion of PE in terms of flame structure and fuel sooting propensity. In our approach the fuel sooting propensity is related to the laminar smoke-point (LSP) height and the LSP strategy, initiated in Refs. [30,31], was adopted to determine the soot production rates of PE. This strategy is based on the analysis developed by De Ris et al. [32] from experimental evidence that the soot production rates of a given fuel are inversely proportional to the LSP height. In practice, the soot production rates are established for a reference fuel, typically ethylene, and the model is extended to other fuels by scaling the aforementioned rates by the inverse of the corresponding LSP flame height [30,31]. In our approach, a two-equation LSP-based soot production model was specifically developed, extending the one-equation formulation proposed in Refs [30,31]. This extended approach is expected to improve the soot oxidation description by considering explicitly the surface area dependence of the soot oxidation rates by O_2 and OH [33]. The combination of the experimental results and simulations provided a detailed characterization of the effects of pressure on flame structure, soot production and soot emission [23,26]. More specifically, it was found that increasing the pressure does not affect the residence time in the present configuration and that, over the range of pressures investigated, the soot formation rate of LDPE is third order in pressure. In addition, consistently with data obtained at normal gravity [34–37], the smoke-point transition was found to occur for a radiant fraction of about 0.3 and the soot oxidation freezing temperature was estimated in the range 1350–1450 K.

The present article focuses on the effects of X_{O_2} on flame structure, soot production, and soot emission in the opposed flow flame spreading over NiCr/LPDE wires for X_{O_2} lower than 21%. The main objectives are: i) to extend the previously-developed two-equation LSP-based soot production model to account for X_{O_2} effects, ii) to further validate the surrogate fuel modeling strategy by comparison with the available experimental data reported in Refs. [23,24], and iii) to provide insights into the ways X_{O_2} affects both soot formation (SF) and soot oxidation (SO) processes as well as the resulting smoke emission and radiative heat transfer. The article is organized as follows. Sections 2 and 3 present the experimental set-up and the main features of the numerical model, respectively. The two-equation LSP model and the developments performed to account for X_{O_2} effects are described in Section 4. The results are discussed in Section 5. Finally, Section 6 summarizes the main conclusions of the paper.

2. Experimental set-up

Experiments were conducted in parabolic flights. The experimental setup and the optical diagnostics are detailed in Refs. [22–24] and are only briefly described here. Cylindrical 150 mm long wires, consisting of a 0.5 mm diameter NiCr core coated with a 0.3 mm thick LDPE insulation, are placed along the central axis of a cylindrical combustion chamber with an inner diameter of 190 mm. For all the experiments considered in the present study, the pressure and flow velocity were set equal to 101.3 kPa and 150 mm.s^{-1}, respectively. X_{O_2} was varied between 18% and 21% by nitrogen dilution of air. The samples were ignited using a hot Kanthal wire at the beginning of the parabolic sequence, resulting in an opposed-flow flame spread. As discussed in the introduction, this choice of NiCr and dimensions enable the formation of a stable steady-spreading axisymmetric laminar boundary layer diffusion flame over the 22 s of microgravity in parabolic flights for the range of ambient conditions studied [22–26].

Flame spread rate, pyrolysis mass flow rate, and SVF were determined during the steady flame spread using the optical diagnostics described in details in Ref. [23]. In particular, SVF fields were obtained using the B-MAE technique as extensively outlined in Ref. [27]. This technique enables the recovery of the SVF and temperature with an uncertainty lower than 1 ppm and 100 K, respectively. In agreement with observations reported in previous

Table 1
Main characteristics of the flames investigated in the present study. The pressure and the oxidizer velocity are 101.3 kPa and 150 mm.s^{-1}, respectively.

(%)	18	19	20	21
u_p (mm/s)	1.11 ± 0.08	1.27 ± 0.07	1.33 ± 0.01	1.46 ± 0.07
$\dot{m}_p$ (mg/s)	0.77 ± 0.058	0.879 ± 0.048	0.925 ± 0.01	1.01 ± 0.05
L_f (mm)	12.41 ± 0.42	14.40 ± 0.77	15.50 ± 0.36	16.19 ± 0.32
r_f (mm)	3.26 ± 0.06	3.47 ± 0.19	3.62 ± 0.28	3.78 ± 0.08
$f_{S,max}$ (ppm)	10.20 ± 0.82	13.85 ± 1.12	16.73 ± 0.96	22.70 ± 1.36
L_S (mm)	10.01 ± 0.21	11.40 ± 0.31	12.40 ± 0.24	13.50 ± 0.12
τ_{SF} (ms)	66.60	76.00	82.66	90.00
S (-)	16.67	15.78	15.00	14.28
Smoking/non-smoking	Non-smoking	Non-smoking	Smoking	Smoking

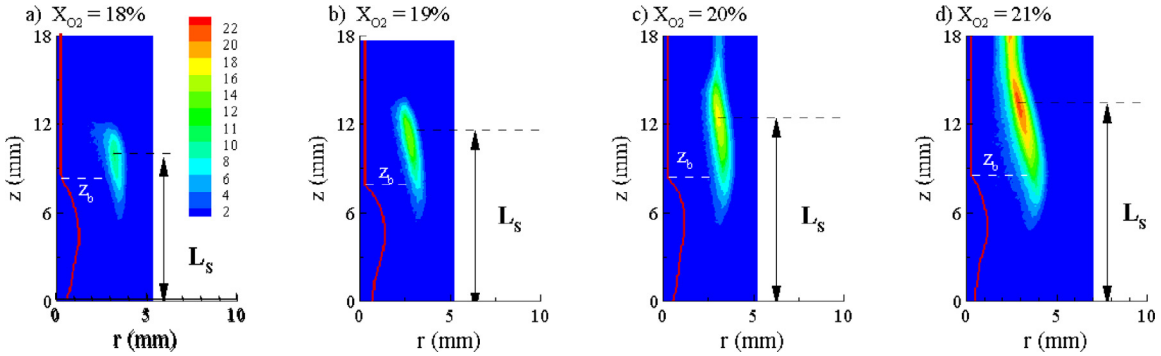

Fig. 2. Fields of SVF in ppm for a) X_{O_2}=18%, b) X_{O_2}=19%, c) X_{O_2}=20% and d) X_{O_2}=21%. The red solid line represents the wire surface. The origin of the z-coordinate is located at the molten ball leading edge that is assumed to correspond to the pyrolysis front. z_b represents the trailing edge of the pyrolyzing region. (For interpretation of the references to colour in this figure legend, the reader is referred to the web version of this article.)

works [8,21,26,38,39], LDPE was characterized by the formation of gaseous bubbles in the molten phase as it degrades, which then burst and eject fragments of molten PE into the gas phase after they reached the fuel surface. These events were mainly observed at higher oxygen content (X_{O_2} =0.21) and were found to be sufficiently sparse to affect significantly neither the mean soot production level nor the smoke point transition at the flame trailing edge. Nevertheless, although the resulting perturbations do not affect the flame downstream, the local signal deformation in flame emission means that the error on local flame temperature increases drastically [26]. As a result, only SVF experimental fields are reported here.

The flame was assumed to spread at a steady rate once the dimensions of the characteristic molten insulation droplet (see Fig. 1), the visible flame length, and the rate of the flame front displacement reach a steady state value [22]. The flame spread rate, u_p, is evaluated by tracking the time evolution of the luminous flame front whereas the pyrolysis mass flow rate, $\dot{m}_p$, is then evaluated from u_p assuming $\rho_{PE} = 920$ kg/m^3.

Table 1 presents the main characteristics of the four flames investigated in the present study. As illustrated on Fig. 1, the luminous flame radius, r_f, and flame length, L_f, are defined as the distances between the coated wire and the maximum radial location of the luminous flame and between the pyrolysis front, identified by molten droplet leading edge, and the maximum axial location of the luminous flame, respectively. Similarly, the SF characteristic length scale, L_S, is defined as the axial distance between the molten droplet leading edge and the peak of SVF (see Fig. 2). Table 1 shows that u_p, $\dot{m}_p$, L_f, r_f, L_S, and the peak of SVF, $f_{S,max}$, increase with X_{O_2}. $f_{S,max}$ increases from about 10.20 ppm for X_{O_2} =18% to about 22.70 ppm for X_{O_2} =21%. The residence time for the SF process, that can be estimated as $\tau_{SF} = L_S/u_{ox}$, increases also with X_{O_2}. The flames for X_{O_2}=18% and 19% are non-smoking whereas the flames for X_{O_2}=20% and 21% are smoking, showing that the smoke point transition occurs somewhere between X_{O_2}=19% and 20% (see Fig. 2).

3. Numerical model

A detailed description of the numerical model can be found in Refs. [25,26] and only a summary is given here. The model solves the governing equations of both gaseous and solid phases in a flame-fixed axisymmetric coordinate system.

For the gas phase, the Navier-Stokes equations and transport equations for gas-phase species mass fractions and energy are solved. The numerical methods as well as the strategy for handling the stiffness of the equation system can be found in Refs. [25,26]. As discussed in the introduction, a surrogate fuel is designed to mimic the gas-phase combustion of PE in terms of flame structure and fuel sooting propensity. This strategy, widely inspired from that used to develop the Burning Rate Emulator (BRE) to simulate the burning of condensed fuels [28,29], consists in preserving the heat of combustion (or similarly the oxygen-fuel mass ratio) to reproduce the flame structure, and the laminar smoke point (LSP) height to reproduce the fuel sooting propensity. Pure ethylene is adopted to represent the pyrolysis products of LDPE since both species exhibit very similar heat of combustion with a discrepancy lower than 10% and the same oxygen-fuel mass ratio [40]. The LSP height of LPDE will be preserved in the soot production model in order to mimic its sooting propensity (see Section 4). This surrogate fuel modeling strategy was found to be able to reproduce accurately the experimental flame structure, soot production and soot emission of flames spreading over LDPE wires under different pressure levels [26]. The oxidation of ethylene is modelled using the full chemical kinetic scheme developed by Qin et al. [41].

The present study focuses on gas-phase processes. Therefore, the conjugated heat transfer problem at the gas/solid interface is simplified since its solution is only required to provide proper boundary conditions for the gas-phase modeling. The spread rates, the pyrolysis mass flow rate, the structure of the burning wire and the shapes of the molten LDPE droplet are specified as inputs from the experimental steady spreading data. The steady structure of the burning wire consists of three regions as shown in

Figs. 1 and 2:i) the insulated wire located ahead of the pyrolysis front for $z \leq 0$, ii) the molten ball corresponding to the pyrolysing region for $0 \leq z \leq z_b$, and iii) the bare NiCr core for $z > z_b$. The experimental data in Fig. 2 show that the shape of the molten ball is hardly affected by the different X_{O_2} and, for the sake of simplicity, the molten ball obtained for $X_{O_2} = 19\%$ will be adopted for all the simulations. In the pyrolysing region, the fuel injection velocity profile, $u_F(z)$, is determined from the measured fuel mass flow rate, $\dot{m}_P$, the ball surface, S_b, and the stand-off distance, $\delta(z)$ by assuming that $\dot{m}''_P$, is inversely proportional to $\delta(z)$ [25,26].

The axisymmetric heat transfer equation in the condensed phases is solved for both the metallic core and LDPE by assuming that both LPDE melting and pyrolysis processes behave as phase transitions. Based on these assumptions, the PE located ahead of the pyrolysis front can be in: i) a virgin state if $T_{PE} < T_{melt}$, with T_{melt} =403 K, ii) at the transition if $T_{PE} = T_{melt}$ and, iii) in the molten phase if $T_{PE} > T_{melt}$. The pyrolysis process is assumed to occur at the molten ball surface at a fixed temperature, T_p=760 K. All the thermal constants for the LDPE, including density, conductivity and heat capacity of both virgin and molten LDPE, temperature and heat of melting and pyrolysis temperature were taken from thermal analysis [9,25,42]. During the melting stage, the thermal properties are computed using a mass-weighted average between the properties of solid and those of the molten LDPE [25,26].

A detailed description of the radiation model can be found in Refs. [25,26]. CO_2, H_2O and soot are considered as the only radiating species since it was found that the contribution of CO is negligible. The radiation model combines the Full-Spectrum Correlated-K (FSCK) [43] as a gas-soot radiative property model and the Finite Volume Method [44] as radiative transfer equation solver. The angular mesh consists in the present simulations of 12×16 control angles. The emissivities of the LPDE, whether in its virgin or molten states, and of the NiCr along the bare wire were set equal to 1.

4. Soot production model

4.1. Formulation

Smoke production is assumed to be only a gas-phase process since, as discussed in Section 2, the generation of solid particles from the bursting of LPDE bubbles were observed mainly for X_{O_2} =0.21 and were found to be sparse enough to have no significant effects on soot production and smoke point transition.

The two-equation LSP soot production model, proposed in Ref. [26] and based on transport equations for soot number density per unit mass of mixture (N_s) and soot mass fraction (Y_s), is adopted and further developed to account for the influence of oxygen depletion on soot formation. Thermophoretic velocities are included in N_s and Y_s conservation equations.

The source term, $\dot{\omega}_{Y_s} = \dot{\omega}_{SF} - (\dot{\omega}''_{O_2} + \dot{\omega}''_{OH})A_S$, accounts for SF and SO by O_2 and OH. The SO rates by OH and O_2, optimized by Guo et al. [33], were considered:

$$\dot{\omega}''_{OH} = 1.27 \times 10^{-2} \frac{\eta_{OH} P_{OH}}{\sqrt{T}} \tag{1}$$

$$\dot{\omega}''_{O_2} = 15.8 \frac{P_{O_2}}{\sqrt{T}} exp\left(-E_{A,O_2}/R_u T\right) \tag{2}$$

with η_{OH} =0.1 and E_{A,O_2} =195 kJ/mol [33]. The source term, $\dot{\omega}_{N_S}$, for the soot number density is given by $\dot{\omega}_{N_S} = N_A/NC_{min}\dot{\omega}_n - \dot{\omega}_{coag}$ where N_A and NC_{min} =60 are the Avogadro number and the number of carbon atoms in the incipient soot particle [45], respectively. The coagulation rate, $\dot{\omega}_{coag}$, is computed as proposed by Lindstedt [45] with a Van der Walls enhancement factor of 9.

4.2. Soot formation and nucleation rates

4.2.1. Background

The modeling of the SF rate, $\dot{\omega}_{SF}$, in the case of the combustion of solid fuels is challenging since, as discussed in the introduction, the gaseous fuel released by the material pyrolysis is generally not well identified. In order to circumvent this issue, LSP-based soot production models have emerged over the last decade [30]. The main idea of these models is to map $\dot{\omega}_{SF}$ as a function of mixture fraction, ξ, and temperature, T, for a reference gaseous fuel, typically ethylene, burning in air under atmospheric pressure. The mapping proposed by Lautenberger et al. [30] for ethylene is adopted, leading to $\dot{\omega}_{SF} = f_{SF}(\xi) g_{SF}(T)$. f_{SF} and g_{SF} are cubic functions whose coefficients are determined by specifying the value and slope of the polynomials at the peak and at the lower and higher limits of the SF process.

Based on experimental evidence, the model is extended to other fuels by scaling the peak of SF rate obtained for the reference fuel by the inverse of the corresponding LSP flame height. The LSP flame height quantifies the propensity of a given fuel to release soot [32]. It represents the height of a well-ventilated axisymmetric laminar diffusion flame burning in air under atmospheric pressure at which soot starts to be released from the flame tip [32]. Also based on experimental evidence, LSP-based soot production models can be extended to sub- and super-atmospheric pressures by scaling the peak of SF rate by $(P/P_0)^n$, where P_0 is the atmospheric pressure [32].

Based on these considerations and on the initial formulation of Lautenberger et al. [30], the expression of the peak of soot formation rates can be estimated as:

$$\dot{\omega}_{SF,P} = 1.1 Y_{FT} \frac{l_{sp,C_2H_4}}{l_{sp,PE}} \left(\frac{W_{C_2H_4}}{W_{PE}}\right) \left(\frac{P}{P_0}\right)^n \tag{3}$$

where l_{sp,C_2H_4} and $l_{sp,PE}$ are the SP flame heights of ethylene and PE that have been estimated to be equal to 0.106 m and 0.045 m, respectively [40]. Y_{FT} is the mass fraction of fuel in the fuel supply stream. The constant 1.1 was calibrated to match SF in axisymmetric laminar ethylene diffusion flames burning in air at atmospheric pressure [30].

Eq. (3) was updated to model SF of PE in our previous study [26] for two reasons: i) the composition of the pyrolysis products and, in turn, W_{PE} are not known, and ii) the modeling has considered LDPE samples burning over a range of pressure in under-oxygenated conditions with $X_{O_2} = 20\%$. This particular value of X_{O_2} was the most suitable to investigate pressure effects over soot production since SVF was found to be above the detection threshold of the BMAE over a wide range of pressures while avoiding undesirable instabilities related to the formation and burst of bubbles in the LDPE as mainly observed for X_{O_2} =0.21. As a consequence, the term $(\frac{W_{C_2H_4}}{W_{PE}})$ was ignored in our formulation and the constant 1.1 was recalibrated to match the experimental SVF peak in a flame spreading over a wire coated by LDPE at a nominal pressure P =101.3 kPa, and $X_{O_2} = 20\%$. The calibrated constant was found equal to 0.5, leading to:

$$\dot{\omega}^{X^0_{O_2}}_{SF,P} = 0.5 Y_{FT} \frac{l_{sp,C_2H_4}}{l_{sp,PE}} \left(\frac{P}{P_0}\right)^n \tag{4}$$

where $X^0_{O_2}$ =20%. In addition, an analysis of our experimental data showed that n is equal to 3, approximately, for pressure ranging from 50 kPa to 140 kPa [23,26].

The nucleation rate, $\dot{\omega}_n$, was computed by revisiting the acetylene-based inception model developed by Lindstedt [45]. The initial formulation was multiplied by $l_{sp,C_2H_4}/l_{sp,PE}$ to account for the difference in sooting propensity between ethylene and PE:

$$\dot{\omega}_n = 2k_1(T) l_{sp,C_2H_4}/l_{sp,PE}[C_2H_2] \tag{5}$$

Table 2
Experimental flow conditions for the axisymmetric laminar coflow ethylene diffusion flames at normal gravity and atmospheric pressure.

Ref.	Characteristic	Fuel Stream		Oxidizer Stream	S (-)	T_{ad} (K)
		X_F	X_{N_2}	X_{O_2} (%)		
Sun et al. [46]	d_F =10.5 mm $\dot{Q}_F$ =3.85 cm^3/s	1	0	21–36.9	14.28–8.13	2368–2773
		1	0	16.8–0.21	17.85–14.28	2145–2368
		0.8–0.95	0.05–0.20	16.8–0.20	14.28	2130–2317
Zeng et al. [49]	d_F=16.4 mm $\dot{Q}_F$=2.80 cm^3/s	1	0	15.2–20.9	19.73–14.35	2026–2361
Fuentes et al. [47]	d_F=10.0 mm $\dot{Q}_F$=2.35 cm^3/s	1	0	17–35	17.65–8.57	2152–2744

where $[C_2H_2]$ is the acetylene concentration. The kinetic parameter, $k_1(T)$, is provided by Lindstedt [45].

The semi-empirical soot production model described above was found to capture quantitatively the pressure effects on both SF and SO processes for flames spreading over LDPE wires for $X^0_{O_2}$ =20% [26].

4.2.2. Effects of oxygen depletion

The objective of this section is to extend the present LSP model to account for variations of X_{O_2} with a special emphasis for oxygen-reduced oxidizers. Varying X_{O_2} modifies two fundamental properties of diffusion flames, namely, the volumetric stoichiometric oxidizer to fuel ratio, S, and the adiabatic flame temperature, T_{ad} [46]. Experiments and detailed numerical simulations of axisymmetric laminar coflow diffusion flames at normal gravity suggest that S controls mainly the flame geometry and, in turn, the residence times whereas the effects on SF and SO rates are rather related to thermal effects that affect the formation of soot precursors and soot oxidizing species [31,46–48]. These effects are directly included in soot nucleation (see Eq. (5)) and oxidation rates (see Eqs. (1) and (2)) that depend explicitly on temperature and concentrations of the corresponding species. In addition, the present model assumes that the effects of X_{O_2} on the peak of SF rate are only related to T_{ad}:

$$\dot{\omega}^{X_{O_2}}_{SF,P} = \dot{\omega}^{X^0_{O_2}}_{SF,P} \times \left(\frac{T_{ad}}{T^0_{ad}}\right)^m \tag{6}$$

where T^0_{ad} is the adiabatic flame temperature for $X^0_{O_2}$ =20%.

The exponent m is determined through the analysis of available experimental data. The selected set of experimental data includes axisymmetric laminar ethylene diffusion flames at normal gravity as well as spreading flames from the present study. The flow conditions relative to the experiments at micro and normal gravity are summarized in Tables 1 and 2, respectively. Table 2 shows that Sun et al. [46] considered a Santoro-type burner with an inner diameter of 10.5 mm for the central fuel tube and an inner diameter of 97.7 mm for the outer tube. For all the experiments, the fuel and oxidizer injection velocities were maintained unchanged and equal to 3.98 cm/s and 24.0 cm/s, respectively, leading to a volumetric fuel flow rate of 3.85 cm^3/s. Their comprehensive set of flow conditions included ethylene flames burning in both oxygen-enriched and oxygen-reduced oxidizers. For the oxygen-reduced oxidizers, two sub-sets of experiments were considered. In the first, pure ethylene injected trough the central tube while the oxidizer was diluted by nitrogen, leading to variations in S. In the second, both fuel and oxidizer were diluted by nitrogen to maintain S constant. Therefore, for a given X_{O_2}, these two sub-sets of data are characterized by different values of S but very similar values of T_{ad}. This enables separate investigation of the effects of S and T_{ad} on the SF rates. In the experiments of Sun et al. [46], SVF were measured with planar Laser Induced Incandescence (LII). Zeng et al. [49] also used LII technique to measure SVF in laminar axisymmetric ethylene-air/N_2 diffusion flames generated from a Santoro type burner with an inner diameter for the central fuel tube of 16.4 mm. The fuel and oxidizer flow rates were maintained at 2.80 cm^3/s and 65 L/min, respectively. The air and N_2 flow rates in the oxidizer were adjusted to vary X_{O_2} between 0.209 and 0.152. Fuentes et al. [47] considered both oxygen-enriched and oxygen-reduced laminar coflow ethylene diffusion flames stabilized on a Santoro-type burner with an inner diameter for the central fuel tube of 10.0 mm. The fuel and oxygen flow rates were kept constant at 2.345 cm^3/s and 20 L/min, respectively, whereas the nitrogen flow rate was decreased from 97.6 to 37.1 L/min to vary X_{O_2} from 0.17 to 0.35. In their experiments, the SVF was measured by using a laser extinction technique at a wavelength of 670 nm.

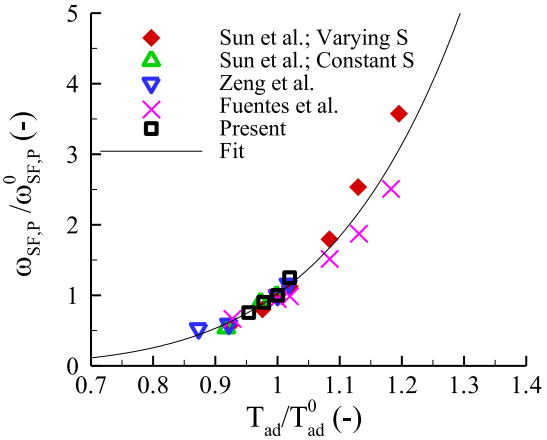

Fig. 3. $\dot{\omega}_{SF,P}/\dot{\omega}^0_{SF,P}$ as a function of T_{ad}/T^0_{ad}. This figure includes the experimental data obtained from Sun et al. [46], Zeng et al. [49], and Fuentes et al. [47], in laminar coflow ethylene diffusion flames at normal gravity as well as the present data. The fit is expressed as $(\dot{\omega}_{SF,P}/\dot{\omega}^0_{SF,P}) = (T_{ad}/T^0_{ad})^m$ with m =6.17 and a coefficient of determination, R^2 =0.97.

SF and SO processes occur mainly in different regions in axisymmetric laminar diffusions flames [48] (see also the discussion in Section 5.4). As a consequence, the peak of SF rate can be estimated from the conservation of soot mass fraction in a Lagrangian sense in the SF region, $\frac{D(\rho_s f_s)}{Dt} \propto \frac{\rho_s f_{s,max}}{\tau_{SF}} = \dot{\omega}_{sf,P}$. For the laminar coflow diffusion flames at normal gravity, τ_{SF} is estimated as $\sqrt{2L_S/a}$, where L_S represents the distance above the burner at which the SVF peaks and $a = g(\frac{T_{ad}}{T_\infty} - 1)$ is a buoyant acceleration [50]. As discussed in Section 2, τ_{SF} is computed as L_S/u_{ox} for the present micro-gravity flames (see Table 1). Figure 3 shows that all the experimental data collapse on a single curve when $\dot{\omega}_{SF,P}/\dot{\omega}^0_{SF,P}$ is plotted as a function of T_{ad}/T^0_{ad}. This correlation includes both the data obtained with constant and varying S, supporting that the adiabatic flame temperature is the predominant parameter affecting the SF process when varying X_{O_2}. These results show also that the exponent m in Eq. (6) can be taken equal to 6.17.

5. Results and discussions

5.1. Computational details

Simulations are performed in an overall computational domain of 4 cm (r) × 6 cm (z). The computational domain is divided into

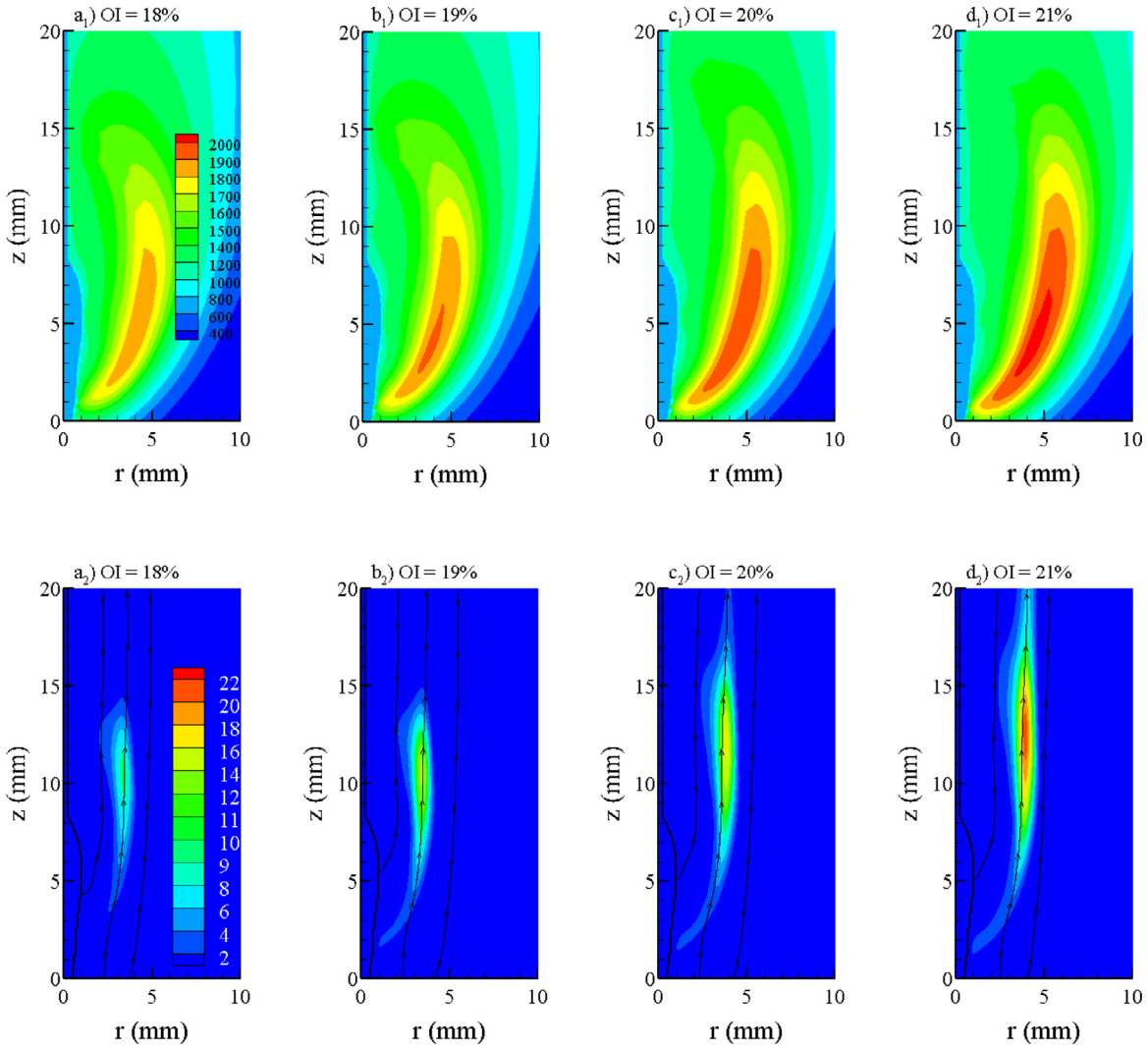

Fig. 4. Computed temperature (index 1, in K) and SVF (index 2, in ppm) fields for a) $X_{O_2} = 18\%$, b) $X_{O_2} = 20\%$, c) $X_{O_2} = 20\%$ and d) $X_{O_2} = 21\%$. Streamlines are plotted with the SVF.

167 (r) × 378 (z) cells using a non-uniform grid. The finest resolution ($76\mu m \times 76\mu$m) is located in a region covering the molten droplet and the sooting region.

5.2. Flame structure

Figure 4 shows the computed temperature and SVF fields for the four flames. As observed experimentally (see Table 1 and Fig. 2), the predicted flame size and the soot production increase with X_{O_2}. As expected, the temperature peak, that is located at vicinity of the flame leading edge, is also enhanced while increasing X_{O_2}. For a given X_{O_2}, the temperature decreases progressively as the distance from the temperature peak is further increased. This cooling process is related, on the one hand, to the radiative losses and, on the other hand, downstream the molten ball, to the heat sink produced by the bare NiCr.

Figure 4 shows clearly that the cooling in the sooting region is enhanced with X_{O_2}, leading to lower and lower temperature at the flame tip. For X_{O_2}=0.20 and 0.21, the SO process at the flame tip is not strong enough to fully oxidize soot that, in accordance with the experimental observations for these oxidizer compositions (see Fig. 2), are partially released into the atmosphere. Streamlines are also plotted along with the fields SVF in the bottom diagrams of Fig. 4. It is interesting to note that the model predicts that, whatever X_{O_2}, the maximum pathline of SVF coincides approximately with a streamline from $z \approx$5–6 mm.

5.3. Flame geometry

The objective of this section is to understand the processes that govern the flame geometry and, in turn, the residence times. The analysis assumes complete combustion that is not fully satisfied for the smoking flames ($X_{O_2} \geq$0.20). However, the amount of smoke released for the present smoking flames does not exceed 5% of the fuel mass flow rate and, therefore, the smoke point transition is expected to have no perceptible influence on the overall trend.

Following the analysis provided by Bhattacharjee et al. for slabs [51] and extended by Konno et al. [52] for cylindrical samples, the luminous flame radius, r_f, is estimated from the oxygen stoichiometric requirement to consume completely the fuel released by pyrolysis:

$$s\dot{m}_P \propto \rho_g u_{0x} \pi r_f^2 Y_{O_{2,\infty}} \tag{7}$$

where s is the stoichiometric oxygen to fuel mass ratio. This expression suggests that r_f varies linearly with $\alpha = \sqrt{s\dot{m}_P/\rho_g u_{0x} Y_{O_{2,\infty}}}$. In the present spreading configurations, the evolution of α while increasing X_{O_2} is governed by two competitive mechanisms: an increase in $\dot{m}_P$ (see Table 1), that tends to enhance α, and an in-

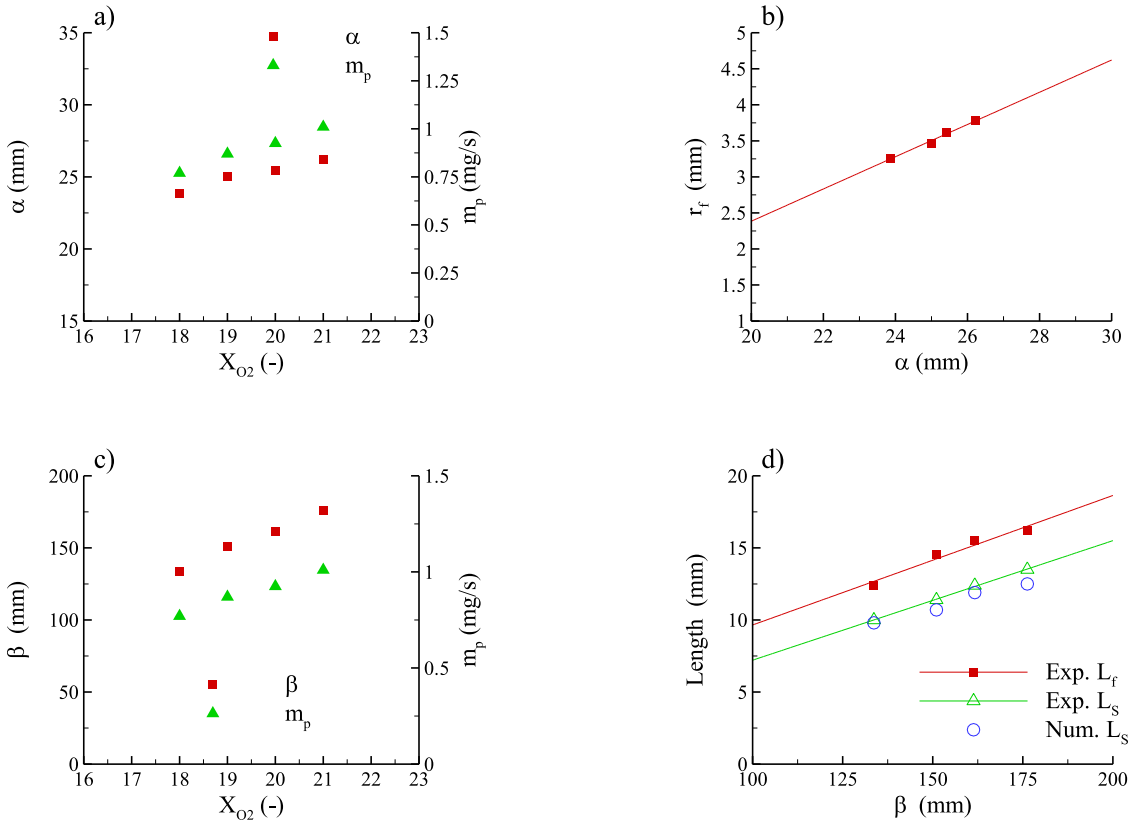

Fig. 5. a) Evolution of α as a function X_{O_2}, b) evolution of experimental r_f as a function of α, c) evolution of β as a function X_{O_2}, and d) evolution of L_f and L_s as a function β.

crease in $Y_{O_{2,\infty}}$, that tends to reduce it. Figure 5a shows that the first mechanism prevails with α increasing with X_{O_2}. Figure 5b confirms the linear dependency of r_f with α.

The analysis of Refs. [51,52] estimates the luminous flame length, L_f, by assuming that the rate of oxygen diffusion towards the fuel equals the stoichiometric amount required for the combustion of the pyrolyzed fuel. In the case of cylindrical samples, this leads to [52]:

$$L_f \propto \beta = \frac{s\dot{m}_P ln\left(r_f/R_{wire}\right)}{\rho_g \alpha_g Y_{O_{2,\infty}}} \tag{8}$$

where R_{wire} is the radius of the cylindrical wire, i.e. 0.55 mm. Similarly to α, the evolution of β as X_{O_2} is enhanced results from a competition between an enhancement in $\dot{m}_P$, that tends to increase β, and an increase in $Y_{O_{2,\infty}}$, that tends to reduce it. As expected, Figs. 5c and d show that the first mechanism prevails and L_f evolves linearly with β, respectively. Figure 5d shows also that both measured and computed L_S increase linearly with β and the slopes of the linear fits are very similar to that of L_f. These results suggest that the luminous flame length can be alternatively considered as characteristic length scale for the SF process in the present flames. In addition, the computed values of L_S agree well with the experimental ones.

5.4. Soot formation and oxidation processes

Figure 6a shows the SVF along the maximum SVF pathline. It increases in the SF region, reaches a peak, and then decreases owing to the SO process. The numerical model captures well the evolution of SVF in both SF and SO region. As discussed previously and in accordance with experimental observations, the model predicts non-smoking flames for X_{O_2} =0.18 and 0.19 and smoking flames for X_{O_2} =0.20 and 0.21. In the SF region, the rates of increase in SVF with z as well as the magnitude of the SVF peaks are well reproduced. In the SO region, the rates of decrease in SVF with z are also well reproduced although the model does not predict the abrupt freezing of the SO process as observed experimentally for the smoking flames and, in turn, underestimates the corresponding amount of soot released into the atmosphere. The present oxidation model based on Eqs. (1) and (2) does not consider aging effects that reduce the soot surface reactivity near the flame tip, which may explain these underestimations [53].

Improvements to account for particle aging were reported in the literature in the case of PAH-based soot production models [53,54]. As discussed in Section 4, such advanced soot models are challenging to be applied to solid fuels and are beyond the scope of the present study. The present numerical results suggest that the model captures the main trends observed experimentally and model predictions can be used to complete the present experimental data.

Let us start to discuss the SF region. Figure 6a shows that the peak location of SVF occurs further downstream as X_{O_2} is enhanced, which results in longer residence time to form soot and partially explains the increase in SVF with X_{O_2}. The evolution of $\dot{\omega}_{SF}$ shows that an enhancement in the SF rate also contributes to this increase (see Fig. 6b). Figure 6a shows that the computed temperature in the SF region follows the same trends as the adiabatic flame temperature, increasing with X_{O_2}. This reinforces the assumption made in Section 4.2.2 that thermal effects control the effects of X_{O_2} on the SF rate and can be related empirically to the adiabatic flame temperature.

Model predictions show that the contribution of OH dominates the SO process along the maximum SVF pathline. Figure 6b shows that $\dot{\omega}_{OH}$ exhibits a non-monotonic behavior with X_{O_2}, increasing

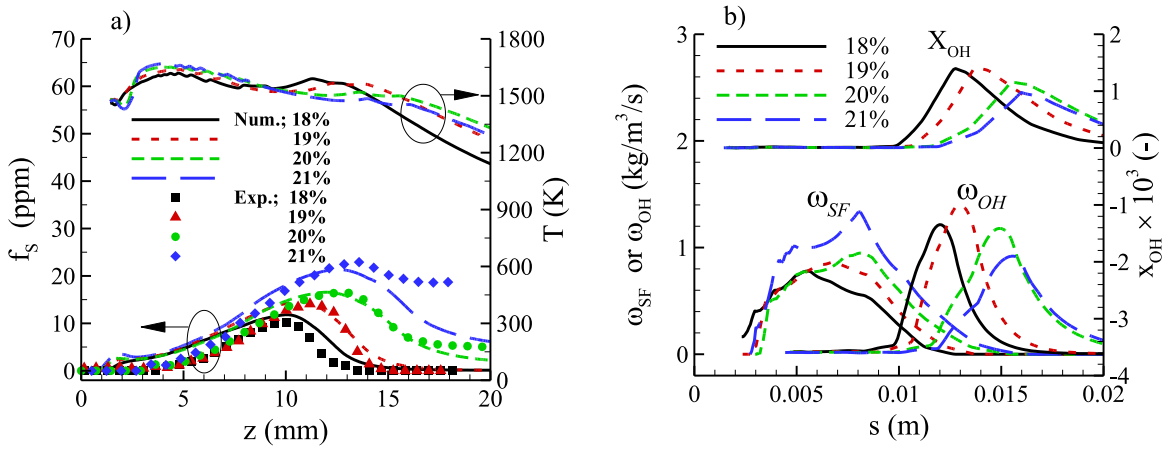

Fig. 6. Evolution along the maximum SVF pathline of a) the experimental and predicted SVF, and the predicted temperature, b) predicted $\dot{\omega}_{SF}$ and $\dot{\omega}_{OH}$, and OH mole fraction. Experimental data are represented by symbols. Numerical results are represented by lines.

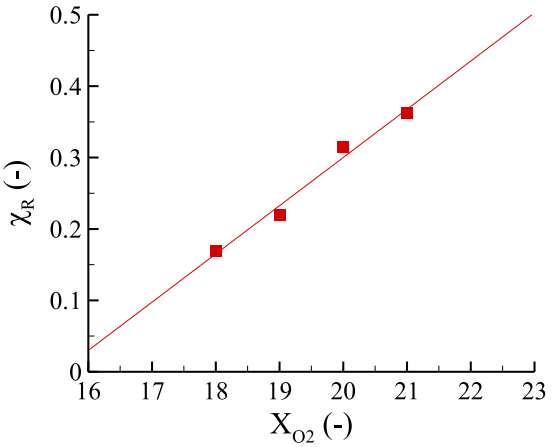

Fig. 7. Computed radiant fraction as a function of X_{O_2}.

first as X_{O_2} is enhanced from 0.18 to 0.19 and, then, decreasing as X_{O_2} is further increased. The previous observations can be then directly related to the effects of increasing X_{O_2} on temperature and OH mole fraction. These effects result from the competition between two mechanisms. On the one hand, oxygen-enhanced oxidizers tend to increase the flame temperature and to promote the formation of OH. On the other hand, Fig. 7 shows that the radiant fraction increases almost linearly with X_{O_2} from about 0.169 for $X_{O_2} = 0.18$ to 0.362 for X_{O_2} =0.21. This increase in radiative losses tends to reduce the temperature in the SO region and to weaken the formation of OH. A detailed examination of Fig. 6 shows that the first mechanism prevails as X_{O_2} is enhanced from 0.18 to 0.19 whereas the second dominates for X_{O_2} =0.20 and 0.21. In particular, it can be observed in Fig. 6 that, in the SO region, the temperature and OH mole fraction become significantly lower and lower as X_{O_2} is increased beyond 0.19.

The experimental SVF in Fig. 6a shows that, for $X_{O_2} = 0.20$ and 0.21, the soot oxidation process freezes at $z = 1.71$ cm and 1.60 cm. At these locations, the corresponding predicted temperatures are of 1451 and 1453 K, respectively. These values stand within the range of 1350–1450 K that corresponds to soot burnout temperature reported in the literature for axisymmetric laminar diffusion flames under different conditions at both normal [34–37] and micro-gravity [24,26]. The smoke point transition occurs for X_{O_2} between 19% and 20%. Figure 7 shows that the corresponding radiant fractions are of 0.23 and 0.30, respectively. These values are in line with recent measurements at normal gravity, which shows smoke point occurs for radiant fractions of about 0.25 for X_{O_2} =19% and 0.28 for X_{O_2} =20% [49].

Figure 8 compares measured and predicted radial profiles of SVF at different z. It should be pointed out that a given location does not necessarily correspond to the same stage in the soot production process for the different flames owing to the different residence times. This figure confirms that model predictions reproduce reasonably the experimental trends in each region of the soot production process. Nevertheless, it can be observed that, for a given z, the computed maximum occurs at higher r and the soot region is shifted downstream as compared to the experiments. These discrepancies become more and more pronounced as the distance along the wire axis increases and can be attributed to the fact that soot evolves parallel to the wire in the simulation (see Fig. 4b) whereas it seems to fall down toward the wire at the stage of the flame trailing edge in the experiments (see Fig. 2). It was observed during the experiments that the flame trailing edge is sensitive to small changes in gravity, which may explain at least partially these discrepancies.

5.5. Effects of X_{O_2} on the radiative feedback to the solid surface

Figure 9 shows that, as expected, the radiative heat flux, $\dot{q}''_{R,inc}$, increases substantially with X_{O_2}. Whatever X_{O_2}, $\dot{q}''_{R,inc}$ increases sharply with z along the molten ball, from values around 1–2 kW/m^2 at the leading edge to reach a peak downstream the ball top. The peak value is strongly enhanced as X_{O_2} increases, from about 9.42 kW/m^2 for X_{O_2} =0.18 to about 15.39 kW/m^2 for X_{O_2} =0.21. $\dot{q}''_{R,inc}$ reaches another maximum value along the bare wire in the region where the flame falls back to the wire. This maximum also increases substantially with X_{O_2}. Figure 9 shows also the radiative flux emitted by the wire surface, $\dot{q}''_{R,w}$. It appears clearly that surface radiative losses dominate the flame radiative feedback in the pyrolysis region and along the bare wire. In the pyrolysis region, $\dot{q}''_{R,w}$ is predicted to be constant due to the assumption of constant pyrolysis temperature. Along the bare wire, it increases to reach a maximum in the region where the flame falls back to the wire. This maximum follows a non-monotonic behavior with X_{O_2}, increasing first as X_{O_2} increases from 18% to 20% and then decreasing slightly as X_{O_2} is increased further to 21%. Finally a careful examination of $\dot{q}''_{R,inc}$ and $\dot{q}''_{R,w}$ shows that the contribution of thermal radiation to the heating process of the solid ahead of the pyrolysis front is negligible whatever X_{O_2}.

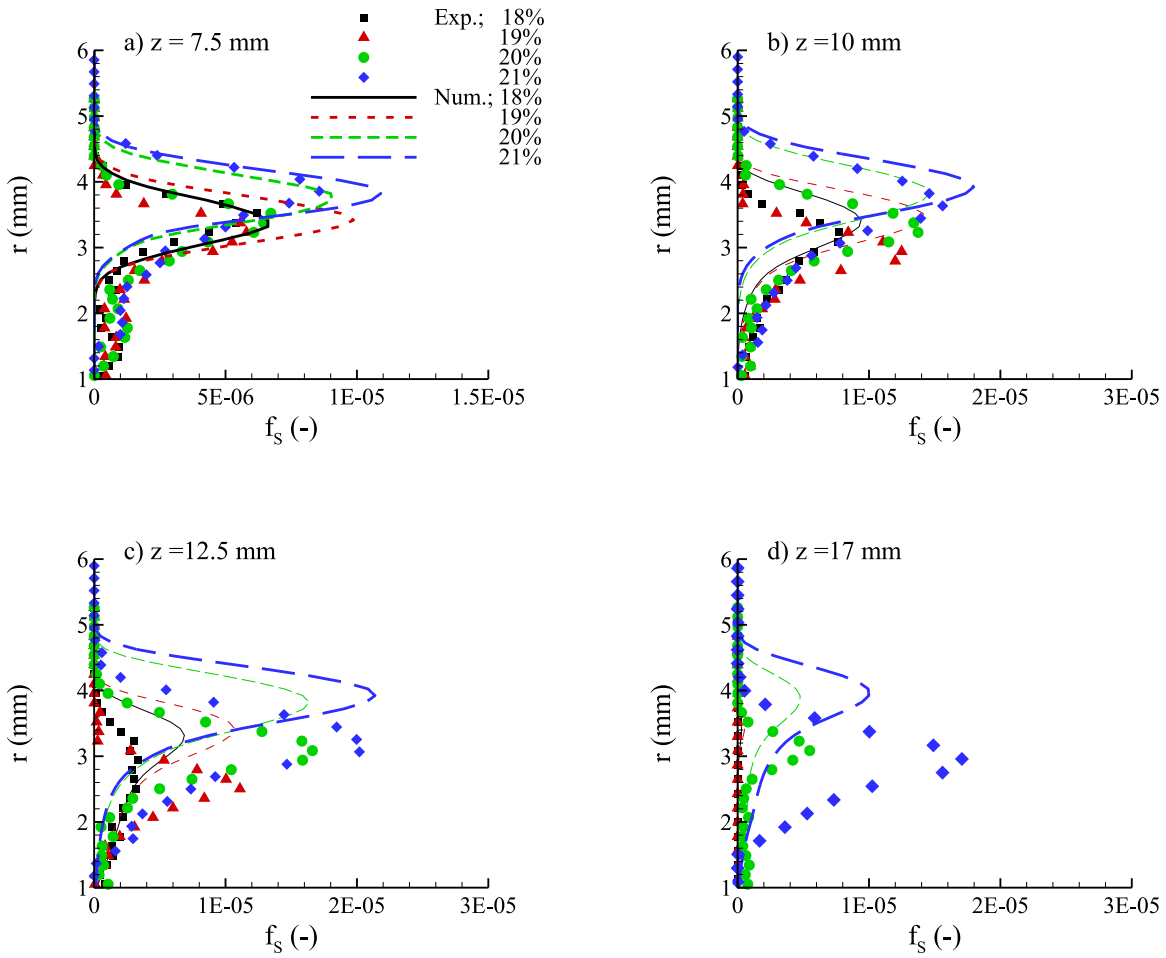

Fig. 8. Radial profiles of SVF at different heights. Experimental data are represented by symbols. Numerical results are represented by lines.

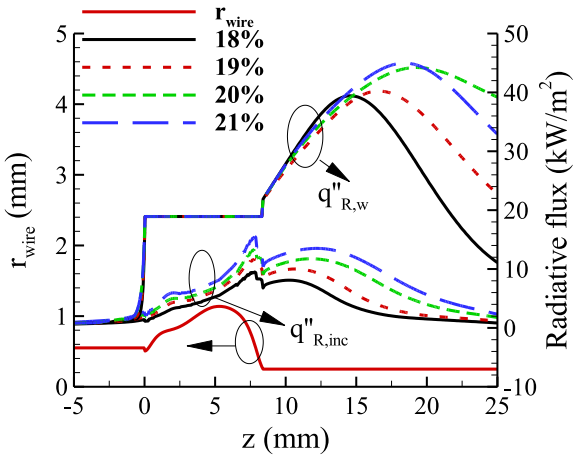

Fig. 9. Incident radiative flux, $q''_{R,inc}$, and surface emission flux, $q''_{R,w}$, along the wire axis (right y-axis). The axial evolution of the wire radius, r_{wire}, is also plotted (left y-axis).

6. Conclusions

Soot production, smoke emission and radiative heat transfer in oxygen-reduced non-buoyant laminar diffusion flames spreading in opposed flow along NiCr wires coated with LDPE are investigated experimentally and numerically. The numerical model considers a detailed chemistry, a state-of-the-art radiation model, and a two-equation soot production model involving a smoke-point soot formation rate and oxidation by OH and O_2.

The following conclusions can be drawn:

1) Experimental data show that spread rate, fuel mass flow rate, flame size, residence time and peak of soot volume fraction increase with X_{O_2}. The flame length and radius and, in turn, the residence time increase with X_{O_2} owing to the increase in the fuel mass flow rates.
2) Analysis of experimental data shows that increasing X_{O_2} enhances the soot formation rate through thermal effects that can be related to the adiabatic flame temperature. Based on these experimental observations, the soot formation rate was scaled by the adiabatic flame temperature to account for X_{O_2} effects.
3) Model predictions are in quantitative agreement with the available experimental data, capturing the effects of X_{O_2} on flame structure, soot formation and oxidation processes. In addition, the model reproduces well the transition from a non-smoking to a smoking flame that occurs for X_{O_2} between 19% and 20%. These results support that the proposed surrogate fuel modeling strategy and the extended soot production model are promising to be applied to other configurations involving solid fuels at both normal and micro-gravity.
4) Increasing X_{O_2} affects the soot oxidation process through two competitive mechanisms. On the one hand, oxygen-enhanced conditions promote the formation of soot oxidizing species. On the other hand, this increases the radiative losses which tends

to lower the temperature and weaken the formation of these species in the soot oxidation region. For the present flames, the first mechanism dominates as X_{O_2} is increased from 18% to 19% whereas the second prevails as X_{O_2} is further increased beyond 19%.

5) The radiant fraction increases with X_{O_2} to reach about 25%−30% at the SP transition. In addition, for the smoking flames, the soot oxidation freezing temperature is found to be about 1450 K. These SP characteristics in terms of radiant fraction and soot oxidation freezing temperature are consistent with those previously reported at normal gravity.
6) The net radiative flux ahead of the pyrolysis front is close to zero whatever X_{O_2}, showing that radiation does not participate to the heating process responsible for flame spread. On the other hand, surface radiative losses dominate the radiative feedback from the flame along the pyrolysis region and the bare wire.

Declaration of Competing Interest

The authors declare that they have no known competing financial interests or personal relationships that could have appeared to influence the work reported in this paper.

Acknowledgments

The authors feel grateful to the centre National d'Etudes Spatiales for its financial support under Contract No. 130615.

References

[1] X. Huang, Y. Nakamura, A review of fundamental combustion phenomena in wire fires, Fire Technol 56 (2020) 315–360.
[2] R. Friedman, Fire safety in spacecraft, Fire Meter. 20 (1996) 35–243.
[3] M. Kikuchi, O. Fujita, K. Ito, A. Sato, T. Sakuraya, Experimental study on flame spread over wire insulation in microgravity, Proc. Combust. Inst. 27 (1998) 2507–2514.
[4] O. Fujita, K. Nishizawa, K. Ito, Effect of low external flow on flame spread over polyethylene-insulated wire in microgravity, Proc. Combust. Inst. 29 (2002) 2545–2552.
[5] W. Kong, B. Wang, W. Zhang, Y. Ai, S. Lao, Study on prefire phenomena of wire insulation at microgravity, Microgravity Sci. Technol. 20 (2008) 107–113.
[6] K. Wang, B. Wang, W. Kong, F. Liu, Study on the pre-ignition temperature variations of wire insulation under overload conditions in microgravity by the functional simulation method, J. Fire Sci. 32 (2014) 257–280.
[7] O. Fujita, T. Kyono, Y. Kido, H. Ito, Y. Nakamura, Ignition of electrical wire insulation with short-term excess electric current in microgravity, Proc. Combust. Inst. 33 (2011) 2617–2623.
[8] S. Takahashi, H. Ito, Y. Nakamura, O. Fujita, Extinction limits of spreading flames over wires in microgravity, Combust. Flame 160 (2013) 1900–1902.
[9] S. Takahashi, H. Takeuchi, H. Ito, Y. Nakamura, O. Fujita, Study on unsteady molten insulation volume change during flame spreading over wire insulation in microgravity, Proc. Combust. Inst. 34 (2013) 2657–2664.
[10] A.F. Osorio, K. Mizutani, C. Fernandez-Pello, O. Fujita, Microgravity flammability limits of ETFE insulated wires exposed to external radiation, Proc. Combust. Inst. 35 (2015) 2683–2689.
[11] M. Nagachi, F. Mitsui, J.M. Citerne, H. Dutilleul, A. Guibaud, G. Jomaas, G. Legros, N. Hashimoto, O. Fujita, Can a spreading flame over electric wire insulation in concurrent flow achieve steady propagation in microgravity? Proc. Combust. Inst. 37 (2019) 4155–4162.
[12] M. Nagachi, J.M. Citerne, H. Dutilleul, A. Guibaud, G. Jomaas, G. Legros, N. Hashimoto, O. Fujita, Effect of ambient pressure on the extinction limit for opposed flame spread over an electrical wire in microgravity, Proc. Combust. Inst. (2000) available online, doi:10.1016/j.proci.2020.05.005.
[13] J.E. Oberg, Star-crossed orbits: Inside the US-Russian Space Alliance, McGraw-Hill Companies, 2002.
[14] G.S. Ivanovich, Salyut-The First Space Station: Triumph and Tragedy, Springer Science & Business Media, 2008.
[15] A.A. Siddiqi, Challenge to Apollo: the Soviet Union and the space race, 1945–1974. NASA History Series, 2000.
[16] S. Garber, Jerry Linenger, Fire and controversy January 12 - May 24, NASA History Program Office, 1997.
[17] P. Baker, The Story of Manned Space Stations: An Introduction, Springer Science & Business Media, 2007.
[18] J.M. Linenger, Off the planet: Surviving Five Perilous Months Aboard the Space Station Mir, McGraw-Hill USA, 2000.
[19] M.E. Meyer, D.L. Urban, G.W. Mulholland, V. Bryg, Z.G. Yuan, G.A. Ruff, T. Cleary, J. Yang, Evaluation of spacecraft smoke detector performance in the low-gravity environment, Fire Safety J 98 (2018) 74–81.
[20] X. Wang, H. Zhou, W.P. Arnott, M.E. Meyer, S. Taylor, H. Firouzkouhi, H. Moosmüller, J.C. Chow, J.G. Watson, Characterization of smoke for spacecraft fire safety, J. Aerosol Sci. 136 (2019) 36–47.
[21] P.S. Greenberg, K.R. Sacksteder, T. Kashiwagi, Wire insulation flammability experiment, NASA CP (2005), p. 3272.
[22] A. Guibaud, J.M. Citerne, J.L. Consalvi, O. Fujita, J. Torero, G. Legros, Experimental evaluation of flame radiative feedback: methodology and application to opposed flame spread over coated wires in microgravity, Fire Technol. 56 (2020) 185–207.
[23] A. Guibaud, J.M. Citerne, J.L. Consalvi, G. Legros, On the effects of opposed flow conditions on non-buoyant flames spreading over polyethylene-coated wires – Part I: spread rate and soot production, Combust. Flame 221 (2020) 530–543.
[24] A. Guibaud, J.M. Citerne, J.L. Consalvi, G. Legros, On the effects of opposed flow conditions on non-buoyant flames spreading over polyethylene-coated wires – Part II: soot oxidation quenching and smoke release, Combust. Flame 221 (2020) 544–551.
[25] A. Guibaud, J.L. Consalvi, J.M. Orlac'h, J.M. Citerne, G. Legros, Soot production and radiative heat transfer in opposed flame spread over a polyethylene insulated wire in microgravity, Fire Technol 56 (2020) 287–314.
[26] A. Guibaud, J.L. Consalvi, J.M. Citerne, G. Legros, Pressure effects on the soot production and radiative heat transfer of non-buoyant laminar diffusion flames spreading in opposed flow over insulated wires, Combust. Flame 222 (2020) 383–391.
[27] A. Guibaud, J.M. Citerne, J.M. Orlac'h, O. Fujita, J.L. Consalvi, J.L. Torero, G. Legros, Broadband modulated absorption/emission technique to probe sooting flames: implementation, validation, and limitations, Proc. Combust. Inst. 37 (2019) 3959–3966.
[28] Y. Zhang, M. Kim, P.B. Sunderland, J.G. Quintiere, J. de Ris, A burner to emulate condensed phase fuels, Exper. Thermal Fluid Sci. 73 (2016) 87–93.
[29] A. Markan, P.B. Sunderland, J.G. Quintiere, J.L. de Ris, D.P. Stocker, H.R. Baum, A burning rate emulator (BRE) for study of condensed fuel burning in microgravity, Combust. Flame 192 (2018) 272–282.
[30] C.W. Lautenberger, J.L. de Ris, N. Dembsey, J.R. Barnett, H.R. Baum, A simplified model for soot formation and oxidation in CFD simulation of non-premixed hydrocarbon flames, Fire Safety J. 40 (2005) 141–176.
[31] P. Chatterjee, D. Zeng, Y. Wang, Numerical modeling of soot radiation in optically-thin, buoyant diffusion flames at varying oxygen concentrations, Proc. Combust. Inst. (2020) available online, doi:10.1016/j.proci.2020.08.028.
[32] J.L. de Ris, P.K. Wu, G. Heskestad, Radiation fire modelling, Proc. Combust. Inst. 28 (2000) 2751–2759.
[33] H. Guo, P.M. Anderson, P.B. Sunderland, Optimized rate expressions for soot oxidation by OH and O_2, Fuel 172 (2016) 248–252.
[34] G.H. Markstein, Relationship between smoke point and radiant emission from buoyant turbulent and laminar diffusion flames, Proc. Combust. Inst. 20 (1984) 1055–1061.
[35] G.H. Markstein, J. de Ris, Radiant emission and absorption by ethylene and propylene diffusion flames, Proc. Combust. Inst. 20 (1984) 1637–1646.
[36] J.H. Kent, H.G. Wagner, Why do diffusion flames emit smoke? Combust. Sci. Technol. 41 (1984) 245–269.
[37] J. Bonnety, A. Guibaud, R. Jalain, A. Matynia, J.L. Consalvi, F. Liu, G. Legros, Probing the local radiative quenching during the transition from a non-smoking to a smoking laminar coflow ethylene/air non-premixed flame, Combust. Flame 203 (2019) 120–129.
[38] R. Friedman, NASA Technical Reports 19940022933, 1994.
[39] P.S. Greenberg, K.R. Sacksteder, T. Kashiwagi, Wire insulation flammability experiment: USML-1 one year post mission summary, NASA Shuttle Mission Summary, 1994.
[40] M.M. Khan, A. Tewarson, M. Chaos M, Combustion characteristics of materials and generation of fire products, in: MJ Hurley (Ed.), SFPE Handbook of Fire Protection Engineering, 5th Edition, Springer, New York (2016), pp. 1143–1232.
[41] Z. Qin, V.V. Lissianski, H. Yang, W.C. Gardiner, S.G. Scott, H. Wang, Combustion chemistry of propane: a case study of detailed reaction mechanism optimization, Proc. Combust. Inst. 28 (2000) 1663–1669.
[42] The National Institute of Advanced Industrial Science and Technology, available at http://riodb.ibase.aist.go.jp/ptdb/entarupi.htm.
[43] M.F. Modest, R.J. Riazzi, Assembly full spectrum k-distribution from a narrow band database: effects of mixing gases, gases and non-gray absorbing particles and non-gray scatters in non-gray enclosures, J. Quant. Spectrosc. Radiat. Transf. 90 (2005) 169–189.
[44] E.H. Chui, G.D. Raithby, P.M.J. Hughes, Prediction of radiative transfer in cylindrical enclosures with the finite volume method, AIAA J. Thermophys. Heat Transf. 6 (1992) 605–611.
[45] R.P. Lindstedt, Simplified Soot Nucleation and Surface Growth Steps For Non-Premixed flames, in Soot Formation in Combustion, H. Bockhorn, ed., Springer-Verlag, Berlin, 1994, 417–441.
[46] Z. Sun, B. Dally, Z. Alwahabi, G. Nathan, The effect of oxygen concentration in the co-flow of laminar ethylene diffusion flames, Combust. Flame 211 (2020) 96–111.
[47] A. Fuentes, R. Henríquez, F. Nmira, F. Liu, J.L. Consalvi, Experimental and numerical study of the effects of the oxygen index on the radiation characteristics of laminar coflow diffusion flames, Combust. Flame 160 (2013) 786–795.

[48] A. Jerez, J.L. Consalvi, A. Fuentes, F. Liu, R. Demarco, Soot production modeling in a laminar coflow ethylene diffusion flame at different Oxygen Indices using a PAH-based sectional model, Fuel 231 (2018) 404–416.
[49] D. Zeng, G. Xiong, Y. Wang, Effect of oxygen environment on soot characteristics in ethylene diffusion flames, Proc. of the Ninth Int. Seminar on Fire and Explosion Hazards, Saint Petersburg, Russia (2019), pp. 21–26. April.
[50] F.G. Roper, C. Smith, A.C. Cunningham, The prediction of laminar jet diffusion flame sizes: part II. Experimental verification, Combust Flame 29 (1977) 227–234.
[51] S. Bhattacharjee, S. Takahashi, K. Wakai, C.P. Paolini, Correlating flame geometry in opposed-flow flame spread over thin fuels, Proc. Combust. Inst. 33 (2011) 2465–2472.
[52] Y. Konno, N. Hashimoto, O. Fujita, Downward flame spreading over electric wire under various oxygen concentrations, Proc. Combust. Inst. 37 (2019) 3817–3824.
[53] A. Khosousi, S.B. Dworkin, Detailed modelling of soot oxidation by O_2 and OH in laminar diffusion flames, Proc. Combust. Inst. 35 (2015) 1903–1910.
[54] A. Khosousi, S.B. Dworkin, Soot surface reactivity during surface growth and oxidation in laminar diffusion flames, Combust. Flame 162 (2015) 4523–4532.

Effects of flame retardants on extinction limits, spread rate, and smoke release in opposed-flow flame spread over thin cylindrical polyethylene samples in microgravity

Y. Li[a,*], A. Guibaud[b], J.-M. Citerne[a], J.-L. Consalvi[c], A. Coimbra[c]
J. Sarazin[d], S. Bourbigot[d,e], J.L. Torero[b], G. Legros[a]

[a] *Institut Jean Le Rond d'Alembert/UMR CNRS 7190, Sorbonne Université, Paris F-75005, France*
[b] *Department of Civil, Environmental and Geomatic Engineering, University College London, London WC1E6BT, UK*
[c] *Aix-Marseille Université, CNRS, IUSTI UMR 7343, 5 rue E. Fermi, 13013 Marseille, France*
[d] *Université de Lille, CNRS, INRAE, Centrale Lille, UMR 8207 – Unité Matériaux et Transformations, F-59000, Lille, France*
[e] *Institut Universitaire de France (IUF), Paris, France*

Abstract

Though flame retardants are considered for use in spacecraft, their performances in microgravity are still poorly understood. To assess their effects on flame extinction, opposed flame spread rate, and smoke emission in the absence of buoyant flows, thin cylindrical samples of Low Density Polyethylene (LDPE) loaded with intumescent flame retardants are ignited in parabolic flights. Two types of flame retardants characterized by different mechanisms of intumescence are considered, namely Expandable Graphite, (EG), and Ammonium polyphosphate / Pentaerythritol, (AP), for which thermal stress and chemical recombination drive physical expansion, respectively. Observations are then reported and contrasted with results obtained at normal gravity for different flame retardant loads, under varying oxygen content at given ambient pressure and flow velocity. Focusing on the flame leading edge, results related to flame spread and flame extinction are analyzed first. At normal gravity, increasing the flame retardant load improves fire safety through an increase in the flame extinction limit on the one hand, and a reduction in the average flame spread rate for all oxygen contents studied on the other hand. In contrast, results in microgravity show no modification in the extinction limit over the range of flame retardant loads studied, and the benefits in average flame spread rate reduction are less pronounced. Investigating then radiative quenching at the flame trailing edge, smoke emission is never evidenced at normal gravity. However, in microgravity, the addition of flame retardants increases the range of conditions leading to smoke emission, which is detrimental to fire safety. These observations are valid for both flame retardants, yet more pronounced for EG-loaded samples than AP-loaded samples. These ambivalent effects on fire safety of AP and EG addition in microgravity, which are not evidenced at normal gravity, call for a cautious integration of flame retardants in the scope of space exploration.

Keywords: Flame retardant; Microgravity; Flame spread; Extinction limits; Smoke emission

1. Introduction

Fire safety has been identified as one of the most important issues that must be properly resolved in manned spaceflight [1], since an accidental fire can jeopardize the missions and even pose a threat to the health and life safety of astronauts in the worst-case scenarios. With the increase in both distance and duration of space travel in the context of lunar habitats development or deep space exploration ambitions, fire safety issues are twofold. From a technological perspective, the existing fire strategies designed for low earth orbit spacecraft rely on the possibility to conduct fast resupply missions after minor fire incidents, or to perform short-range emergency evacuations if the situation deteriorates. Unfortunately, both options are not accessible beyond Earth's orbit. From a fundamental perspective, the dramatic impact of reduced gravity on material flammability, ignition conditions, flame spread, fire growth, and smoke emission through modifications in heat and mass transfer is still not fully understood and remains an active topic of academic research [2, 3]. Thus, to develop relevant fire strategies in the absence of buoyancy, these fire safety aspects are being studied over a range of materials, e.g. composite cotton fabric [4], PMMA [5], and polyethylene [6], and over geometries such as flat sheets [7] and cylinders [8] to create a comprehensive base of knowledge for further investigations.
Cylindrical Low-Density PolyEthylene (LDPE) is one of the most studied configurations, and can thus be used as a baseline material to expand our knowledge in this field. It has been found that the probability of ignition of LDPE is significantly increased in microgravity conditions as compared with a standard gravity level [9]. In addition, as buoyant flows disappear, a flame can spread over these samples under low oxygen content conditions that would lead to flame self-extinction at normal gravity [10]. Moreover, more intense smoke production is reported in the absence of buoyancy [11] owing to increased radiative losses from sootier flames [12], which is consistent with observations from a major past incident aboard the Mir Space Station [13]. All these observations suggest an increased danger in the confined environment of a spacecraft.
Though leading aspects of combustion are modified in microgravity, the associated fire safety concerns are not specific to space exploration. As such, inspiration can be found in existing solutions from other industries. For instance, flame resistant or flame retardant materials are commonly employed in construction, transport, cable, or textile industries to improve fire safety, and should be considered in spacecraft design as well. Flame resistant fabrics are made from materials that inherently have low flammability properties, while flame retardant fabrics have been modified by chemical coating or inclusion and thermal treatments to improve on their original behavior.
Concerning flame resistant materials, Orndoff summarized the successful development of several fabrics for space exploration by textile industries since the 1960s, like polybenzimidazole fibers, aromatic polyamide fibers, chlorofluoroethylene fibers, polyimide fibers, and beta fiberglass [14]. These materials could eventually pass flammability tests on the ground to assess their viability in an oxygen-enriched atmosphere (beta fiberglass for instance was designed to be non-flammable in the pure oxygen environment of a spacesuit), and were included in the design of successive spacecraft. However, the tests were not performed in the absence of buoyancy, so it is not known whether these flame retardant fabrics perform in microgravity as well as they do at normal gravity. In addition, their prohibitive cost and limited range of applications hampers a sustainable production. Investigating the difference caused by buoyancy, Takahashi et al. compared flammability of other more common flame resistant materials, such as NOMEX, Kevlar, Kapton, CARBOGLASS, PEEK, PPSU, silicone resin, and silicone rubber, under both normal and micro-gravity [15, 16]. They found that, among these materials, those with higher pyrolysis temperatures inhibit flame spread in microgravity and can self-extinguish under higher oxygen content than observed at normal gravity. Because they are inherently designed for specific fire needs, flame resistant materials may poorly address other functional requirements vital to space travel [14].
As such, research on flame retardant materials has also received a special focus to boost the fire properties of existing materials used in spacecraft at a limited development cost. To protect spacecraft and astronauts following the catastrophic 1967 Apollo 1 fire, Parker et al. [17] considered enhancing the fire resistance properties of polymeric materials by adding flame retardant coatings (nitroanailine-sulfonic acids, quinonedioxime-acid mixtures, and nitroanilinosulfones). The nitroanailine-sulfonic acids coating had been tested for its effectiveness in protecting a structure from the fire on the ground and it was shown that the temperature of the coated sample increased five times slower than in the absence of coating. With the same purpose, Kourtides et al. [18] conducted experiments on composite materials loaded with flame retardants (graphite-reinforced composites) on the ground. They found that the loaded samples showed a higher limiting oxygen index (LOI), lower heat release rate, and lower smoke production. These two reports aside, there is a lack of measurements regarding the efficiency of flame retardants in the context of space exploration, amplified by the absence of data in reduced gravity.
In this context, a broad range of flame retardants can be investigated. Intumescent flame retardants, which expand when exposed to external heating while retaining acceptable mechanical properties, are especially relevant in polymer materials increasingly used in spacecraft. In the presence of a flame, an expanded char layer can be formed, inhibiting fire spread by slowing down heat and mass transfer between the gas and condensed phases [19]. Intumescence can

be obtained from a series of chemical reactions or using mechanical expansion. Ammonium polyphosphate/pentaerythritol (AP) is a system consisting of ammonium polyphosphate (APP) and PentaERythritol (PER), producing intumescence via a series of chemical reactions. Under the action of external heat flux, APP decomposes and yields acidic phosphates acting as char promoters. Phosphates react with PER to yield char which can expand to a porous char layer, thanks to the evolution of ammonia from APP and the decomposition products of the burning material [20]. Therefore, the post-combustion AP residue is an expanded carbonaceous char, acting as a heat barrier. Its internal structure is foamy with small and large voids. The cohesion of the structure is relatively high. Comparatively, Expandable Graphite (EG) is a typical example of intumescent flame retardant that follows a mechanical process. Insertion compounds are contained between the graphite layers and upon heating EG expands: the intercalation compound quickly decomposes into gaseous products, thereby exposing the graphite flakes which then form an entangled network of worm-like structures on the surface of the loaded material. This network acts as a protective layer that expands under the rapid sublimation of molecules in the polymeric matrix [21, 22]. It should be noted that the cohesion of the structure is high enough to provide the protection of interest but it is not strong to resist the fluid flow or other erosion forces. The structure difference between AP and EG could lead to a different mass transfer of gaseous fuel to the flame. An image of the AP and EG residues after combustion is provided as supplementary material to show the difference in their structure.

To investigate the influence of different flame retardants on flame spread at both normal and microgravity, this paper investigates the consequences of AP and EG addition to standard samples. Many of the results depend on the particular configuration. That being said, the axisymmetric configuration gives access to a relatively simple topology of the flow field and the opposed flow feature leads to a minimal still relevant interaction between the flame and the condensed phase. As a result, the configuration investigated is believed to offer a fine compromise between applied challenges and fundamental ambitions for the specific study of flame retardants and especially their influence on the condensed phase. Therefore, thin cylindrical samples of LDPE are used as a baseline, to build on the existing literature with uni-directional flame spread. Experiments are then performed on the ground and in parabolic flights to study the extinction limit, the average flame spread rate, and smoke emission in the opposed-flow configuration, under varying oxygen content.

2. Methodology

2.1. Experimental setup

All experiments at normal and micro-gravity are conducted on the Detection of Ignition And Mitigation Onboard for Non-Damaged Spacecrafts (DIAMONDS) rig, extensively detailed in Refs. [23–25]. To conduct microgravity experiments, DIAMONDS is installed aboard Novespace A310 ZeroG aircraft which performs parabolic flights. Each parabola provides 22 seconds of microgravity, with an absolute residual acceleration below $5 \times 10^{-2} \mathrm{g}_0$.

Briefly, DIAMONDS features a cylindrical combustion chamber with an internal diameter of 190mm where a laminar flow of controlled oxygen content, pressure, and velocity is established. The ranges of controlled oxygen content, ambient pressure level and flow velocity are 0% to 21% in volume, 50 kPa to 150 kPa, and 0 to 300mm/s, respectively. In the following, the flow velocity and the pressure are set at 150mm/s and 101.3 kPa, respectively, and the oxygen content is investigated from 17 to 21%. The samples studied are LDPE cylinders, potentially loaded with intumescent flame retardants. The samples are 100mm long, with a diameter of 2mm. Unlike previously studied samples [23], they do not feature a metallic core that affects both heat transfer and the integrity of the condensed phase as the flame propagates. The sample, located at the center of the combustion chamber along its axis, is ignited without contact using a hot incandescent Kanthal wire. A 14.2V current flows for 8s in the Kanthal wire as the aircraft enters its parabolic trajectory, regardless of whether ignition happens or not. Since the present study on the flame retardant sample is based on the opposed-flow flame spread, the coil is placed at the upstream end of the samples.

Once the sample is ignited, the flame propagation is recorded by a JAI AT-140CL digital 12-bit tri-CCD camera. This camera, equipped with a telecentric lens, images the incoming light over red, green, and blue 521x1396 pixel^2 CCD arrays with a spatial resolution of 72.6μm at a rate of 39fps. At the back of the sample, uniform backlighting produced by a set of adjustable RGBW LEDs is alternatively set on and off during the images recording. The solid fuel surface can be observed on the backlighted images to investigate the intumescence produced by the different types of flame retardant. In addition, the backlight allows discrimination between smoking and non-smoking conditions through observation of absorption at the flame trailing edge. Besides, a 640x480 VIM 640 G2 ULC Infrared camera with a working spectral range from 8μm to 14μm, a resolution of 86μm, and a frame rate of 30fps has been added along the direction perpendicular to the line-of-sight of the tri-CCD camera. This additional camera measures the infrared energy emitted from the surface of samples through a polished germanium window with a transmission spectrum between 2μm and 14μm. Moreover, a passively athermalized infrared lens is mounted in order to block the infrared signal in a spectral band from 8μm to 12μm.

Observations are carried out 15 to 25 seconds after ignition. This allows the flame to spread away from the

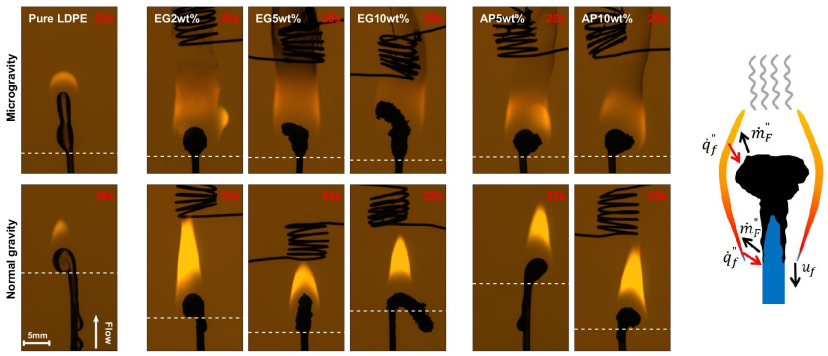

Fig. 1: Backlighted frames imaging opposed-flow flame spread over cylindrical LDPE samples (left) and schematic of the degradation process (right). All observations are carried out at a pressure of 101.3 kPa, under an oxygen content of 21% and a flow velocity of 150 mm/s, to observe the impact of gravity and both AP and EG flame retardants with varying weight contents. The images are taken 15s after ignition, shortly before the end of the flame spread. The time since ignition is indicated in the upper right corner of every frame. The position of the upstream condensed phase deformation is indicated by a dashed line.

igniter and reduce undesired interactions while making sure flame spread is analyzed in the steady microgravity phase of the parabola.

2.2. Samples manufacturing process

LDPE was supplied by Sabic (Netherlands) in the commercial grade Sabic® LDPE 2602X1 00900. EG is the commercial grade ES350F5 from Graphitwerk Kropfmühl (Germany) with an average particle size of 300 µm. Sulfate was used in this grade as an intercalation compound to make graphite bisulfate. APP is the commercial grade of Clariant (Germany) with the brand name Exolit AP422. PER was supplied by Aldrich.

LDPE was blended with flame retardants in a twin-screw extruder. The total loading of flame retardants in LDPE varied from 2 to 10 wt% of EG and at 5 and 10 wt% for APP/PER with the ratio 3:1 (wt/wt) and hereafter called AP. Compounding was performed using HAAKE Rheomix OS PTW 16 twin-screw extruder. The extruder is a co-rotating intermeshing twin screw with a barrel length of 400 mm and a screw diameter of 16 mm (L/D = 25) with 10 zones. LDPE and flame retardants were incorporated using two gravimetric side feeders into the extruder. The polymer flow rate is fixed to extrude about 500 g/h with a screw speed of 300 rpm.

Since the purpose of the present study is to observe the influence of flame retardant on flame spread from 17 to 21% oxygen content, the flame retardant loading needs to be adjusted to adapt to the general requirements. Here, flame retardants are incorporated into the LDPE solid phase, with proportions of 2wt%, 5wt%, and 10wt% for EG, and 5wt%, 10wt% for AP. To provide a baseline, pure LDPE samples are also investigated.

3. Results and discussion

3.1. Initial observation

Figure 1 displays backlighted observations of samples at normal and micro-gravity, with various flame retardant contents, at a set oxygen content of 21%.

The expansion linked to the intumescent processes is clearly visible in microgravity, as illustrated in Fig. 1. AP loaded samples feature a globally spherical shape in the pyrolyzing region with a size independent of the loading. Yet, this region is larger in microgravity than at normal gravity. In contrast, the intumescent region of EG-loaded samples increases in size with the EG loading, moving from a spherical shape towards a more cylindrical structure. As the expanded carbon layers accumulate, the intumescent region severely bents, and even drops under its own weight at normal gravity, affecting the protection of the unburnt upstream part. Ahead of the intumescent region, dripping is also recorded at normal gravity and increases as the content of flame retardant decreases.

Over pure LDPE samples, a strong dripping process is observed. At normal gravity, the intense dripping carries most of the molten fuel away, leading to a short flame length. The dripping occurs due to the effect of gravitational force on the accumulated molten droplet generated by the pyrolysis process of LDPE. It has been observed that the dripping also occurs with a sample at low flame retardant loading (e.g. EG2wt% and AP5wt%), but as the loading continues to increase, the dripping is reduced. In microgravity, a complex motion of twin droplets is observed ahead of the flame. The droplets regularly merge and separate as the flame spreads, with no correlation to the residual gravity, evidencing competing flow mechanisms in the molten phase.

Over flame retardant-loaded samples, the luminosity of the flame does not significantly change at a set gravity level, in spite of the severe modifications in the condensed phase with the increased intumescent load. However, as the flame retardant load increases, the flame seems to be more stable, with weaker flickering. At normal gravity, the flame is bright and stretched, while it is wider and less luminous in mi-

crogravity. This points to an increased residence time and a lower local soot temperature, which promotes quenching at the flame trailing edge. A dark trail of smoke is systematically observed over flame retardant-loaded samples in microgravity, though it was not reported over the pure LDPE samples. As such, EG and AP seem to promote quenching, which results in increased atmospheric contamination. This illustrates the need for systematic characterization of flame retardant performance in the absence of buoyant flows, as increased smoke production questions their efficiency.

A schematic is shown in Fig. 1 to further analyze the mechanism of flame retardants affecting the flame spread. The heat flux, $\dot{q}''_f$, from the flame to the sample surface is transferred to the unburned zone at the leading edge of the flame, and the addition of flame retardants slows down the local pyrolysis rate $\dot{m}''_F$ of the solid fuel. This influences the overall pyrolysis rate $\dot{m}_F$, therefore the flame spread rate, u_f, as shown by Eq. (1), and potentially stops the flame spreading. In addition, the intumescent region also blocks a part of the heat, $\dot{q}''_f$, which weakens the pyrolysis process and contributes to the mitigation of the flame spread. The gaseous fuel supplied by the pyrolysis needs to flow through the intumescent region to reach the trailing edge of the flame, and this process tends to increase the residence time, which favors soot production in the flame, thus increasing the hazard of smoke emission.

3.2. Extinction limits

Flame propagation and self-extinction are investigated first and reported in Fig. 2. Since the igniter provides a large external heat flux in the first few seconds of each experiment, a visible flame appears systematically. During the observation period, if combustion is not self-sustained, the flame gets smaller and less luminous until it eventually quenches at its leading edge, then releasing a significant amount of unburnt pyrolysis gases and possibly soot particles which are visible through backlight attenuation. Such a situation is regarded as extinction [26]. The infrared camera provides additional clues regarding the surface temperature evolution. If combustion is sustained at the flame leading edge and the flame spreads, a pyrolysis region of uniform and stable temperature is recorded. In an extinction situation, the infrared signal gradually drops, starting from the upstream preheating region, as heat loss mechanisms dominate in the condensed phase. The infrared signal collects quantitative information ahead of the potential visible flame extinction, thus increasing confidence in the discrimination of spread and extinction situations within the limited observation period.

Under normal gravity conditions, flame retardants have a noticeable impact on flame extinction. Under the pressure and flow velocity conditions studied, the LOI is raised from 18% for the pure LDPE sample to 19% for both EG- and AP-loaded samples, and is even increased to 21% for 10wt% AP-loaded samples. Increasing the EG load does not show any significant effect on flame extinction. This is interpreted as a consequence of the increase in intumescence volume, which triggers subsequent bending and falling off of the expanded carbon layer under the influence of gravity. As this protective thermal insulation layer is removed, the virgin fuel is exposed to the flame heat flux, which promotes pyrolysis and cancels the benefits of increased EG loading. On the other hand, the increase in AP loading results in a higher LOI since the more compact intumescent volume never detaches from the fuel surface, thus retaining its protective function. Unlike normal gravity observations, no shift in LOI was reported in microgravity for both flame retardants regardless of the loading. The flames could spread at 18% oxygen content, the LOI for the pure LDPE sample, in spite of the visible intumescence (see Fig. 1). As such, the intumescence does not improve on the ex-

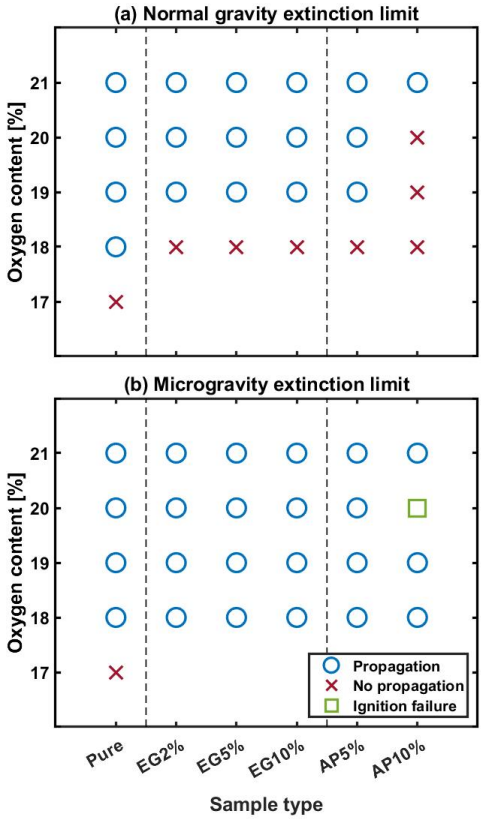

Fig. 2: Effect of oxygen content on flame spread and extinction over LDPE samples loaded with various flame retardant contents under (a) normal and (b) micro-gravity conditions. The noticeable impact of flame retardants on extinction at normal gravity disappears in microgravity.

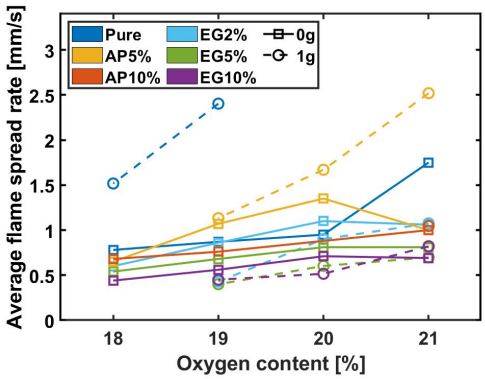

Fig. 3: Effect of oxygen content on average flame spread rate at normal and micro-gravity. Each color corresponds to a type of sample and two different markers represent two different gravity levels. Flame retardants hinder the spread of flame at both normal and micro-gravity. The associated uncertainties extracted from the measurement of the pyrolysis position and the frame rate of the camera are lower than 2.5% of the average flame spread rate (see the supplementary material for the set of estimated values).

tinction limit of the studied material under the investigated conditions. This lack of correspondence between normal and micro-gravity observations is particularly problematic as present spacecraft material flammability tests performed on the ground rely on self-extinction criteria [27]. A possible explanation is that the intumescent matrix acts as a porous media in the condensed phase, driving the molten fuel towards the flame through capillarity. This mechanism is shrouded by dripping at normal gravity but dominates the viscous flow in microgravity. In addition, the absence of natural convection prevents blow off at the flame leading edge from the increased buoyancy induced air velocity, as the Damkohler number is increased in microgravity [28].

3.3. Average flame spread rate

The steadiness of spread rate for a given sample and flow condition is evaluated based on the steadiness of the flame length, of the droplet volume, and of the velocity of the flame front position over the period of interest [25]. In all studied conditions, the flame length and the droplet volume continuously increase, so no condition can be considered as a steady flame spread. An average flame spread rate is then estimated by averaging the displacement of the pyrolysis front over the 10s of observation, with the pyrolysis front being defined as the upstream deformation position of the condensed phase (see Fig. 1).

The average flame spread rate at normal gravity and microgravity is plotted as a function of the oxygen content in Fig. 3. It should be pointed out that the pure LDPE results at normal gravity under 20 and 21% oxygen content are not reported, because the sample was fully consumed before the end of the observation period. Still, the average flame spread rate for these two conditions can be considered higher than all the other ones. Overall, the average flame spread rate increases with the oxygen content, for all flame retardant types and loads, and under both normal and micro-gravity conditions. This is expected as the increased flame temperature enhances the heat transfers to the sample surface.

At normal gravity and at a set oxygen content, the average flame spread rate decreases when increasing EG and AP flame retardants loads. In the absence of flame retardant in microgravity, the samples have a tendency to release two droplets upstream of the flame (see Fig. 1 bottom left), which slows down the propagation as the molten fuel cools down upstream of the flame, thus increasing heat losses. As flame retardant is added, this process is not observed anymore, which increases the flame spread rate for the lowest flame retardant loadings (EG2wt% and AP5wt%) compared to the pure LDPE situation. Yet, as the loading is further increased, a reduction in spread rate is observed. Comparing the amplitude of flame spread rate, higher flame retardant loading is required in microgravity to reduce the spread rate to an extent similar to normal gravity observations, where the slowest spread rates are reported. It is interesting that the EG-loaded sample tends to provide a higher flame spread rate in microgravity than at normal gravity. The main reason may be associated with the dripping effect. At normal gravity, the increase in EG loading is correlated with a reduced dripping rate. Different effects may contribute to this trend. Among others, the enhanced rugosity associated with the intumescent material, and more specifically the worms formed with EG addition (see the supplementary material), increases the adherence of the molten droplet at the contact location. As a result, the deceleration of the flame spread with EG loading is significant at normal gravity. In addition, the above trend leads to a certain collapse of the molten droplet formation phenomenology for normal and micro-gravity conditions. However, at normal gravity, the heat of the flame is transferred downstream of the flame especially by the buoyant flow, which reduces the heat transferred upstream, therefore weakening the pyrolysis process. The latest trend can then explain the lower spread rate at normal gravity as compared to that in microgravity as EG loading significantly affects the spread.

Overall, the EG-loaded samples spread more slowly than the AP-loaded samples for the same flame retardant load, under both normal and micro-gravity conditions.

3.4. Smoke emission

In spreading situation where the flame does not quench at the leading edge, local extinction can still take place at the trailing edge, leading to contamination of the surrounding atmosphere. The tendency of the flame to emit smoke can be simply evaluated us-

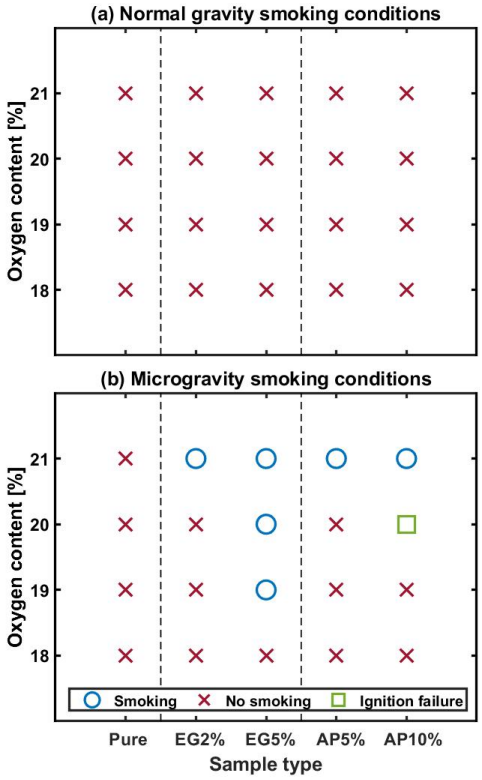

Fig. 4: Effect of oxygen content on smoke emission over LDPE samples loaded with various flame retardant contents under (a) normal and (b) micro-gravity conditions. Flame retardants promote smoke emission in microgravity.

ing the backlighted frames, and results are reported in Fig. 4. Smoke-emitting conditions are defined as spreading situations where a continuous flow of broadband absorbing soot particles is reported at the flame trailing edge. On the contrary, smoke-free conditions are defined as spreading situations where the closed-tip flame does not display detectable absorption at the trailing edge (see both Pure LDPE conditions in Fig 1 for instance). It is worth reporting that the flame spread over the EG 10wt% samples is too slow to discriminate the smoking condition, since the flame trailing edge is still intertwined with the igniter.

At both normal and micro-gravity, no smoke emission was observed over pure LDPE in the studied range of oxygen contents. At normal gravity, no smoke emission is also reported for all flame retardant-loaded samples, over the range of oxygen contents studied. It should be pointed out that results are affected by significant dripping, which can reduce the fuel supply to the flame, thereby reducing soot production. Besides, it is also worth mentioning that the decrease in soot residence time within buoyant flames also reduces the radiative heat losses, leading to flame temperatures at the trailing edge high enough to support complete soot oxidation.

Under microgravity conditions, flame retardant-loaded samples show a consistent tendency to emit smoke at an oxygen content of 21% for all flame retardant types and loading. In addition, smoke emission is also observed at an oxygen content as low as 19% for EG-loaded samples of 5 wt%. But, since the nature of EG and AP intumescence is different, the mechanisms leading to smoke emission are different. EG expansion creates graphite worms through rapid sublimation. As such, it promotes the production of carbonaceous elements which can be released in the flame. Combined with the increase in residence time and hence radiative losses in microgravity, this promotes smoke release. In addition, higher EG loading leads to an increase in carbon particle production and thus also increases the possibility of smoke emission. AP expansion, on the other hand, is driven by a carbonation mechanism that also promotes smoke emission. When the AP loading increases, the amount of char promoters also increases, thus strengthening the carbonation mechanism. As a result, the smoking also increases with AP loading. Comparing both flame retardants, the increase in EG loading causes the smoke emission transition to occur at lower oxygen content conditions, while the increase in AP loading has relatively a weaker impact on smoke emission. This is attributed to the different intumescent mechanisms, affecting the pyrolysis processes differently as oxygen content is increased. The gaseous fuel generated from pyrolysis flows through the intumescent region up to the trailing edge. This tends to increase the residence time, favoring soot production, which increases the hazard of smoke emission. As compared to the AP-loaded sample, the EG-loaded one produces a larger intumescent region at similar loading, which leads also to a longer residence time, further promoting the smoke emission. In addition, the cohesion of the EG residue structure is lower than that of the AP residue after combustion. As a result, it can be anticipated that the carbonaceous matter is released at a higher rate from the EG-loaded sample, which also promotes the smoke emission.

Smoke emission is heavily influenced by oxygen content in microgravity, as the flames spreading over all flame retardant-loaded samples transition from non-smoking to smoking when the oxygen content is increased. Oxygen content has a mixed effect on smoke emission. Higher oxygen content provides higher stoichiometric flame temperature and a higher soot oxidation rate [29], which should block smoke emission. But from the results of the previous section, it also appears that the flame spread rate,and consequently the pyrolysis rate, increases with oxygen content, which facilitates smoke production [12]. And the pyrolysis rate is determined as:

$$\dot{m}_F = \rho_{pe} \cdot \pi \cdot r_s^2 \cdot u_f \tag{1}$$

where ρ_{pe} is the density of LDPE, r_s is the cylinder radius and u_f is the spread rate.

Table 1: Flame spread rate exponent β for different samples in microgravity

Pure	EG2%	EG5%	EG10%	AP5%	AP10%
4.84 ± 1.76	3.84 ± 1.16	2.73 ± 0.67	3.11 ± 0.79	3.05 ± 2.35	2.53 ± 0.17

To further investigate the role of oxygen content, the relationship between pyrolysis mass flow rate $\dot{m}_F$ and oxygen content x_{O_2} is quantified, following Guibaud et al. [30]. The power law relating pyrolysis mass flow rate to oxygen content is extracted from a least square optimization using logarithmic transform to identify the parameter β, as shown in Eq. (2).

$$\dot{m}_F = C\, x_{O_2,\infty}^{\beta} \tag{2}$$

where C is a constant.
The value of β is then contrasted to a previous investigation by Glassman and Yaccarino at normal gravity [31]. The authors investigated the effect of oxygen content on a coflow diffusion flame at atmospheric pressure, and reported the variation of critical ethylene fuel flow rate $\dot{m}_F^c$ to sustain quenching conditions at the flame tip. Based on the variation of this critical value in the oxygen content range of the present experiment, a critical mass flow rate can be obtained as:

$$\dot{m}_F^c = C\, x_{O_2,\infty}^{0.82\pm0.14} \tag{3}$$

Any variation above this critical value fosters smoke emission, while any variation below hampers smoke emission. With the present configuration, the fuel is made of a similar chemical structure at the molecular level (polyethylene). Still, it is solid and the fuel pyrolysis rate is especially a function of the oxygen content, therefore cannot be freely adjusted. To understand whether a variation in oxygen content and the subsequent variation in fuel mass flow rate can trigger the release of smoke, a method similar to that of Glassman and Yaccarino is also applied to the present results in microgravity. The values of β extracted for the different sample types (reported in Tab. 1) are contrasted with the critical variation reported by Glassman and Yaccarino. All values for β are higher than the critical fuel flow rate variation of Eq. (3), so it can be concluded that the pyrolysis mass flow rate of all samples in microgravity increases faster than the critical mass flow rate required to sustain quenching at the flame trailing edge as the oxygen content increases. This means that the increase in pyrolysis mass flow rate with oxygen can be sufficient to justify a transition from non-smoking to smoking conditions. In addition, in the present case and as stated previously, the smoke release is also promoted by the effect of flame retardants on pyrolysis. Consequently, if high flame retardants loadings can further reduce flame spread rate until the increase in pyrolysis rate drops below its critical value, the transition from non-smoking to smoking still needs to be verified.

4. Conclusion

LDPE samples loaded with two types of intumescent flame retardants, EG and AP, were ignited at varying levels of oxygen content at normal and microgravity, to analyze the associated extinction limits, flame spread rates, and smoke emissions. The results show strong differences between microgravity and normal gravity conditions, which call for cautious integration of flame retardants in the scope of space exploration. The extinction limit increases with flame retardants loading at normal gravity, but this effect is not reported in microgravity. At normal gravity, an increased flame retardant load inhibits flame spread, this effect is also observed, though less pronounced, when assessing the average spread rate in microgravity. Under the same ambient conditions and the same loading, EG-loaded samples show a reduced flame spread rate compared to AP-loaded samples. To confirm that these results stand once the flame spreads steadily, similar long-duration experiments are required. Though flame retardants enhance fire safety in microgravity by lowering the flame spread rate, they also facilitate smoke emission to an extent that is not reported at normal gravity. The enhanced propensity to emit smoke is especially noticeable over the EG-loaded sample in spite of the lower flame spread rate, because the intumescence production mechanism readily contributes to soot formation in the absence of gravity. Globally, it is observed that the combustion characteristics of samples loaded with flame retardants in microgravity are different from those at normal gravity, stressing the need for additional experimental observations prior to their adoption in spacecraft design.

Acknowledgments

The authors feel grateful to the Centre National d'Etudes Spatiales (CNES) for its financial support under Contract No. 130615.

Supplementary material

An image of AP and EG residue after combustion and the data of average flame spread rates and their uncertainties are provided as supplementary material.

References

[1] National Research Council, Recapturing a Future for Space Exploration: Life and Physical Sciences Research for a New Era, The National Academies Press, Washington, DC, 2011.

[2] O. Fujita, Solid combustion research in microgravity as a basis of fire safety in space, Proc. Combust. Inst. 35 (3) (2015) 2487–2502.

[3] G. Jomaas, J. L. Torero, C. Eigenbrod, J. Niehaus, S. L. Olson, P. V. Ferkul, G. Legros, A. C. Fernandez-Pello, A. J. Cowlard, S. Rouvreau, et al., Fire safety in space–beyond flammability testing of small samples, Acta Astronautica 109 (2015) 208–216.

[4] S. Olson, M. Johnston, J. T'ien, Flammability Aspects of a Cotton-Fiberglass Fabric in Opposed and Concurrent Airflow in Microgravity, American Society for Gravitational and Space Research, 2012.

[5] S. Link, X. Huang, C. Fernandez-Pello, S. Olson, P. Ferkul, The effect of gravity on flame spread over pmma cylinders, Scientific reports 8 (1) (2018) 1–9.

[6] A. Guibaud, J.-M. Citerne, J.-L. Consalvi, J. L. Torero, O. Fujita, M. Kikuchi, P. V. Ferkul, N. Smirnov, G. Jomaas, B. Toth, S. Rouvreau, G. Legros, Accessing the soot-related radiative heat feedback in a flame spreading in microgravity: optical designs and associated limitations, Proc. Combust. Inst. 38 (3) (2021) 4805–4814.

[7] Y. Nakamura, T. Kashiwagi, S. Olson, K. Nishizawa, O. Fujita, K. Ito, Two-sided ignition of a thin pmma sheet in microgravity, Proc. Combust. Inst. 30 (2) (2005) 2319–2325.

[8] M. A. Delichatsios, R. A. Altenkirch, M. F. Bundy, S. Bhattacharjee, L. Tang, K. Sacksteder, Creeping flame spread along fuel cylinders in forced and natural flows and microgravity, Proc. Combust. Inst. 28 (2) (2000) 2835–2842.

[9] O. Fujita, T. Kyono, Y. Kido, H. Ito, Y. Nakamura, Ignition of electrical wire insulation with short-term excess electric current in microgravity, Proc. Combust. Inst. 33 (2) (2011) 2617–2623.

[10] S. Takahashi, H. Ito, Y. Nakamura, O. Fujita, Extinction limits of spreading flames over wires in microgravity, Combustion and flame 160 (9) (2013) 1900–1902.

[11] P. S. Greenberg, K. R. Sacksteder, T. Kashiwagi, Wire insulation flammability experiment: Usml-1 one year post mission summary, Joint Launch and One Year Science Review of USML-1 and USMP-7 with the Microgravity Measurement Group 2 (1994).

[12] A. Guibaud, J.-M. Citerne, J.-L. Consalvi, G. Legros, On the effects of opposed flow conditions on non-buoyant flames spreading over polyethylene-coated wires–part i: Spread rate and soot production, Combustion and Flame 221 (2020) 530–543.

[13] S. Garber, J. Linenger, Fire and controversy january 12-may 24, NASA History Program Office (1997).

[14] E. Orndoff, Flame retardant fibers for human space exploration-past, present, and future, Dornbirn Man-Made Fibers Congress (2017).

[15] S. Takahashi, M. A. F. bin Borhan, K. Terashima, A. Hosogai, Y. Kobayashi, Flammability limit of thin flame retardant materials in microgravity environments, Proc. Combust. Inst. 37 (3) (2019) 4257–4265.

[16] S. Takahashi, K. Terashima, M. A. F. bin Borhan, Y. Kobayashi, Relationship between blow-off behavior and limiting oxygen concentration in microgravity environments of flame retardant materials, Fire Technology 56 (1) (2020) 169–183.

[17] G. Fohlen, J. Parker, S. Riccitiello, P. Sawko, Intumescence: an in situ approach to thermal protection, WESRAC-Fireproofing and Safety Symposium (1972).

[18] D. A. Kourtides, Flame-retardant composite materials, Vol. 3109, Technology 2000: Proceedings of a Conference, 1991.

[19] J. Alongi, Z. Han, S. Bourbigot, Intumescence: Tradition versus novelty. a comprehensive review, Progress in Polymer Science 51 (2015) 28–73.

[20] S. Bourbigot, M. Le Bras, R. Delobel, Carbonization mechanisms resulting from intumescence association with the ammonium polyphosphate-pentaerythritol fire retardant system, Carbon 31 (8) (1993) 1219–1230.

[21] S. Bourbigot, J. Sarazin, T. Bensabath, F. Samyn, M. Jimenez, Intumescent polypropylene: reaction to fire and mechanistic aspects, Fire Safety Journal 105 (2019) 261–269.

[22] T. Bensabath, J. Sarazin, M. Jimenez, F. Samyn, S. Bourbigot, Intumescent polypropylene: Interactions between physical and chemical expansion, Fire and Materials 45 (3) (2021) 387–395.

[23] J.-M. Citerne, H. Dutilleul, K. Kizawa, M. Nagachi, O. Fujita, M. Kikuchi, G. Jomaas, S. Rouvreau, J. L. Torero, G. Legros, Fire safety in space–investigating flame spread interaction over wires, Acta Astronautica 126 (2016) 500–509.

[24] A. Guibaud, J. Citerne, J. Orlac'h, O. Fujita, J.-L. Consalvi, J. Torero, G. Legros, Broadband modulated absorption/emission technique to probe sooting flames: Implementation, validation, and limitations, Proc. Combust. Inst. 37 (3) (2019) 3959–3966.

[25] A. Guibaud, J.-M. Citerne, J.-L. Consalvi, O. Fujita, J. Torero, G. Legros, Experimental evaluation of flame radiative feedback: methodology and application to opposed flame spread over coated wires in microgravity, Fire Technology 56 (1) (2020) 185–207.

[26] M. Nagachi, J.-M. Citerne, H. Dutilleul, A. Guibaud, G. Jomaas, G. Legros, N. Hashimoto, O. Fujita, Effect of ambient pressure on the extinction limit for opposed flame spread over an electrical wire in microgravity, Proc. Combust. Inst. 38 (3) (2021) 4767–4774.

[27] D. Mulville, Flammability, odor, offgassing, and compatibility requirements and test procedures for materials in environments that support combustion, Tech. rep., NASA-STD-6001 (1998).

[28] M. C. Johnston, S. James, D. E. Muff, X. Zhao, S. L. Olson, P. V. Ferkul, Self induced buoyant blow off in upward flame spread on thin solid fuels, Fire safety journal 71 (2015) 279–286.

[29] J.-L. Consalvi, A. Guibaud, A. Coimbra, J.-M. Citerne, G. Legros, Effects of oxygen depletion on soot production, emission and radiative heat transfer in opposed-flow flame spreading over insulated wire in microgravity, Combustion and Flame 230 (2021) 111447.

[30] A. Guibaud, J.-M. Citerne, J.-L. Consalvi, G. Legros, On the effects of opposed flow conditions on non-buoyant flames spreading over polyethylene-coated wires–part ii: Soot oxidation quenching and smoke release, Combustion and Flame 221 (2020) 544–551.

[31] I. Glassman, P. Yaccarino, The effect of oxygen concentration on sooting diffusion flames, Combustion Science and Technology 24 (3-4) (1980) 107–114.